Chemical Physics Impact 9 (2024) 100757

Contents lists available at ScienceDirect

Chemical Physics Impact

journal homepage: www.sciencedirect.com/journal/chemical-physics-impact

Full Length Article

Evaluation of *Taraxacum officinale* phytoconstituents as potential JNK1 inhibitors: Perspectives from ADMET, molecular docking, molecular dynamics, and density functional theory

Sphelele C. Sosibo [a,b,*], Hendrik G. Kruger [c], Wonder P. Nxumalo [d,e], Zimbili Zondi [a]

[a] Department of Chemistry, School of Physical and Chemical Sciences, North-West University, Private Bag X2046, Mmabatho, 2735
[b] Materials Science Innovation and Modelling (MaSIM), North-West University, Private Bag X2046, Mmabatho, 2735
[c] Catalysis and Peptide Research Unit, University of KwaZulu-Natal, Durban, 4001, South Africa
[d] Department of Pharmacology, School of Medicine, University of Pretoria, Private Bag X323, Arcadia, 0007
[e] Organic and Bio-Analysis, National Metrology Institute of South Africa, Private Bag X34, Lynnwood Ridge, 0040

ARTICLE INFO

Keywords:
Taraxacum officinale
c-Jun N-terminal kinase
Type-2 diabetes
DFT
MD

ABSTRACT

The impact of activated c-Jun N-terminal kinase isoform JNK1 chemical pathways in insulin biosynthesis poses a potential health risk of glucose intolerance. Blocking the activity of JNK1 is a promising route for the design of anti-diabetic drugs and associated metabolic syndromes. In this study, 17 extracts of *Taraxacum officinale* were chosen to bind JNK1 and ascertain their modulatory activity. We employed molecular dynamics, density functional theory and three docking approaches: standard precision, extra precision and quantum polarized ligand docking. The best binding free energy results were obtained from the quantum polarized ligand docking, with myricetin (1) showing a docking score of -10.464 kcal/mol, while quercetin (2) and daphnetin (3) displayed values of -9.769 and -7.136 kcal/mol respectively. Following this, 100 ns molecular dynamics simulations with Desmond showed stabilization average root mean square deviations of 2.34, 2.87, and 2.88 Å for myricetin, quercetin and daphnetin. Further, molecular dynamics revealed complexes of myricetin (ΔG = -38.81 kcal/mol) and quercetin (ΔG = -34.99 kcal/mol) as the most stable inside the JNK1 interface. The energy gaps for myricetin, quercetin and daphnetin were estimated to be 6.17, 6.00 and 6.53 eV employing the M06–2X functional in PCM solvation. Further, myricetin showed the strongest intramolecular hydrogen bonding with -13.06 kcal/mol. This study provides insights into possible anti-type-2 diabetes properties of *Taraxacum officinale* targeting JNK1.

1. Introduction

Type 2 diabetes mellitus (T2D) is a major metabolic syndrome of insulin resistance or deficiency, resulting in abnormal blood glucose levels [1]. Recent studies also associate ectopic lipid accumulation with the progression of T2D. [2,3] According to the International Diabetes Federation, around 536.6 million people had diabetes worldwide in 2021 [4]. This number is expected to rise by 20 % in 2030 and by 46 % by 2045 [4]. The surge in T2D prevalence remains a universal public health concern due to the high cost of care, the number of associated risk factors and the increasing mortality rate [5]. It is estimated that over 470 million people will be prediabetic in 2030. Moreover, 5–10 % of people with prediabetes progress to diabetes annually [5].

Several synthetic anti-diabetic agents with hypoglycemic activities are available in the market. Examples include thiazolidinediones, α-glucosidase inhibitors, sulfonylureas, biguanides, meglitinides, glucagon-like peptide-1 receptor agonists, dipeptidyl peptidase-4 inhibitors and sodium-glucose transporter inhibitors [6]. However, most of these drugs are reported to trigger several side effects [7] and T2D patients on treatment are prone to develop chronic complications. [8–10] Prolonged hyperglycemia results in the impairment of the metabolism of electrolytes, fats, and carbohydrates. [11,12] These diabetic complications damage endothelial capillary cells and may negatively impact the vascular system. [2,13] The harmful accumulation of glucose in diabetic states mainly impacts the renal glomerulus, the retina, and central and peripheral nervous systems [13]. There is an urgent need to develop new anti-T2D drugs for long-term glucose regulation and minimisation of side effects. The mechanism of T2D is

* Corresponding author at: Department of Chemistry, School of Physical and Chemical Sciences, North-West University, Private Bag X2046, Mmabatho, 2735.
E-mail addresses: Sphelele.Sosibo@nwu.ac.za (S.C. Sosibo), Kruger@ukzn.ac.za (H.G. Kruger), wonderchemist21@gmail.com (W.P. Nxumalo), Zimbili.Mkhize@nwu.ac.za (Z. Zondi).

https://doi.org/10.1016/j.chphi.2024.100757
Received 7 August 2024; Received in revised form 30 September 2024; Accepted 10 October 2024
Available online 22 October 2024
2667-0224/© 2024 The Authors. Published by Elsevier B.V. This is an open access article under the CC BY-NC-ND license (http://creativecommons.org/licenses/by-nc-nd/4.0/).

Table 1
Physiochemical properties of 17 selected Taraxacum officinale bioactive compounds along with standards.

PubChem CID	Compound	Molecular formula	Molecular weight/gmol^{-1}
115250	Taraxasterol	$C_{30}H_{50}0$	426.7
689043	Caffeic acid	$C_9H_8O_4$	180.16
5280794	Stigmasterol	$C_{29}H_{24}0$	412.7
5281764	Chicoric acid	$C_{22}H_{18}0_{12}$	474.4
95392279	Taraxinic acid 1′-O-β-D-glucopyranoside	$C_{21}H_{28}O_9$	424.4
101553163	Ixerin D	$C_{21}H_{30}O_9$	426.5
5280637	Cynaroside	$C_{21}H_{20}O_{11}$	448.4
5280343	Quercetin	$C_{15}H_{10}0_7$	302.23
5281672	Myricetin	$C_{15}H_{10}0_8$	318.23
132567	Curculigoside B	$C_{21}H_{24}0_{11}$	452.4
6508	Quinic acid	$C_7H_{12}0_6$	192.17
161496	Bruceine B	$C_{23}H_{28}O_{11}$	480.5
23669636	Sodium ferulate	$C_{10}H_9NaO_4$	216.17
525	Malic acid	$C_4H_6O_5$	134.09
5280569	Daphnetin	$C_9H_6O_4$	178.14
5318597	Isomangiferin	$C_{19}H_{18}O_{11}$	422.3
3233896	2-(4-Methoxyphenoxy)-8-(thiophen-2-yl-methyl) pteridin-7-one	$C_{18}H_{14}N_4O_3S$	366.4
4091	MetforminH$^+$*	$C_4H_{11}N_5$	129.16
72700745	AX13587**	$C_{26}H_{26}FN_50_2$	459.5
1176	Urea#	CN_2H_4O	60.03

* FDA approved antidiabetic drug
** native ligand
\# prototype for nonlinear optical properties

linked to obesity since elevated levels of tumour necrosis factor-alpha (TNF-α) from the adipose tissue decrease insulin sensitivity. [14,15] Further, the elevation of systematic free fatty acids (FFA) in normal humans or animals has been shown to induce insulin resistance, leading to elevated hepatic glucose output. [16,17] It is widely accepted that obesity-induced inflammatory response activation of protein kinases such as IκB kinases and of JNKs govern the etiology of T2D. [18–20] TNF-α and FFA are potent c-Jun N-terminal kinases (JNKs) activators [21].

The first reports of JNKs belonging to the mitogen-activated protein kinase (MAPK) subfamily date to 1994. [22,23] Activated JNKs regulate cellular differentiation and trigger the phosphorylation of transcription factors interlinked to apoptosis [24]. Moreover, JNKs govern the signal transduction in response to a sequence of extra-cellular stimuli resulting from pro-inflammatory cytokines or environmental stressors [25]. Due to this, these kinases are negatively associated with the onset of various diseases, including inflammation, cardiovascular diseases, diabetes mellitus and cancer. [26,27] Three genes code for the biosynthesis of JNKs, namely *Jnk1, Jnk2* and *Jnk3* [28]. Human chromosomes 10q11.22 and 5q35 secrete *Jnk1* and *Jnk2*, resulting in broad tissue distribution of these genes [29]. Contrary to *Jnk1* and *Jnk2, Jnk3* is expressed in human chromosome 4q22.1-q23 localized in the brain, heart, and testes [29]. The messenger RNA transcripts alternatively splice the three encoding genes (*Jnk1, Jnk2* and *Jnk3*) into their respective JNK isoforms (JNK1 (4), JNK2 (4) and JNK3 (2)). [30–32] Isoform JNK3 has been investigated as a target for neurogenerative disorders, and recent reports suggest that the biological activities of JNK1 and JNK2 are opposing [33]. JNK2 activity supports cell proliferation and invasiveness, while JNK1 promotes apoptosis. [34,35]

Among the three possible isoforms, JNK1 (also called MAPK8) is mostly associated with the ontogeny of obesity-induced insulin resistance preceding T2D [36]. It has been reported that the JNK1 pathway impedes insulin activity and hampers β cell action [37]. Hirosumi *et. al.* [38] used two mice models to show that under diabetic conditions, the JNK activity is abnormally high. Further, this study established that the lack of JNK1 recovered insulin signalling ability, decreased adiposity and improved insulin sensitivity [38]. Many studies point to the inhibition of JNK1 as a promising route to new anti-T2D candidates by protecting pancreatic β cells from inflammatory onset stimulation. [39,40] Several pan and isoform-specific JNK inhibitors are in development, but there has been no promising outcome to date. [33,41–44]

Due to their few side effects and multiple-target treatment, natural products are plentiful drug discovery sources [45]. There has been an increase in the interest of using natural phytoconstituents and nutraceuticals to manage diseases [46]. *Taraxacum officinale* (*T. officinale*) is a medicinal plant native to Europe and Asia but has naturalized in India, North America, southern Africa, South America, New Zealand, Australia, and Canada. [47,48] Root and aerial extracts of this plant are reported in various literature to mitigate diverse metabolic syndromes as they are rich in phytocompounds such as terpenes, phenolic acids and flavonols [46]. Furthermore, *T. officinale* has many diverse uses, such as

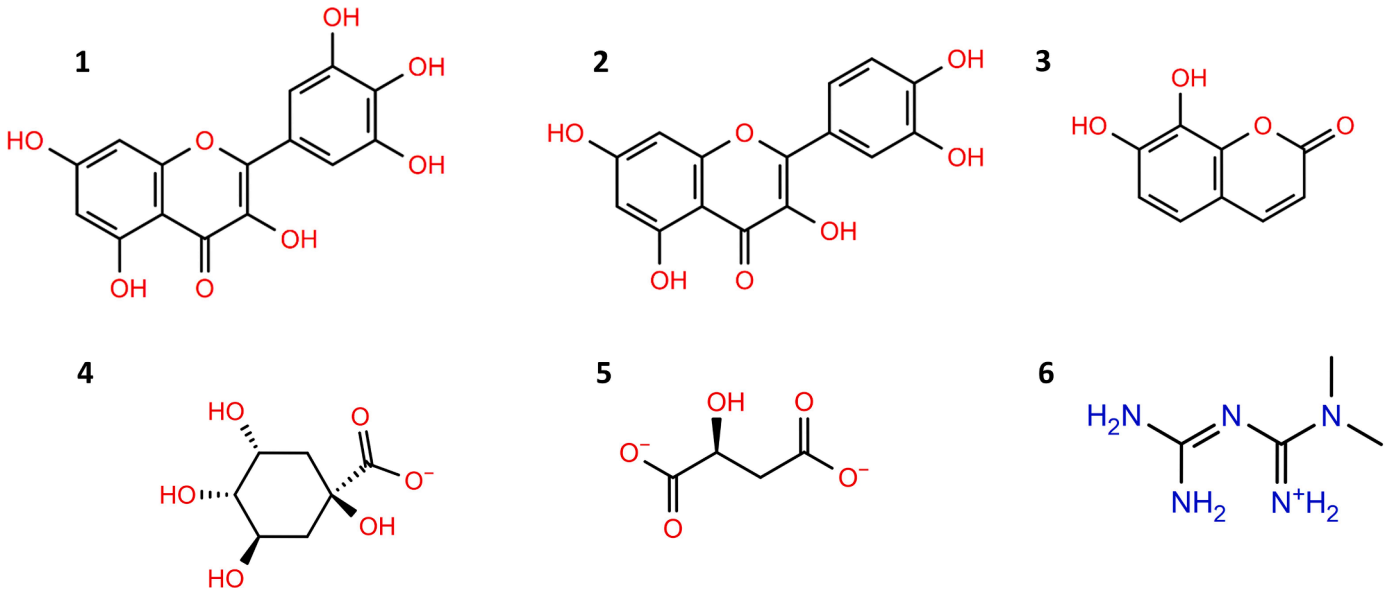


Fig. 1. Best binding compounds (1) Myricetin (CID 5281672); (2) Quercetin (CID 5280343); (3) Daphnetin (CID 5280569); (4) Quinate (CID 1560034); (5) Malate (CID 160434); and (6) MetforminH$^+$ (CID 4091). NB: Quinic acid (CID 6508) and malic acid (CID 525) were deprotonated at pH 7 during ligand preparation into their respective ions (4 and 5).

Table 2
Docking results in Glide gscores, docking score, Glide energy, hydrogen bond interactions and Prime energies.

CID	Glide SP docking				
	Glide gscore (kcal/mol)	Docking score (kcal/mol)	Summary of interactions	Interacting residues and distance (Å)	MMGBSA ΔG bind (kcal/mol)
5281672	-7.580	-7.542	6H bonds, 1π-Sulfur, 8π-Alkyl	Ile32/H_2O (2.47, 1.87), Ile32(2.28), Glu109 (1.91), Ser34 (2.03), Met111 (2.31), Met108 (5.00), Ala53 (3.52, 4.82), Val158 (4.49, 5.40), Leu168 (4.72, 4.77, 5.08), Val40 (4.46, 5.16)	-37.49
5280343	-7.673	-7.641	5H bonds, 2π-Sulfur, 8π-Alkyl	Ile32/H_2O (2.47, 1.76), Ile32 (2.22), Glu109 (1.80), Met111 (2.31), Met108 (5.03, 5.71), Ala53 (3.51, 4.82), Val158 (4.52, 5.46), Leu168 (4.81, 511), Val40 (4.40, 5.41)	-38.27
5280569	-7.252	-7.233	3H bonds, 1π-σ, 2π-Sulfur, 5π-Alkyl	Lys55 (2.64), Glu 109 (2.24), Met111 (2.04), Val158 (2.90), Met108 (4.77, 5.31), Ala53 (3.77, 5.00), Leu168 (4.08, 5.04), Val40 (4.48)	-42.13
1560034	-5.646	-5.646	6H bonds, 1Salt bridge, 1Charge-Charge, 1Alky	Ser34 (1.71, 1.94), Lys55 (2.49), Ser155 (1.67), Asn156 (2.43, 2.81), Lys55(3.62), Arg69 (5.11), Leu168 (4.57)	-12.02
160434	-4.200	-4.200	3H bonds	Ile32/H_2O (2.08, 2.47), Lys55 (2.51)	3.84
4091*	-3.035	-2.668	2H bonds	Ser34 (1.86), Glu109 (2.00)	-10.72

* MetforminH$^+$

Table 3
Docking results in Glide gscores, docking score, Glide energy, hydrogen bond interactions and Prime energies.

CID	Glide XP docking				
	Glide gscore (kcal/mol)	Docking score (kcal/mol)	Summary of interactions	Interacting residues and distance (Å)	MMGBSA ΔG bind (kcal/mol)
5281672	-9.806	-9.769	3H bonds, 2π-Sulfur, 7π-Alkyl	Ile32/H_2O (1.75, 2.47), Glu109 (1.91), Met108 (4.84, 5.55), Ala53 (3.56, 5.12), Val158 (4.64), Leu168 (4.54, 4.92, 4.96), Val40 (4.31)	-31.00
5280343	-9.390	-9.358	3H bonds, 1π-σ, 2π-Sulfur, 7π-Alkyl	Ile32/H_2O (1.89, 2.47), Glu109 (1.66), Val158 (2.92), Met108 (5.15, 5.40), Ala53 (3.59, 4.83), Lys55 (5.16), Val158 (2.92), Leu168 (4.58, 4.71, 5.11)	-40.88
5280569	-8.546	-8.527	2H bonds, 1π-σ, 2π-Sulfur, 5π-Alkyl	Ile32 (2.79), Met111(1.74), Val40 (2.92), Met108 (4.75, 5.03), Ala53 (3.54, 4.89), Val158 (4.57), Leu168 (4.37, 4.89)	-39.77
1560034	-5.736	-5.735	5H bonds, 1Charge-Charge	Gln37 (1.83), Glu73 (1.97, 1.98, 2.14), Asn156 (2.79), Arg69 (5.01)	-9.37
160434	-3.884	-3.884	4H bonds	Ile32/H_2O (1.81, 2.47), Met111 (1.74, 2.10)	11.20
4091*	-1.693	-1.325	4H bond, 1Charge-Charge	Ile32/H_2O (2.38, 2.47), Met111 (1.90, 2.24)	-17.07

* MetforminH$^+$

culinary as food, medicine as a diuretic, and textile as a natural dye [49]. Commonly known as dandelion, *T. officinale* is listed as a 'generally recognized as safe' substance by the US Food and Drug Administration [46]. This plant is recognized in the British and Chinese Herbal Pharmacopoeia, while in Germany, the roots are registered as a medicinal tea [46]. The German Commission E monographs recommend a dosage of 3 – 4 g twice daily for roots or 10 – 15 drops of root tincture thrice daily [46]. Furthermore, a dose of 4 -10 g or 2 – 5 mL tincture three times a day is recommended for the leaf [46]. *T. officinale* has been studied and applied in the mitigation of T2D. [46,49] Due to its anti-oxidative, anti-inflammatory, and anti-hyperglycemic activities, dandelion serves as a significant anti-diabetic plant [49].

Computational methods play a huge role in all the stages of drug discovery. [50–52] The wide availability and impact of computational methods may also mask the lack of state-of-the-art and sophisticated techniques required for drug discovery [50]. There has been a growth in the interest in computational screening of plant-based compounds for drug development. [53,54] Diverse theoretical approaches have been applied to discovering JNK1 inhibitors in recent years. [55–57] The present investigation explored the role of dandelion extracts on JNK1. We employed standard- and extra-precision (SP & XP) docking and quantum mechanics polarized ligand docking (QPLD) followed by Prime/MM-GBSA energetics. Absorption, distribution, metabolism, excretion, and toxicity (ADMET) parameters, as well as density functional theory (DFT), were also used to study the pharmacokinetics and charge distribution of the ligands, respectively. Molecular dynamics (MD) were applied to study the interaction kinetics and stability of complexes of JNK1 and *T. officinale* phytocompounds.

The analysis revealed that phytocompounds were more stabilized for binding JNK1 than the positive control metforminH$^+$. Quercetin emerges as the most promising candidate due to its superior binding affinity, stability during simulations, optimal ADMET properties and favourable nonbonding interaction DFT results. According to our knowledge, this is the first comprehensive computational investigation

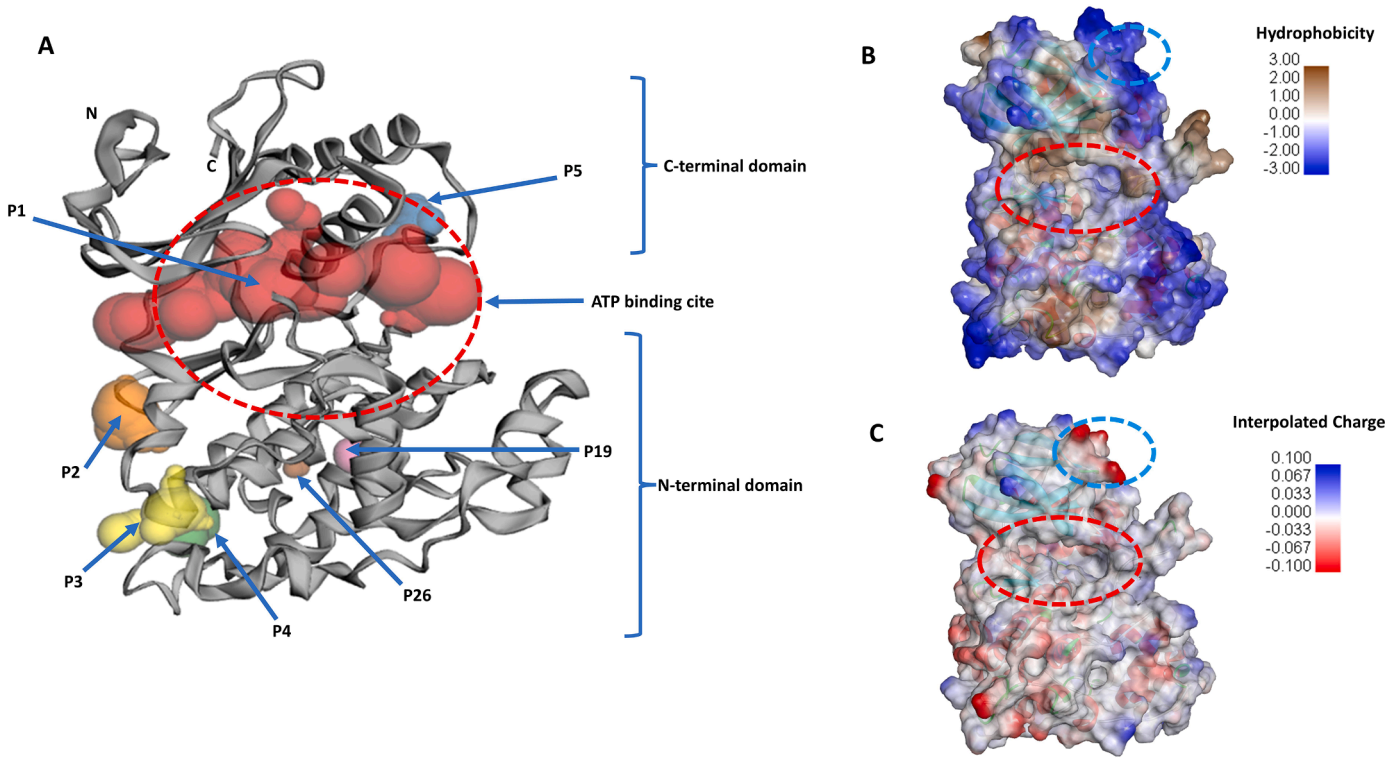


Fig. 2. Protein surface and charge analysis of (A) Pockets and crevices calculated in CASTp 3.0 (B) Hydrophobicity of the binding regions. (C) Charge distribution of protein 4L7F.

of *T. officinale* phytocompounds against JNK1.

2. Computational methodology

ADMET, docking, and MD studies were conducted in the Maestro interface v 12.8 (Schrödinger Release 2022–1: Maestro, Schrödinger, LLC, New York, NY, 2021). DFT was performed in the Gaussian 09 program [58] and NBO was analyzed in the NBO7 program [59]. Multiwfn [60], Gaussum [61], gnuplot [62] and UCA Fukui [63] were employed for DFT postprocessing.

2.1. Ligand preparation

The 3D structure-data files of 17 *T. officinale* isolates [46,49] and all other nonstandard residues (Table 1) were obtained from PubChem (https://pubchem.ncbi.nlm.nih.gov) [64]. FDA approved antidiabetic inhibitor metforminH$^+$ was used as a reference drug. [65,66] AX13587 and urea were used as prototypes for docking procedure validation and nonlinear optical property evaluation respectively. The LigPrep module (Schrödinger Suites 2022–1: LigPrep; Schrödinger, LLC, New York, NY, 2021) was used for structural processing. The structures were energy minimized and optimized employing the Optimized Potentials for Liquid Simulations 4 (OPLS4) forcefield [67]. The Epik [68,69] (Schrödinger Release 2022–1: Epik, Schrödinger, LLC, New York, NY, 2021) tool was used to desalt the compounds and to generate low-energy ionization and tautomeric states within the pH range of 7.0 ±1.0. All possible structural conformers were considered, and the best three were generated for each ligand. Hydrogen bonds were optimized through the prediction of the pKa of ionizable groups employing PROPKA [70]. From the 17 input ligands, LigPrep module generated a library of 29 compounds ready for docking.

2.2. Receptor preparation

The crystal structure of JNK1 with PDB ID: 4L7F, complexed to a small drug molecule AX13587 was retrieved from the RCSB database (https://www.rcsb.org/) [71]. The chosen JNK1 monomeric receptor was resolved through the x-ray diffraction method with a resolution of 1.96 Å. The protein was prepared in the Protein Preparation Wizard [72] (Schrödinger Release 2022–1: Protein Preparation Wizard; Epik, Schrödinger, LLC, New York, NY, 2021; Impact, Schrödinger, LLC, New York, NY; Prime, Schrödinger, LLC, New York, NY, 2021) tools of the Schrödinger Maestro suite. In protein preparation, missing side- and backbone chains and hydrogen atoms were added to the JNK1 system. Missing heavy backbone atoms were manually added employing the 3D system builder. Distant crystalline waters, measured beyond 5 Å from heteroatomic groups, were removed from the protein structure. Furthermore, parameterization such as bond length optimization, bond order assignments, possible disulfide formation, protein terminal capping, missing loops rectification and refinement were carried out. The protonation and tautomeric states of charged amino acids such as Glu, Asp and His were determined during refinement. Further, the protonation states close to the physiological pH (7.5 ±1.0) of the selected monomeric protein were achieved by the PROPKA [70] function. In the last step of protein preparation, the OPLS4 [67] forcefield was employed to minimize the protein crystal. The minimization was restrained until heavy atoms converged, with root mean square deviation (RMSD) of 0.30 Å.

2.3. Grid generation

The Glide [73] (Schrödinger Release 2022–1: Glide, Schrödinger, LLC, New York, NY, 2021) receptor grid generation panel was employed to generate the receptor grid. The grid was created based on the centroid of the co-crystalized ligand AX13587 with an outer box size of 40 × 40 × 40 Å^3 and an inner box of 10 × 10 × 10 Å^3 within the minimised protein. Ligand size cut-off was adjusted to 30 Å within the coordinates x = -4.34, y = 53.16, z = 4.68 based on the OPLS_2005 [74] atom typing without any constraints imposed. The grid was generated with van der Waals radii of receptor scaled by 1.0. The charge cut-off for polarity was set to

Table 4
Docking scores, glide energy and Prime energies of five bioactive plant components against 4L7F.

CID	Glide QPLD				
	Glide gscore (kcal/mol)	Docking score (kcal/mol)	Summary of interactions	Interacting residues	MMGBSA ΔG bind (kcal/mol)
5280343	-10.464	-10.432	4H bonds, 1π-σ, 1π-Sulfur, 5π-Alkyl	Met111 (1.74, 185) Asn156 (1.75), Lys55 (2.28), Ile32 (2.77 Or 4.44)[#], Met108 (5.43), Val40 (4.47), Met108 (5.43), Ala53 (4.47), Val158 (5.10), Leu168 (3.99, 4.54)	-44.65
5281672	-9.769	-9.732	5H bonds, 1Sulfur- X, 2π-σ, 2π-Sulfur, 3π-Alkyl	Ile32 (2.07), Gly35 (1.70), Gly38(2.29), Lys55 (2.45), As156 (1.75), Met108 (5.74, 5.87), Val40 (2.76, 2.86), Met108 (5.74, 5.87), Ala53 (5.40), Leu168 (4.45, 4.85)	-39.58
5280569	-7.136	-7.118	3H bonds, 1π-σ, 2π-Sulfur, 5π-Alkyl	Lys55 (2.64), Glu109 (2.25), Met111 (2.06), Val158 (2.90), Met108 (4.77, 5.30), Val40 (4.48), Ala53 (3.77, 4.98), Leu168 (4.08, 5.04)	-35.62
1560034	-5.167	-5.166	3H bonds, 1Salt bridge, 1Charge-Charge	Arg69 (2.16), Glu73 (2.10, 2.34), Lys55 (3.63), Lys55 (5.10)	-6.57
160434	1.954	1.954	3H bonds	Ile32/H_2o (1.93, 2.47) Met111 (2.51)	0.33
4091[*]	-2.417	-2.050	1H bond	Met111 (1.95)	-18.88

[#] Conformation dependent
[*] Metforminh$^+$

0.25, keeping the site, rotatable groups constraints and exclusion of volumes at default options.

2.4. Forcefield-based molecular docking

A stepwise structure-based ligand docking was carried out using Maestro's Virtual Screening Workflow (VSW) utility tool. Two sequential docking protocols integrated into the Glide VSW were carried out: standard precision (SP) and extra-precision (XP) modes. To the 29 ligands, a QikProp (Schrödinger Release 2022–1: QikProp; Schrödinger, LLC, New York, NY, 2021) filter was run to eliminate compounds with poor pharmacokinetics and violate Lipinski's rule of five [75]. Glide employs OPLS4 [67] forcefield parameterization for docking calculations. Although the SP mode predicts good ligand binding, the XP scoring function filters out false positives with poor pharmacokinetics. Of the 29 compounds filtered through QikProp, only 14 proceeded to the SP docking mode, and only six of the best binding ligands passed through to XP docking. Molecules with binding XP scores below that of metforminH$^+$ (-1.325 kcal/mol) were selected for further studies.

2.5. Quantum mechanics polarised ligand docking (QPLD) [76–78]

The six compounds that gave the best binding (Fig. 1) were subjected to an enriched docking method of QPLD [76] analysis (Schrödinger Release 2022–1: QM-Polarized Ligand Docking protocol; Glide, Schrödinger, LLC, New York, NY, 2021; Jaguar, Schrödinger, LLC, New York, NY, 2021; QSite, Schrödinger, LLC, New York, NY, 2021). In QPLD, the quantum mechanical and molecular mechanical (QM/MM) calculations are integrated. There are three steps involved in QPLD, the normal Glide SP scoring is the first step. The second step entails replacing ligand partial charges with the field of the protein for the complex, followed by QM calculation to monitor the changes. The B3LYP density functional theory and 6–31G**/LACVP*+ basis sets are employed by default in QPLD. The QM region was estimated in the accuracy level of ultrafine SCF (iacc =1, iac-scf = 2). In the final step of QPLD, the ligands were redocked with the updated atomic charges employing Glide XP and QPLD. The compounds are finally ranked on calculated MMGBSA binding free energies of five generated poses per QPLD redocking pose.

2.6. DFT

The stereo-electronic features of the top three binding phytoconstituents, along with metforminH$^+$ as a standard, were predicted by DFT calculations. The computations were carried out in the Gaussian 09 program [58]. The compounds were optimized using the Truhlar's Minnesota (M06–2X) functional [79], with the split valence triple ζ 6–311++*G*(d,p) basis set. The geometry optimizations were carried out at 298.15 K in vacuum. Vibrational frequency calculations were performed at the same level of theory to confirm the optimized geometries as real minima without imaginary frequencies. Further, employing the gas phase optimized structures, solvent phase minimizations were carried out in the water (ε = 78.355) to observe the behaviour of these compounds under solvation. The Polarizable Continuum Model (PCM) water solvation system was employed for molecular processing. The solvation energy was calculated using the universal SMD solvation model.

2.7. Drug-likeness [80,81] prediction and ADMET profiling

The top six molecules (Fig. 1) selected based on QPLD scores were subjected to drug metabolism and pharmacokinetic investigation. The QikProp module (Schrödinger Release 2022–1: QikProp; Schrödinger, LLC, New York, NY, 2021) in the Maestro interface was used to predict the drug-like properties of the six ligands. Properties such as absorption, distribution, metabolism, and excretion were calculated in the accurate prediction mode. Hydrogen bond donor (HBD), hydrogen bond acceptor (HBA), the predicted octanol-water partition coefficients (QPlogPo/w), the van der Waals surface area of polar N and O atoms (PSA), predicted human serum albumin binding (QPlogKhsa) and Lipinski's rule of five violations, were calculated. Further in this process, calculated central nervous system activity (CNS), predicted IC_{50} value for HERG K^+ ion channels (HERG), predicted apparent Caco-2 cell permeability (CaCo), Madin-Darby Canine Kidney (MDCK) cell line permeability, skin permeability (log K_P), aqueous solubility (log S) as well as % human oral absorption, were estimated. The respective numbers of reactive functional groups (#rtvFG) and of possible metabolic reactions were also computed.

2.8. Molecular dynamics (MD) simulations

The minimized holo 4L7F complexes were prepared for molecular dynamics using the system builder module of Maestro software. Desmond [82] software (Schrödinger Suites 2022–1: Desmond, Schrödinger, LLC, New York, NY, 2021) was used to perform MD simulations employing the generated systems. The OPLS4 forcefield [67] was employed to determine the ligand's interactions with the receptor, solvated with the simple point charged (TIP-3P) water model [83,84]. An orthorhombic water box modelled a 10 Å buffer region between the atoms on the receptors and box sides. The box's volume was minimized, and the overall charge of the system was neutralized by adding either Na^+ or Cl- counter ions.

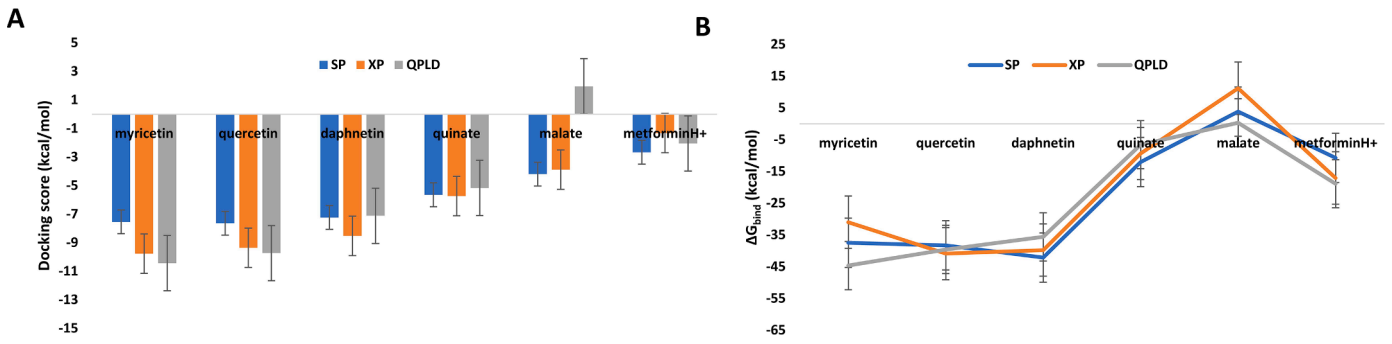


Fig. 3. (A) Docking scores for forcefield and QM/MM protocols and (B) Comparison of MMGBSA for docked complexes.

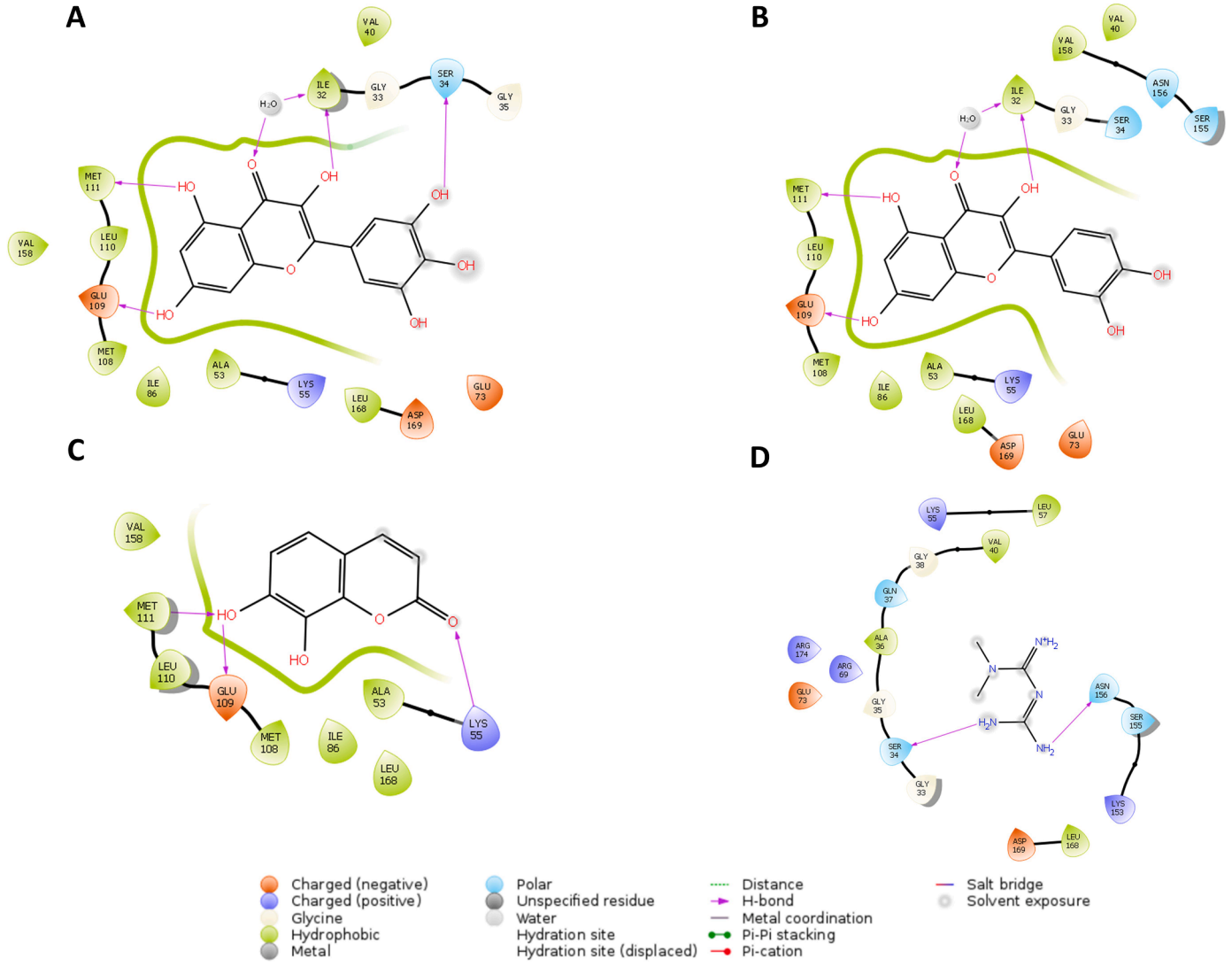


Fig. 4. SP docking 2D Ligand interaction of (A) Myricetin (1, CID 5281672); (B) Quercetin (2, CID 5280343); (C) Daphnetin (3, CID 5280569) and (D) MetforminH$^+$ (6, CID 4091) against 4L7F.

The steepest descent (SD) and limited memory Broyden-Fletcher-Goldfarb-Shanno (LBFGS) algorithms, with a maximum of 2000 iterations, were executed for the minimisation and stepwise system relaxation. The salt concentration of the system was adjusted to 0.15 M NaCl to mimic the biological salinity using the S-OPLS forcefield. The temperature was kept constant at 300 Kelvin using the Nose–Hoover thermostat method [85]. The pressure was constant at 1.01325 bar through the Martyna–Tobias–Klein barostat set to 2.0 ps relaxation time in isotropic coupling style. The simulations were performed using the isothermal-isobaric (NPT) ensemble by considering the number of atoms, pressure, and the simulation time at 100 nanoseconds. Particle mesh Ewald method (PME) was used to evaluate long-range coulombic interactions with a cut-off of 9 Å. The captured frames of simulation trajectories were saved and recorded at every 100 ps interval. The

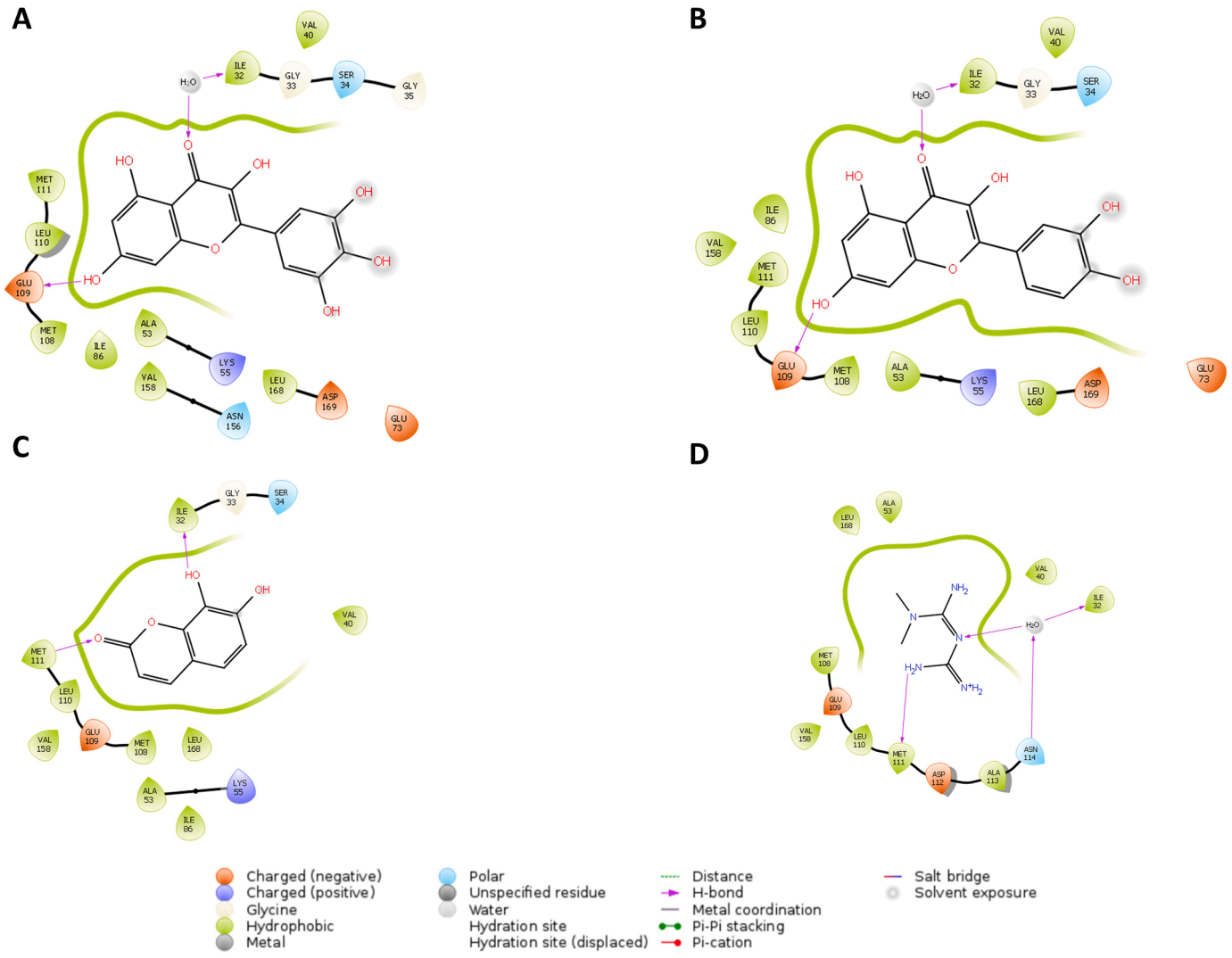


Fig. 5. XP docking 2D Ligand interaction of (A) Myricetin (1, CID 5281672); (B) Quercetin (2, CID 5280343); (C) Daphnetin (3, CID 5280569) and (D) MetforminH^{+} (6, CID 4091) against 4L7F.

trajectories from MD simulations were further analysed according to RMSD, RMSF, protein contacts and ligand contacts in the simulation interactions diagram module.

2.9. Ligand binding free energy analysis through MMGBSA

Molecular mechanics with generalised Born surface area solvation (MM-GBSA) of the relative free energy of the selected six ligands were carried in the Prime [86] MM-GBSA module (Schrödinger Release 2022–1: Prime; Schrödinger, LLC, New York, NY, 2021). Further in the study, the thermal_mmgbsa.py script from the Prime module was used to split Desmond MD trajectories into individual snapshots for the ΔG binding analysis. The Prime binding energies and ligand strain are calculated employing the S-OPLS forcefield [74] in the Glide pose viewer file. Prime combines the surface generalized Born solvation mode for polar (GSGB) and non-polar (GNP) solvation models, as well as molecular mechanics energies (EMM) that compile various nonpolar solvent accessible surface area and van der Waals. The free energy changes brought by ligand binding is estimated according to the equation [87]:

$$\Delta G_{bind} = G_{complex} - \left[G_{protein} + G_{ligand}\right]$$

$$G = EMM + GSGB + GNP$$

where, $G_{complex}$ indicates the free energy of the protein-ligand complex, $G_{protein}$ and G_{ligand} denote the minimised energy values of protein and ligand, respectively.

2.10. Pharmacophore hypothesis

The top three QPLD-screened active molecules were employed as the basis for generating the theoretical phase of the pharmacophore. The Phase [88] application of Schrödinger was used to generate pharmacophore sites from the MMGBSA post-processing poses. Up to five pharmacophoric features as vectors of chemical attributes were generated per pose. The retained features include hydrogen-bond donor (D) and acceptor (A), rings (R) representing aromatic regions, negative ionisable (N), and positive ionizable(P).

3. Results and discussion

3.1. Forcefield molecular docking

In this study, we employed Glide [73] standard precision (SP) and extra precision (XP) sampling methods to investigate the binding affinities of ligands derived from *T. officinale* against JNK1. The results ranked in two scoring functions (docking score and Glide Gscore) are

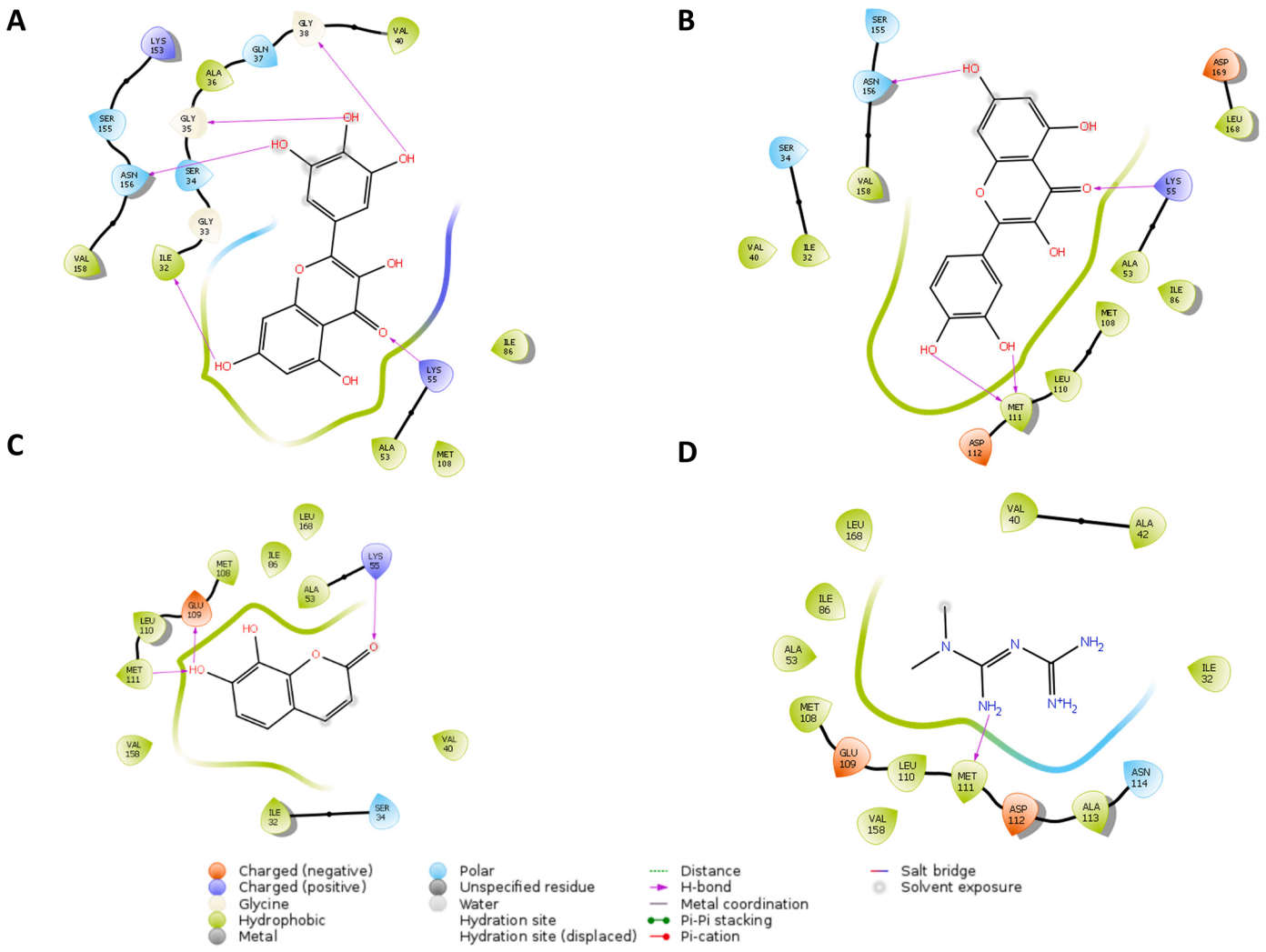


Fig. 6. QPLD 2D Ligand interaction of (A) Myricetin (1, CID 5281672); (B) Quercetin (2, CID 5280343); (C) Daphnetin (3, CID 5280569) and (D) MetforminH$^+$ (6, CID 4091) against 4L7F.

summarized in Tables 2 and 3. From the 19 input ligands, Ligprep generated a library of 29 different protomers and tautomers docked in the SP mode. To evaluate the validity of the docking procedure, native ligand redocking was performed. The co-crystalized ligand was isolated before docking and further redocked in the active site and the RMSD of the two poses was calculated. The calculated superimposition RMSD was 0.2334 Å, well below the 2 Å threshold for natural state estimation [89]. Subsequently, all the compounds retained in the SP scoring algorithms were redocked in the XP paradigm. The docking scores ranged from -7.641 (myricetin) to -2.668 kcal/mol (metforminH$^+$) in SP to -9.769 (myricetin) and -1.325 kcal/mol (metforminH$^+$) in XP. The summary of the forcefield-based docking is displayed in Tables 2 and 3.

In both the SP and XP protocols, myricetin, quercetin, and daphnetin interacted strongly with JNK1 compared to metforminH$^+$. In SP (Fig. 4), myricetin showed six polar hydrogen bonds with residues Ile32/H_2O (2.47, 1.87 Å), Ile32(2.28 Å), Glu109 (1.91 Å), Ser34 (2.03 Å) and Met111 (2.31 Å). One π-sulfur interaction with Met108 (5.00 Å) and eight π-alkyl with residues Ala53 (3.52, 4.82 Å), Val158 (4.49, 5.40 Å), Leu168 (4.72, 4.77, 5.08 Å) and Val40 (4.46, 5.16 Å) (**Fig. S3**). In the XP mode (Fig. 5), three hydrogen bonds were observed between myricetin and Ile32/H_2O (1.75, 2.47 Å) as well as with Glu109 (1.91 Å). Two π-sulfur interactions with Met108 (4.84, 5.55 Å) and seven π-alkyl interactions with amino acids Ala53 (3.56, 5.12 Å), Val158 (4.64 Å), Leu168 (4.54, 4.92, 4.96 Å) and Val40 (4.31 Å) were also observed (**Fig. S4**). In SP, quercetin interacted through five hydrogen bonds with residues Ile32/H_2O (2.47, 1.76 Å), Ile32 (2.22 Å), Glu109 (1.80 Å) and Met111 (2.31 Å). Further in the SP mode, quercetin showed two π-sulfur interactions with Met108 (5.03, 5.71 Å) and seven π-alkyl interactions with Ala53 (3.59, 4.83 Å), Lys55 (5.16 Å), Val158 (2.92 Å) and Leu168 (4.58, 4.71, 5.11 Å). In XP, there were three hydrogen bonds between quercetin and amino acids Ile32/H_2O (1.89, 2.47 Å) and Glu109 (1.66 Å). Further, one π-σ interaction was observed with Val158 (2.92 Å) while seven noncovalent π-alkyl interactions were formed with residues Ala53 (3.59, 4.83 Å), Lys55 (5.16 Å), Val158 (2.92 Å) and Leu168 (4.58, 4.71, 5.11 Å).

For daphnetin in SP, there was a total of three polar hydrogen bonds with residues Lys55 (2.64 Å), Glu109 (2.24 Å) and Met111 (2.04 Å). One π-σ interaction with Val158 (2.90 Å), two π-sulfur interactions with Met108 (4.77, 5.31 Å) and five π-alkyl interactions with residues Ala53 (3.77, 5.00 Å), Leu168 (4.08, 5.04 Å) and Val40 (4.48 Å). Furthermore, in XP, daphnetin showed two hydrogen bonds with residues Ile32 (2.79 Å) and Met111(1.74 Å). One π-σ was observed with Val40 (2.92 Å) and five π-alkyl hydrophobic interactions formed with amino acids Ala53 (3.54, 4.89 Å), Val158 (4.57 Å) and Leu168 (4.37, 4.89 Å). Contrary to the phytocompounds, the metforminH$^+$ tautomer showed the least number of interactions in both SP and XP. Two hydrogen bonds with amino acids Ser34 (1.86 Å) and Asn156 (2.00Å) were observed in SP for metforminH$^+$. Only residues Ile32/H_2O (2.38, 2.47 Å) and Met111 (1.90, 2.24 Å) interacted with metforminH$^+$ in the XP mode.

The top three *T. officinale* compounds (**1, 2** and **3**) possess a potential

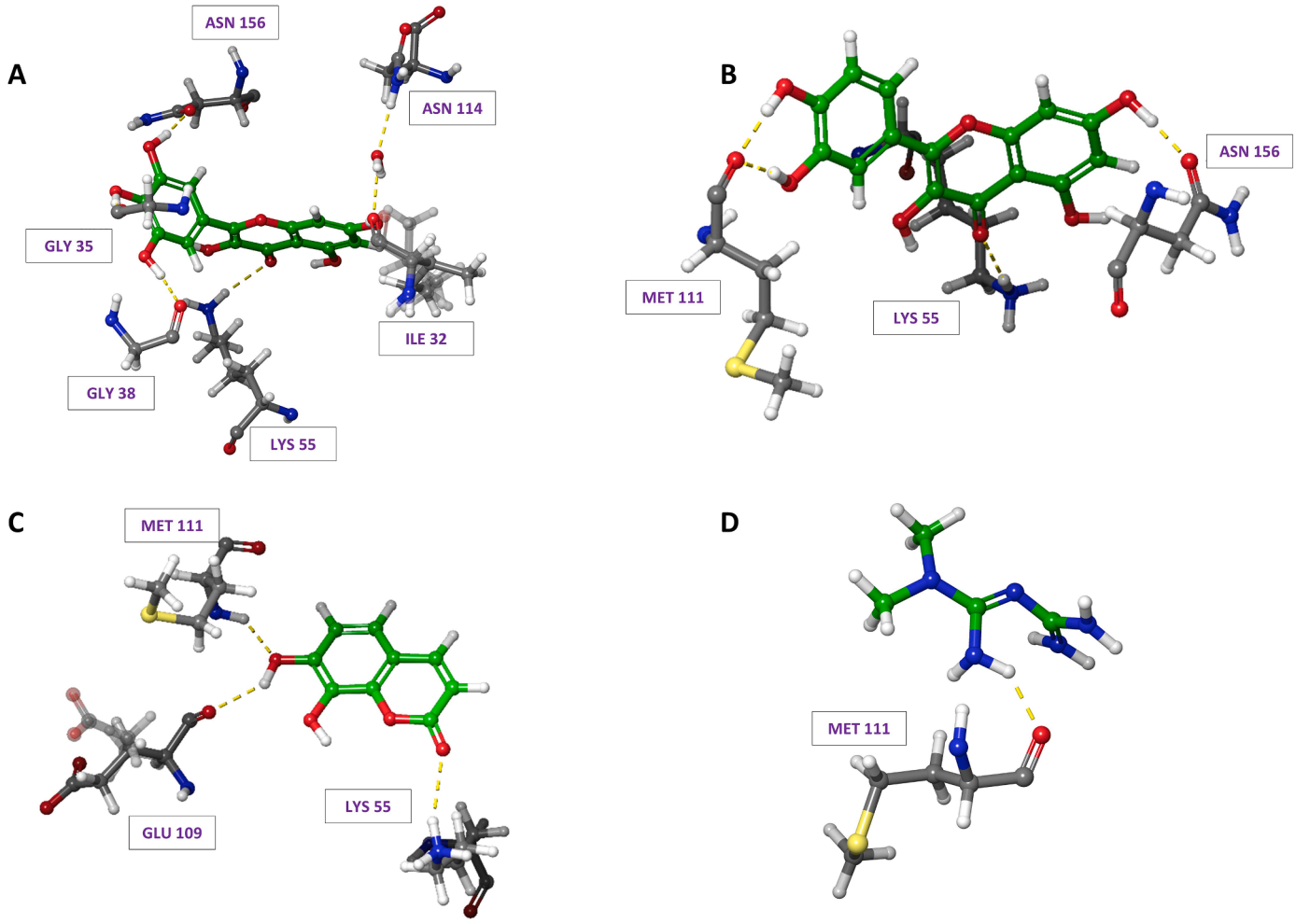


Fig. 7. Residues in QPLD docked pose interactions of (A) Myricetin (1, CID 5281672); (B) Quercetin (2, CID 5280343); (C) Daphnetin (3, CID 5280569) and (D) MetforminH$^+$ (6, CID 4091) against 4L7F.

for inducing a modulatory response in JNK1, as they all show interactions with the gatekeeper residue Met108. This amino acid is in the adenosine triphosphate (ATP)-binding pocket and is known to control the selectivity of the receptor kinase [90]. Fig. 2 shows the ATP-binding cleft in the centre of the bi-lobal (C- and N-termini) domain architecture of JNK1. The ATP-binding site consists of the entirety of the active site residues. The occupancy of the ATP-binding site has been experimentally shown to modulate the affinity of JNKs to its upstream activators, such as MAPK kinases (MKK4 and/ MKK7) and JNK-interacting proteins [91]. The active site residues belonging to the ATP-binding pocket that were found to interact with JNK1 include Ile32, Ser34, Met111, Met108 and Glu109. Residue Leu168 resides in the activation loop of JNK1 and belongs to the active site. Amino acids Val40 and Ala53 constitute the hydrophobic adenine-binding pocket. Hydrogen bonds were also observed with Lys55, another residue that blocks the ATP-binding site, thereby dysregulating JNK1 activity. The interaction of the studied ligands extends to all the biologically pertinent regions of JNK1, such as the ATP-binding site, the kinase interaction motif, the active site, the polypeptide substrate binding site, and the activation loop.

3.2. QPLD

While the accuracy of molecular mechanics-based forcefields in nonstandard residue parameterization is practical, protein environments induce charge polarization. Considering the role of charge polarization by placing *ab initio* partial charges on ligands has been shown to improve docking accuracy [76]. The QPLD scores for the five best docking compounds and protonated metforminH$^+$ are shown in Table 4. Among these, myricetin, quercetin and daphnetin had the best QPLD scores of -44.65, -39.58 and -35.62, respectively, compared to -18.88 kcal/mol for the standard metforminH$^+$. In all the systems, there was an enhancement in binding, as shown by the enriched binding scores and lower binding energies (Fig. 3A). The comparison of Glide Gscores and docking MMGBSA obtained from XP and QPLD are shown in Fig. 3B. The full decomposition of docking MMGBSA energetics is shown in Table S2. There is a good agreement between the XP and QPLD-derived MMGBSA energies. To further investigate the improved docking accuracy and enrichment by QPLD, the native ligand was redocked. We calculated the difference between the most common structure alignment RMSDs of the redocked and crystallized versions of the native ligand (Table S1). The alignment (Fig. S2) RMSD for XP was 0.281 and 0.160 Å for QPLD. The threshold for good docking is assumed to be <2 Å [89]. From the alignment of RMSDs, it can be inferred that the native ligand reasonably assumed the natural state in both XP and QPLD. However, the QPLD protocol presented a better natural state pose. Employing quantum mechanical partial charges in determining the bound ligand's conformation enhances the docking accuracy of polar protein systems [77].

There were two distinct hydrogen bonding patterns for polar neutral and for charged ions. While the hydrophobic moieties interacted in the vicinity of the same hydrophobic pocket (Figs. S5 and S7). The charged functional groups were redefined in QPLD. Chung *et. al.* [92] studied the forcefield and QM-based charge typing on the carboxylate ion in Glide

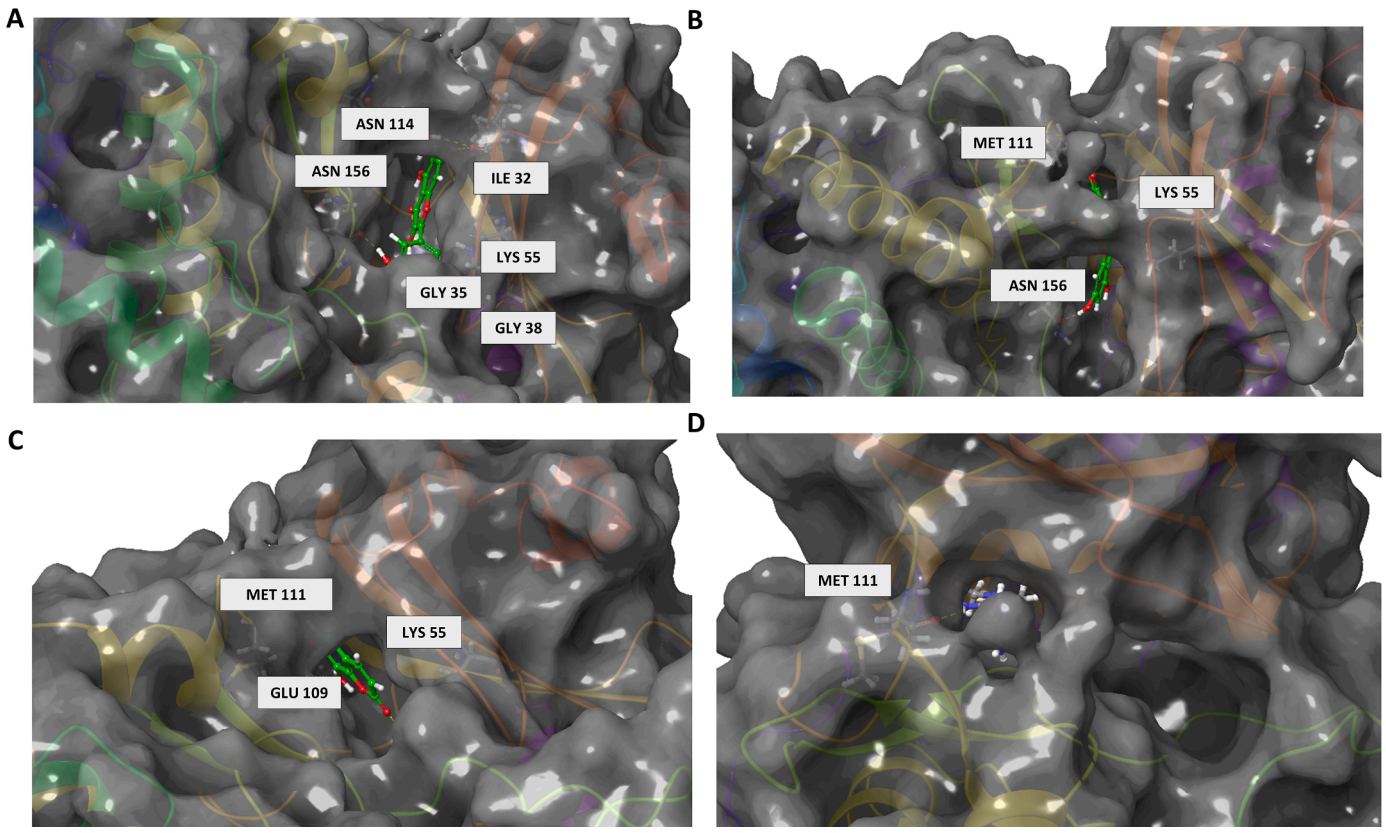


Fig. 8. QPLD Docked ligands of (A) Myricetin (1, CID 5281672); (B) Quercetin (2, CID 5280343); (C) Daphnetin (3, CID 5280569) and (D) MetforminH$^+$ (6, CID 4091) in 4L7F cavity.

XP and in QPLD. They found that the OPLS forcefield symmetrically charged the two carboxylate oxygens to -0.8e. From QM/MM calculation the charges of the two oxygens were ordered unequally to -0.95 and -0.76e, yielding distinct hydrogen bonding arrangements [92]. This observation was consistent with our results, the OPLS forcefield configured all four charges of the malate ion (**4**) carboxylate oxygens to -0.8e. The QM/MM differentiated these charges to -0.759 and -0.789e for the α carboxylate and -0.775 to -0.770e for the β carboxylate. A similar observation was made for the quinate ion (**5**) oxygen charges. While the OPLS forcefield symmetrical charged the two carboxylate oxygens to -0.8e in Glide, the QM charges were -0.732 and -0.713e in QPLD.

To study the hydrophilic nature of the binding site we followed the hydrogen dependence of the *T. officinale* best three compounds. While only eight total hydrogen bonds are observed for XP docking (Table 3), there were 12 hydrogen bonds in QPLD (Table 4, Fig. 6–8) with residues Asn114, Ile32, Ser34, Met111, Asp112, Glu109, Gly38 and Glu73. The non-hydrogen bonding interactions remained the same (Fig. S5). This is consistent with the previous reports that show that QPLD improves Glide XP poses through accurate charge placements. The explicit catalytic water within 5 Å was found to have a critical role in ligand binding the ligand as observed for residue Ile32/H_2O complexes (Fig. 4). This is consistent with the crystal structure of the native ligand (AX13587) complexed to PDB:4L7F where water was found to form a complex with Asn156.

3.3. DFT

The electronic properties, chemical stability, and reactivity of the three best phytoconstituents and metforminH$^+$ (**1, 2, 3** and **6**) were estimated through frontier molecular orbitals (FMOs) analysis. The optimized structures of **1, 2, 3** and **6** are shown in Fig. 9. FMOs such as the highest and lowest occupied molecular orbitals (HOMO and LUMO) indicate the possible nucleophilic and electrophilic attack sites within the ligand, respectively. The chemical reactivity descriptor data is presented in Table 5, and the FMO contour surfaces are presented in Figs. 10 and 11. The energy band gap, ΔE_{gap} is the difference of LUMO and HOMO energies (E_L and E_H) correspondingly. The stability and reactivity of a small molecule is inversely proportional to the band gap. Molecules with smaller band gaps are more reactive and are probable to react with polar macromolecules such as DNA or enzymatic proteins.

All three phytoconstituents showed a slight decrease in ΔE_{gap} from gas to aqueous phases. The solvated ΔE_{gap} represents the extrinsic energy requirements for electron charge transfer to the first excited state stabilized by hydrogen bonding. Stabilization due to solvation increases E_H while lowering E_L which lowers ΔE_{gap} and provides semiconductor solutions. The ΔE_{gap} is the energy required to move an electron from the valence band to the conduction band. A decrease in solvated ΔE_{gap} indicates that these compounds are more reactive in water and are stable in the gas phase. This was the opposite for metforminH$^+$, the increase in ΔE_{gap} for metforminH$^+$ could be attributed to the positive electric field of the metforminH$^+$ solution due to the tautomer charge at pH above 7.

The relationship between a material's ΔE_{gap} in various solvation media depends on the electric field of the resultant solution if the particle size remains constant. In the phytocompounds, myricetin and quercetin showed lower values in ΔE_{gap}, with the latter having the lowest value (5.919 eV). All the studied top three phytocompounds (**1, 2** and **3**), showed insulator properties with $\Delta E_{gap} > 4$ eV [93]. Both myricetin and quercetin are flavonols (Fig. S1) with a high degree of maximum common structure. It is noted, however, that the hydroxyl at the C6' position of the pyrogallol moiety is significant for the charge transfer of myricetin. The pyrogallol is substituted with a catechol moiety in quercetin, which lacks this hydroxyl group. The ΔE_{gap} for the compounds was also studied as the number of electron states that can

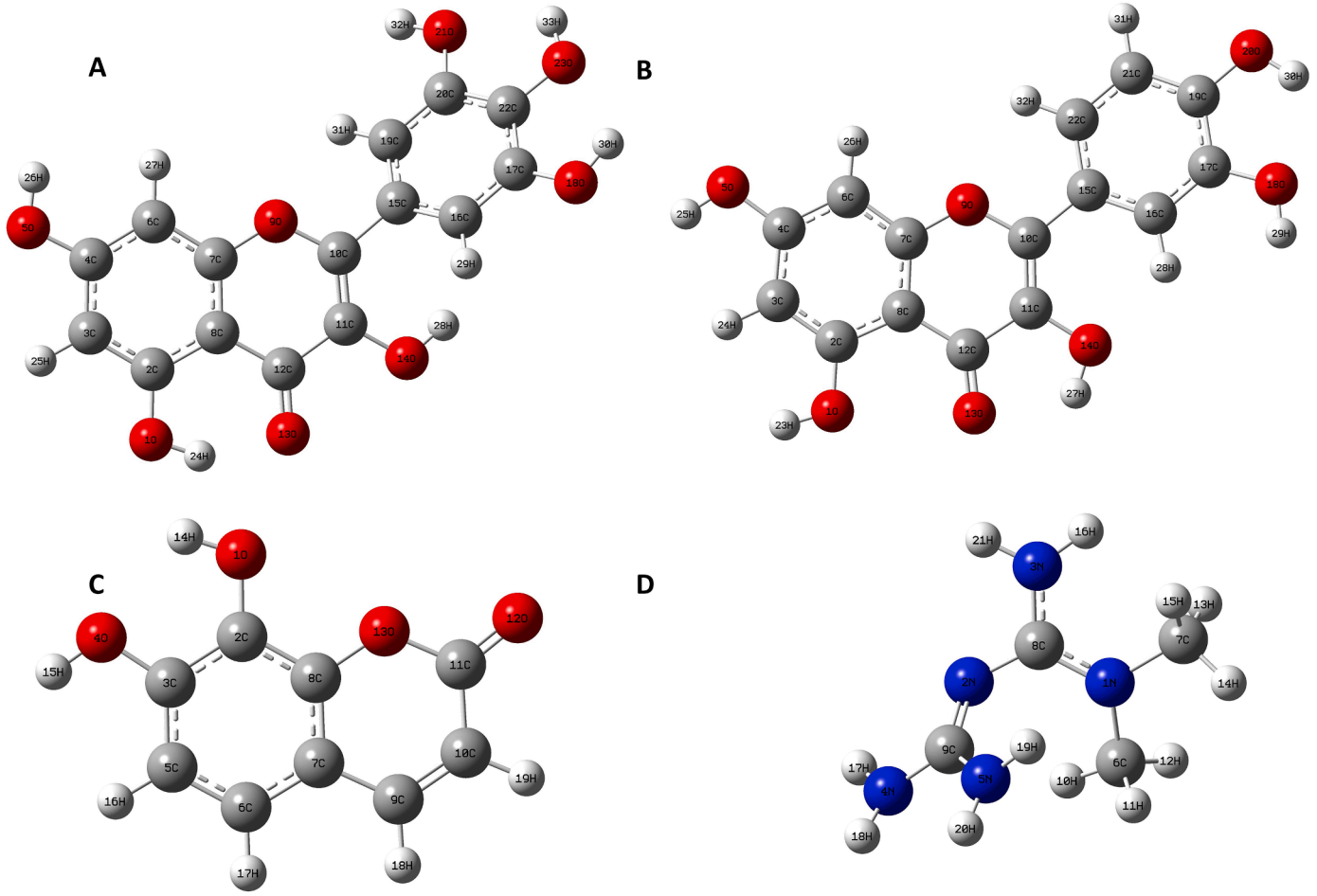


Fig. 9. Optimized structures of (A) Myricetin (CID 2518672), (B) Quercetin (CID 5280343), (C) Daphnetin (CID 5280569) and (D) MetforminH$^+$, in PCM water solvent (ε = 78.355) at M06–2X/6–311++G(d,p) level of theory.

Table 5
Quantum chemical properties of best ligands optimized in M06–2X density functional with 6–311++G(d,p) basis set.

CID (phase)	E_H (eV)	E_L (eV)	ΔE_{gap} (eV)	χ (eV)	μ (eV)	η (eV)	σ (eV^{-1})	ω (eV)	ν (eV^{-1})	I (eV)	A (eV)	E_{Tot} (Hatrees)
5281672 (g)	-7.433	-1.156	6.277	4.295	-4.295	3.138	0.1593	2.938	0.3403	10.92	1.156	-1179.316
5281672 (w)	-7.451	-1.284	6.168	4.367	-4.367	3.084	0.1621	3.093	0.3234	6.689	1.284	-1179.341
5280343 (g)	-6.990	-1.070	5.920	4.030	-4.030	2.960	0.1689	2.743	0.3646	6.990	1.070	-1104.085
5280343 (w)	-7.182	-1.263	5.919	4.222	-4.222	2.959	0.1690	3.012	0.3320	7.182	1.263	-1104.12
5280569 (g)	-7.765	-1.062	6.704	4.414	-4.414	3.352	0.1492	2.906	0.3441	7.765	1.062	-647.4
5280569 (w)	-7.696	-1.164	6.532	4.430	-4.430	3.266	0.1531	3.005	0.3328	7.696	1.164	-647.419
4091* (g)	-12.61	-3.736	8.870	8.171	-8.171	4.435	0.1127	7.527	0.1329	12.61	3.736	-433.162
4091* (w)	-8.950	-2.629	6.321	5.789	-5.789	3.161	0.1582	5.302	0.1886	8.950	2.629	-433.238

* MetforminH$^+$, (g) gas-phase, (w) water-solvation, E_{Tot} = total energy

coexist at a specific Fermi level, referred to as the density of states (DOS) [94]. DOS is calculated as the number of electron states per unit of energy. The HOMO/LUMO energy gap can be visualized in DOS spectra in Fig. 12.

Electronegativity (χ) is a quantity introduced by Linus Pauling as the power of an atom or atom groups to accept electrons [95]. Mulliken quantified χ as the average of the chemical potential (I) and the electron affinity (A) [96]. Molecules with larger electron affinities and ionization potentials are said to be more electronegative. In both the gas phase and in water solvation, the phytoconstituents showed larger electronegativities compared to metforminH$^+$ (Table 5). The descending order of electronegativities in water solvation was daphnetin > myricetin > quercetin > metforminH$^+$. The reduced electron cloud improves the electron distribution of daphnetin due to the lack of the activated phenyl moieties present in the two flavonols (**1** and **2**), resulting in high electronegativity.

Global hardness (η) describes the molecule's ability to resist charge transfer. Therefore, molecules with larger η are chemically stable. The maximum hardness principle (MPH) specifies a positive correlation between stability and hardness at a constant potential [97]. Half the inverse of η is the chemical softness (σ) described as the molecule's proneness to charge transfer. Both η and σ are used to quantify chemical stability and reactivity respectively. Among the phytocompounds, daphnetin had the highest η (3.27 eV) and lowest σ (0.15 eV^{-1}) in water. Inversely, quercetin displayed the lowest η (2.96 eV) and highest σ (0.17 eV^{-1}) under solvation. It can then be inferred that quercetin is the softest molecule, most reactive and less prone to charge transfer. Daphnetin was calculated to be a harder and less reactive ligand. There was a slight

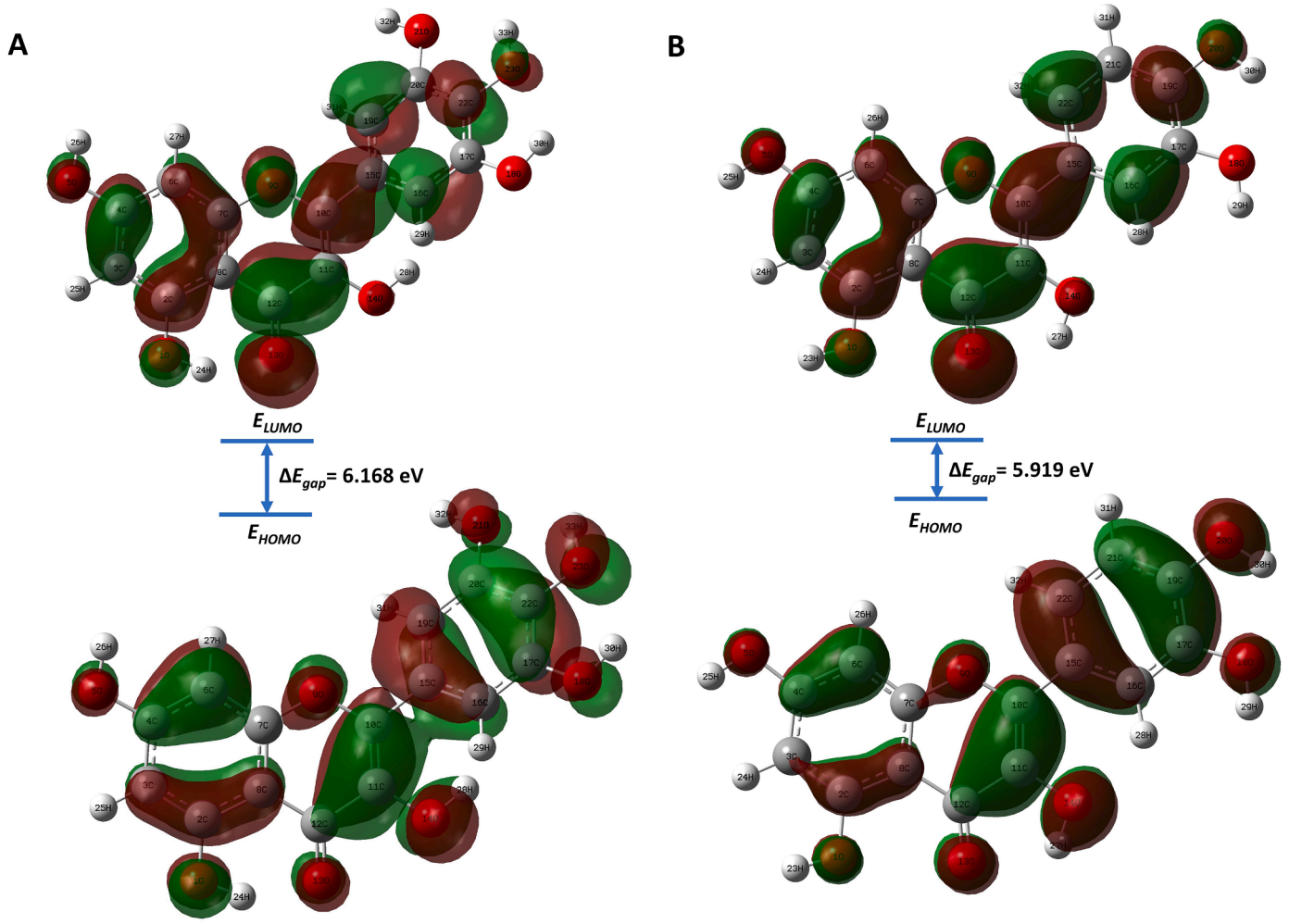


Fig. 10. HOMO-LUMO of (A) Myricetin (1, CID 5281672) and (B) Quercetin (2, CID 5280343) at M06–2X/6–311++*G*(d,p) in PCM water solvent (ε = 78.355).

change of η and σ under solvation. This minute shift suggests that solvation has less influence on the hardness and softness of the studied compounds at this level of theory.

The average sum of E_L and E_H gives the chemical potential μ, quantifying the energy a molecule gives off upon reaction. This value relates to the change in energy resulting from varying electron density and is also evaluated as minus electronegativity [98]. The μ values for the extracts ranged from -4.2 to -4.4 eV in water. The range was -4.0 to -4.4 eV in the gas phase, further confirming the higher reactivities of these compounds under solvation.

Global electrophilicity index (ω) and nucleophilicity index (ν) are chemical descriptors that quantify a molecule's stability when reduced or oxidized, respectively. There was a slight increase in the electrophilicity index for all the neutral molecules in water compared to the gas phase. Under solvation, all the isolates have roughly similar ω of 3.0 eV and ν of 0.3 eV^{-1}. This shows that these compounds are strongly nucleophilic (ω > 1.5 eV) [93] and slightly electrophilic in water.

The electrophilicity index measures the electrophilic power of an atom or a molecule towards a nucleophile; large indices represent higher reactivity as an electrophile. Of all the global descriptors (η, σ and μ), ω is considered the most significant in predicting the reactivity of molecules [99]. As a result of the positive formal charge on protonated metforminH$^+$, the gas-phase ω is highest (7.53 eV) due to increases in intrinsic electrophilicity. However, under solvation, since the hydrogen bonding stabilizes the charge, solvated metforminH$^+$ shows a reduced ω (5.30 eV).

The energy requirements for a molecule to lose an electron is quantified as ionization potential (I). MetforminH$^+$ displayed the highest value of I in the gas phase. This I estimates the energy of the second ionization of metforminH$^+$. As a cation in gas-phase, metforminH$^+$ has the least efficiency for HOMO hole injection as the positively charged molecules are exposed to each other. This is not the case in water, where hydrogen bonding stabilizes the charge. All the neutral compounds displayed a lower I value than metforminH$^+$ except for myricetin at the gas phase. In water, myricetin exhibited the lowest value of I (6.689 eV).

The value of solvated I is related to nucleophilicity. Solvated I is directly proportional to the thermodynamic oxidation potential of any chemical species, and a positive value indicates spontaneity [100]. The energy released during reduction is estimated as electron affinity A and is directly proportional to the thermodynamic reduction potential. The value of A partially estimates the electrophilicity of a chemical entity [100]. In water, myricetin showed a relatively higher A value (1.28 eV), which also confirms the significance of hydroxyl of the pyrogallol in charger transfer and reactivity.

3.3.1. Fukui indices and charge population

Fukui indices were used to investigate the reactivity of the optimized top-hit compounds (**1, 2** and **3**) and metforminH$^+$(**6**). The optimized parameters, such as coordinates, bond angles and bond lengths, are presented in Tables S4, S7, S10 and S13. Fukui indices (f^-, f^0, f^+ *and* $f^{(2)}$) are used to estimate the local susceptibilities of molecules upon global perturbation. Three energy calculations were performed for each compound at different charge states and corresponding multiplicities to

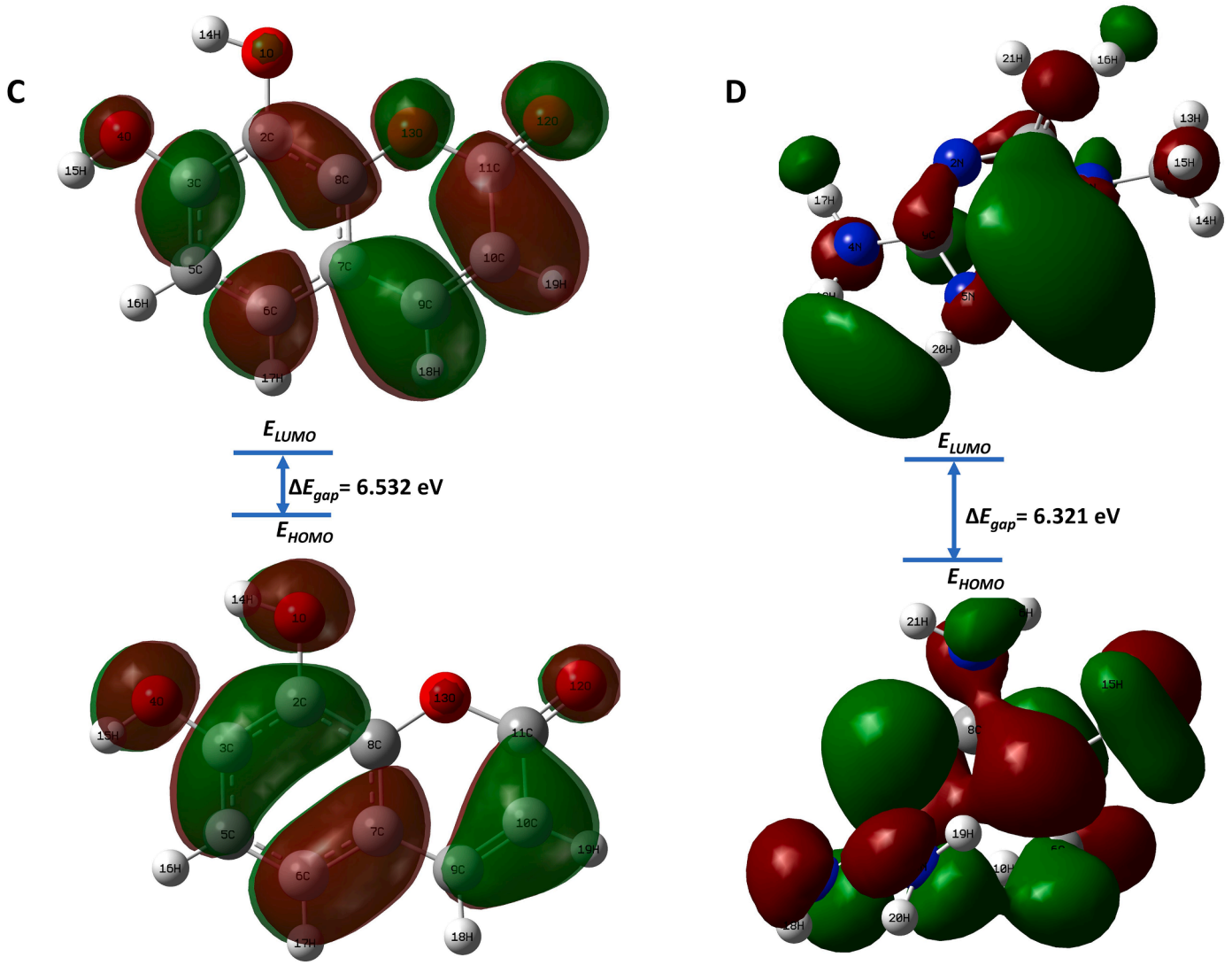


Fig. 11. HOMO-LUMO of (C) Daphnetin (3, CID 5280569) and (D) MetforminH$^+$ (6, CID 4091) at M06–2X/6–311++*G*(d,p) in PCM water solvent (ε = 78.355).

account for the charge density relaxation due to molecular charge changes. The charge states refer to the neutral, cationic and anionic states (N0, N-1 and N+1). The full Fukui indices and natural population analysis list is presented in Tables S8, S11 and S14. Population analysis and Fukui indices are used to estimate sites of chemical reactivity. Regions with negative charges are known to be susceptible to electrophilic attacks. Larger values of f^+ indicate electrophilic regions, while larger f^- values relate to nucleophilicity. Fig. 13 shows the alignment of the f^+ and charge distribution, which estimate the atomic electrophilicity of molecules.

For myricetin (Fig. 13A), charge analysis of the optimized structure showed that all the protons bear positive charges. The hydroxylic protons (H24, H26, H28, H30, H32 and H33) possessed the highest values of positive charge compared to those bonded to carbons (H25, H27, H29 and H31). H24 shows a more positive charge among the hydroxylic protons, suggesting a possible charge transfer at this position. Carbons generally represented electron-deficient regions, except for carbon nuclei in electron-dense environments (C3, C8, C15 and C16). All carbons were positively charged except for electron-rich carbons, which were all negatively charged. Carbons C10 and C12 represent regions of highest electrophilicity. All types of oxygen (hydroxylic, carbonyl and ether) were negatively charged in myricetin. The order of charge is carbonyl (O13) > hydroxyl (O1, O5, 014, O18, O21 and O23)> ether (O9).

In quercetin (Fig. 13B), all the protons are positively charged with hydroxyl protons (H23, H25, H27, H29 and H30) having higher charges than carbon-bonded hydrogens (H24, H26, H28, H31 and H32). Among the hydroxylic protons, H27 showed a possible charge stabilization. Two patterns of carbon charges were observed. In electron-deficient regions where carbons are directly bonded to oxygens, the charge of carbon is positive and negative, whereas carbons are bonded to hydrogens instead. Among the electron-deficient carbons, nuclei C10 and C12 were the most electrophilic. The oxygens of quercin were all negatively charged; the carbonyl oxygen (O13) was the most electrophilic and bore the least charge. The ether oxygen (O9) bears the highest charge among all oxygens and is more electrophilic than all hydroxyl oxygens.

The protons in daphnetin (Fig. 13C) were all positively charged. Hydroxylic protons (H14 and H15) recorded the highest values of positive charges compared to carbon-bound hydrogens (H16, H17, H18 and H19). Carbons directly bonded to electronegative heteroatoms, and those in negative resonance regions (C2, C3, C8, C9 and C11) were all positively charged. The electron-rich carbon atoms (C5, C6, C7, and C10) were all negatively charged. Nuclei C3, C6, C9, C10, C11, O12 and O13 were the most electrophilic.

In metforminH$^+$ (Fig. 13D) all the protons bonded to nitrogen (H16, H17, H18, H19 and H20) were more positive than the carbon-bonded protons (H10, H11, H12, H13, H14 and H15). The carbons of metforminH$^+$ in electron-poor environments (C8 and C9) were highly

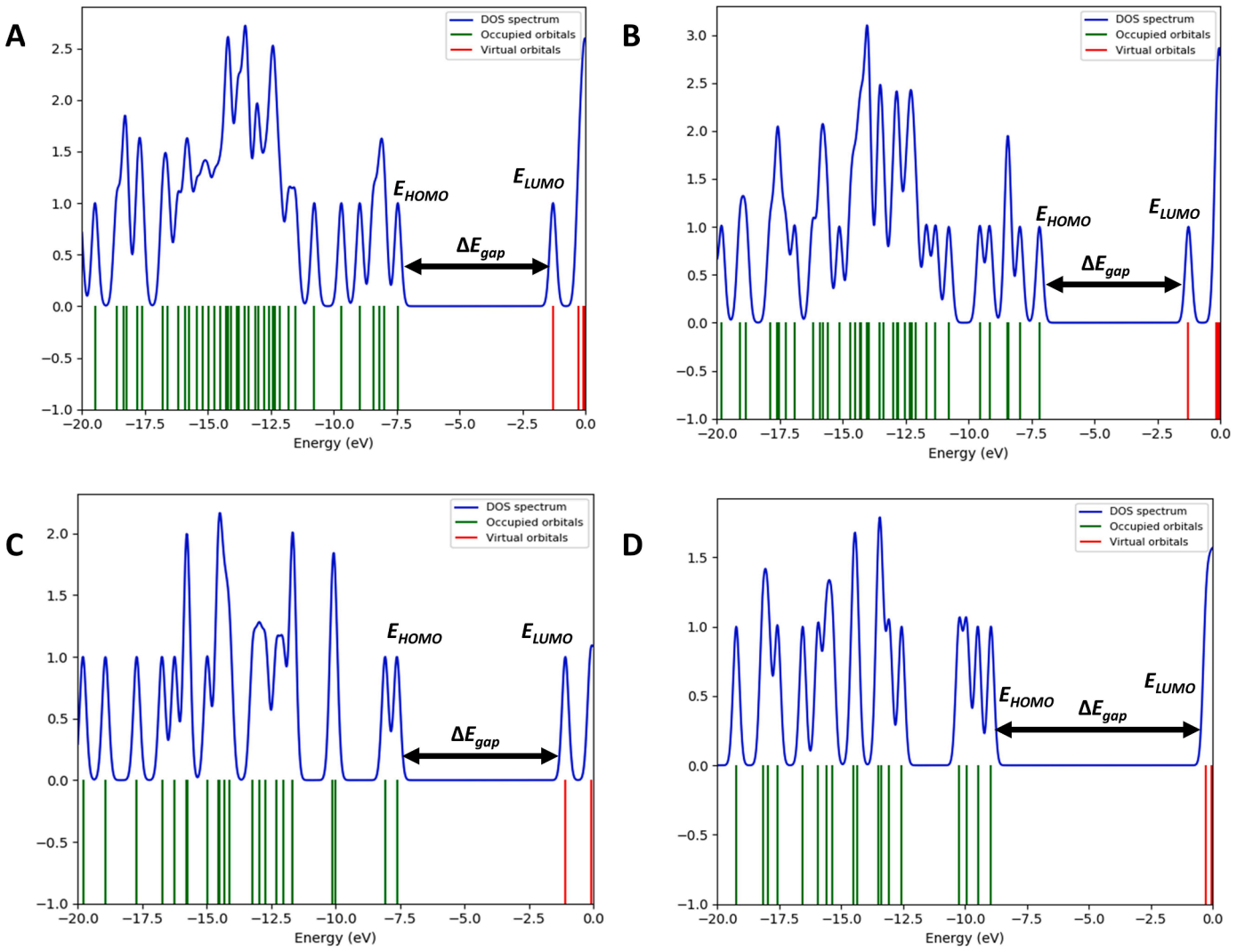


Fig. 12. Density of states spectra of (A) Myricetin (CID 2518672), (B) Quercetin (CID 5280343), (C) Daphnetin (CID 5280569) and (D) MetforminH^+, in PCM water solvent (ε = 78.355) at M06–2X/6–311++G(d,p) level of theory.

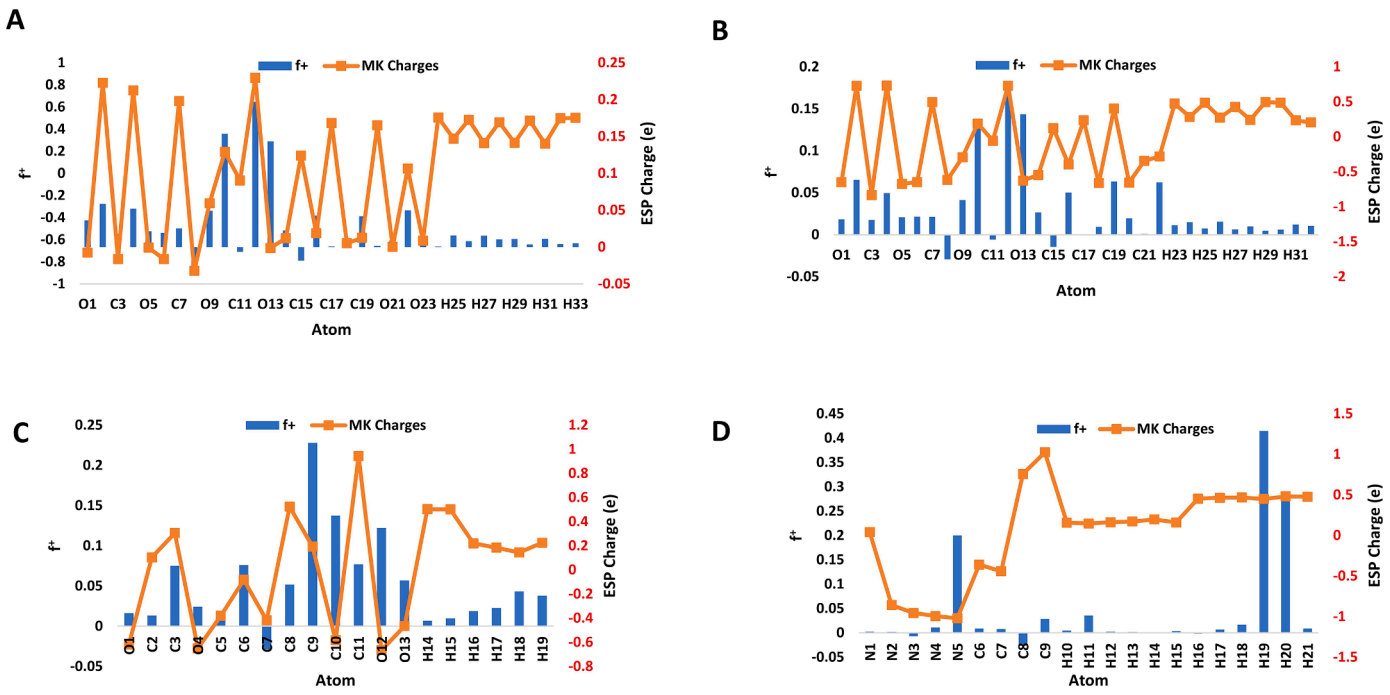


Fig. 13. Fukui indices and MK ESP population analysis of (A) Myricetin (1, CID 5281672); (B) Quercetin (2, CID 5280343); (C) Daphnetin (3, CID 5280569) and (D) MetforminH^{+} (6, CID 4091) at M06–2X/6–311++G(d,p) in PCM water.

positively charged. Carbons bonded to fewer nitrogens (C6 and C7) were less positively charged than carbon nuclei in electron-deficient regions (C8 and C9). Atoms N5, H19 and H20 were most susceptible to nucleophilic attacks.

3.3.2. MESP

The 3D molecular electrostatic potential (MESP), $V(r)$ at a point a to r, in a molecular system with nuclear charges Z_A located at R_A with an electron density $\rho(r)$, are computed with the equation [101]:

$$V(r) = mathop \sum_{A=1}^{N} \frac{Z_A}{|r\ R_A|} - \int \frac{(r')d^3r'}{|r\ r'|}$$

N is the total nuclei count, and the two terms represent the bare nuclear potential and the contributions due to electrons. The MESP of the optimized structures was studied to reveal electron-rich and electron-deficient regions. MESP regions of electrophilicity are shown in blue, and the red sites represent areas of nucleophilicity. Fig. 14 shows that the electrons were concentrated around electronegative heteroatoms, while hydrogens were regions of positive ESP.

3.3.3. Local reactivity descriptors

The changes in molecular electron density due to charge addition or removal were calculated as Fukui functions. Positive Fukui functions (f^{+}) correspond to charge addition, and negative Fukui functions (f^{-}) account for charge removal. In the generated surfaces, the green regions are positive, and the blue regions are negative. The positive f^{+} indicates electrophilicity or a region of electron gain during nucleophilic attack. Fig. 15 shows the distribution of electrophilic regions in myricetin, quercetin, daphnetin and metforminH^{+}. The negative f^{-} indicates nucleophilic regions or centres where electrons are lost when a molecule undergoes an electrophilic attack. Fig. 16 shows the various nucleophilic regions in myricetin, quercetin, daphnetin and metforminH^{+}. It can be established that the phytocompounds have pronounced nucleophilic character (blue regions). This suggests that these compounds are mostly reductants under electronic perturbation, making them applicable as antioxidants. The antioxidant nature of the isolates in contrast to metforminH^{+} was also confirmed by calculating radical Fukui functions (f^{0}), as shown in Fig. S13.

Local systems can also be studied with dual descriptors $f^{(2)}$. In this study, two methods were employed in calculating $f^{(2)}$ contours: the spin state estimation and the full electron density calculation. In the former, two states are considered (N+1 and N-1); in the latter, three states are considered (N0, N+1 and N-1). The $f^{(2)}$ simultaneously displays areas of nucleophilicity and electrophilicity upon charge disturbance Fig. 17. From our findings, for neutral ground state compounds, there is no quantitative difference between the spin state estimation and the total electron density generated $f^{(2)}$ Fig. 17 and Fig. S14.

3.3.4. Nonlinear optical properties

Most organic compounds with conjugated π systems respond nonlinearly to electromagnetic wave perturbation [102]. The consequential nonlinear optical effects can be described in terms of the dipole moment (μ_D), mean polarizability (α), anisotropy of polarizability (Δα) and the static first-order hyperpolarizability (β) according to [103]:

$$\langle \mu_D \rangle = sqrt\mu_{Dx}^2 + \mu_{Dy}^2 + \mu_{Dz}^2$$

$$\langle \alpha \rangle = frac\alpha_{xx} + \alpha_{yy} + \alpha_{zz}3$$

$$\Delta\alpha = sqrt\frac{\left[(\alpha_{xx} - \alpha_{yy})^2 + (\alpha_{yy} - \alpha_{zz})^2 + (\alpha_{zz} - \alpha_{xx})^2\right]}{2}$$

$$\langle \beta \rangle = sqrt\beta_x^2 + \beta_y^2 + \beta_z^2$$

where;

$$\beta_x = \beta_{xxx} + \beta_{xyy} + \beta_{xzz}, \beta_y = \beta_{yyy} + \beta_{yzz} + \beta_{yxx},\ \beta_z = \beta_{zzz} + \beta_{zxx} + \beta_{zyy}$$

The calculated optoelectronic properties are shown in Table 6. The prototype for calculating hyperpolarizabilities is urea ($\beta = 0.45\ x\ 10^{-30} \pm 0.12\ x\ 10^{-30}$ esu) [104]). The three top *T. officinale* compounds showed good NLO responses with larger μ_D values ranging from 5.466 – 10.82 Debye. Polarizability estimates electron distribution in molecules and is a system's important structural and orientation determination feature [105]. Compared to urea, the first-order hyperpolarizability (β)

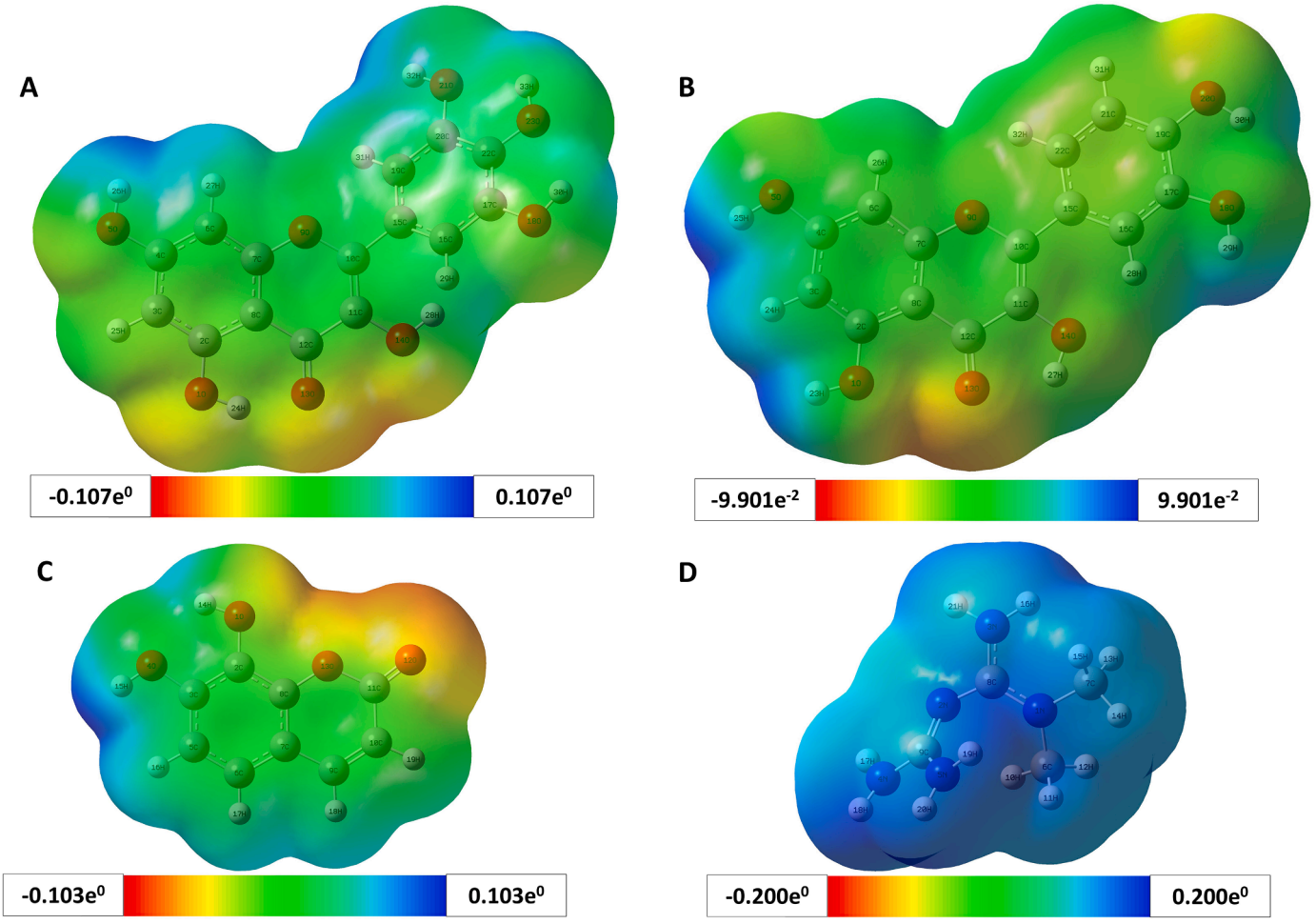


Fig. 14. MESP of (A) Myricetin (1, CID 5281672); (B) Quercetin (2, CID 5280343); (C) Daphnetin (3, CID 5280569) and (D) MetforminH$^+$ (6, CID 4091) in PCM water solvent (ε = 78.355) at M06–2X/6–311++G(d,p) level of theory.

computed was well over a factor of 10^3 for the phytocompounds at this level of theory. It can be deduced that these molecules possess a good potential as materials with nonlinear optical properties.

3.3.5. *Natural bonding orbitals (NBO) analysis*

NBO analysis is one approach for determining conjugation and charge transfer within a molecule. In NBO analysis, the data pertaining to filled and empty natural orbitals based on the Lewis structure of molecules is used to investigate intra and intermolecular interactions. The stabilization of the filled (donor) and empty (acceptor) orbitals can be computed as the second-order perturbation energies according to:

$$E^2_{i\rightarrow j^*} = -n_\sigma \frac{\left\langle \sigma_i \middle| \widehat{F} \middle| \sigma^*_j \right\rangle^2}{\varepsilon_{j^*} - \varepsilon_i} = -n_\sigma \frac{F^2_{ij}}{\varepsilon_{j^*} - \varepsilon_i}$$

where the Fock matrix element between natural bonds *i* and *j* is given by $\left\langle \sigma_i \middle| \widehat{F} \middle| \sigma^*_j \right\rangle$ or F^2_{ij}. Higher E^2 denotes pronounced interaction and stabilization between the donor and acceptor orbitals in this approach [94]. Table 7 summarises the NBO analysis of prominent charge transfers, electron density delocalization and hybridization disturbance energies of the studied molecules at M06-2X/6–311++*G*(d,p). For myricetin, similar charge transfer regimes were observed in the gas phase and under solvation. The maximum gas stabilization energy (51.68 kcal/-mol) was observed for η_2 $O_1 \rightarrow \pi^*$ $C_2 - C_3$ charge transfer. Transfers π $C_4 - C_6 \rightarrow \pi^*$ $C_7 - C_8$, η_2 $O_5 \rightarrow \pi^*$ $C_4 - C_6$ and π $C_2 - C_3 \rightarrow \pi^*$ $C_4 - C_6$ displayed perturbation energies of 44.07, 43.35 and 43.30 kcal/mol respectively. It is interesting to note that similar charge characteristics are observed in the water and the gas phase. However, under solvation, the stabilization is slightly lower with η_2 $O_1 \rightarrow \pi^*$ $C_2 - C_3$, π $C_4 - C_6 \rightarrow \pi^*$ $C_7 - C_8$, η_2 $O_5 \rightarrow \pi^*$ $C_4 - C_6$ recording stabilization energies of 48.12, 44.71 and 44.01 kcal/mol respectively. Further, in water solvation, unlike in gas, the η_2 $O_9 \rightarrow \pi^*$ $C_7 - C_8$ was found to have a stabilization energy of 41.79 kcal/mol.

In quercetin, four major charge transfers were recorded for η_2 $O_1 \rightarrow \pi^*$ $C_2 - C_3$, η_2 $O_9 \rightarrow \pi^*$ $C_7 - C_8$, π $C_4 - C_6 \rightarrow \pi^*$ $C_7 - C_8$ and η_2 $O_5 \rightarrow \pi^*$ $C_4 - C_6$ with stabilization energies of 47.03, 43.33, 43.06 and 41.75 kcal/mol. Similar transfers were observed in water in the order of η_2 $O_1 \rightarrow \pi^*$ C_2, π $C_4 - C_6 \rightarrow \pi^*$ $C_7 - C_8$, η_2 $O_9 \rightarrow \pi^*$ $C_7 - C_8$ and η_2 $O_5 \rightarrow \pi^*$ $C_4 - C_6$ with energies of 45.47, 44.48, 43.02 and 42.77 kcal/mol respectively. In the gas phase, daphnetin showed major charge transfers involving η_2 $O_{12} \rightarrow \pi^*$ $C_{11} - O_{13}$, η_2 $O_{13} \rightarrow \pi^*$ $C_{11} - O_{12}$, η_2 $O_{13} \rightarrow \pi^*$ $C_7 - C_8$ and η_2 $O_1 \rightarrow \pi^*$ $C_2 - C_3$ with stabilization energies of 46.37, 44.50, 39.69 and 39.25 kcal/mol. These transfers were also major contributors in water solvation at the order of η_2 $O_{13} \rightarrow \pi^*$ $C_{11} - O_{12}$, η_2 $O_{12} \rightarrow \pi^*$ $C_{11} - O_{13}$, η_2 $O_1 \rightarrow \pi^*$ $C_2 - C_3$ and η_2 $O_{13} \rightarrow \pi^*$ $C_7 - C_8$ with stabilization energies of 50.63, 45.25, 37.32 and 37.07 kcal/mol respectively. In metforminH$^+$, the gas phase major transfers were observed for η_1 $N_3 \rightarrow \pi^*$ $N_1 - C_8$, η_1 $N_4 \rightarrow \pi^*$ $N_2 - C_9$, η_1 $N_5 \rightarrow \pi^*$ $N_2 - C_9$ and σ $N_2 - C_9 \rightarrow \pi^*$ $N_1 - C_8$ with energies 95.45, 92.09, 80.84 and 46.25 kcal/mol respectively. In water a similar trend was observed for η_1 $N_3 \rightarrow \pi^*$ $N_1 - C_8$, η_1 $N_4 \rightarrow \pi^*$ $N_2 - C_9$ and η_1 $N_5 \rightarrow \pi^*$ $N_2 - C_9$ with energies of 97.98, 92.37 and 91.05 kcal/mol. In solvated metforminH$^+$ the fourth highest energy transfer stems from π $N_2 - C_9 \rightarrow \pi^*$ $N_1 - C_8$ with an energy of 45.41 kcal/mol. The extended NBO analysis

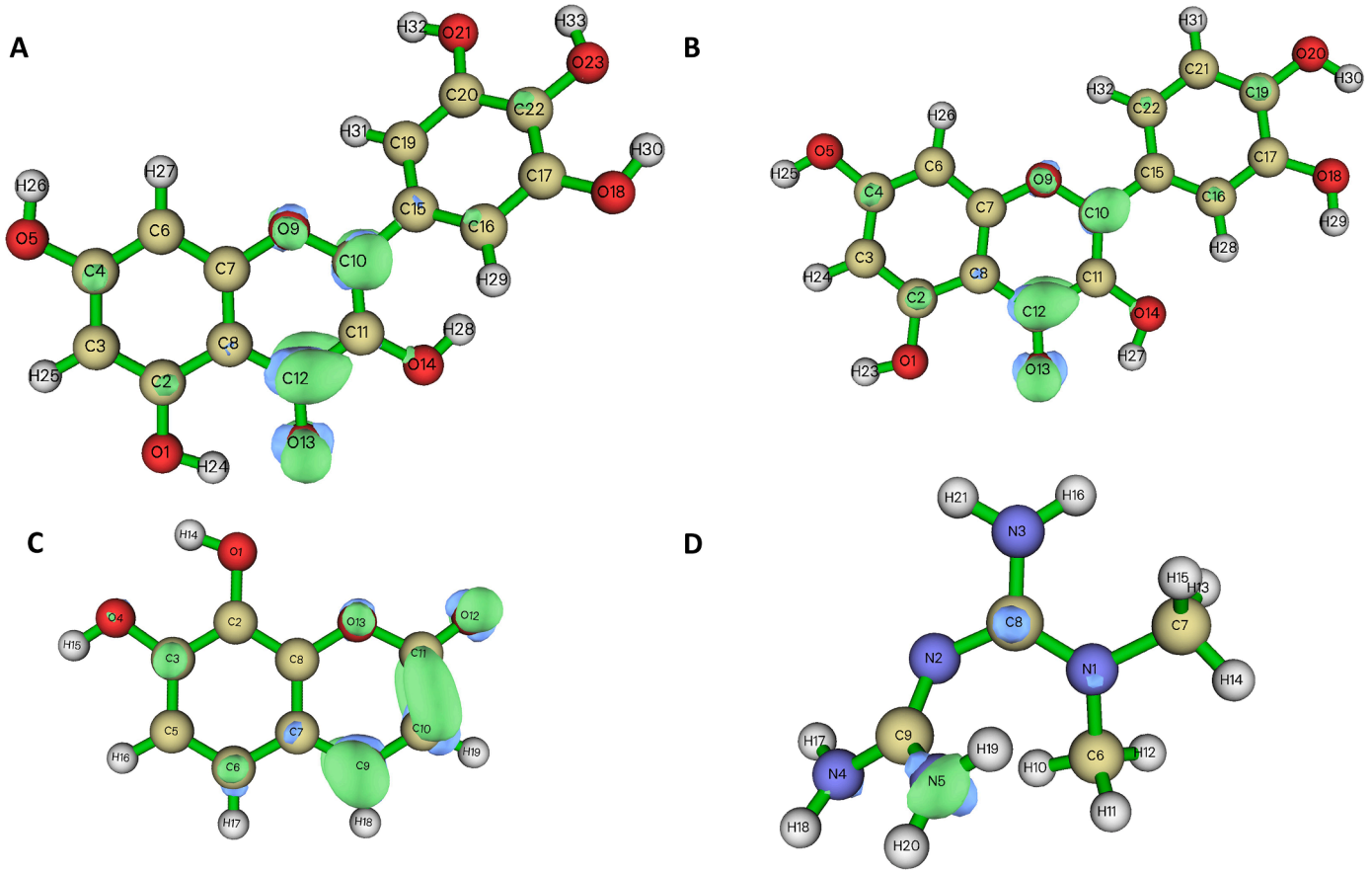


Fig. 15. Positive Fukui functions (f^+) for (A) Myricetin (1, CID 5281672); (B) Quercetin (2, CID 5280343); (C) Daphnetin (3, CID 5280569) and (D) MetforminH$^+$ (6, CID 4091) in PCM water solvent (ε = 78.355) at M06–2X/6–311++G(d,p) level of theory.

under solvation at a threshold of 10 kcal/mol can be found in Tables S6, S9, S12 and S15.

3.3.6. QTAIM and NCI plot analyses

Bader's quantum theory of atoms in molecules (QTAIM) and noncovalent interactions (NCI) [94] have been employed to understand the nature of intramolecular bonding of the phytocompounds [106]. AIM is a tool for investigating interactions in real-space functions such as the total electron density at bond critical points (BCPs). In Bader's method, intra and intermolecular hydrogen bonds can be studied by topological parameters comprising the bond energy $E_{int} = V(r)/2$, the Lagrangian kinetic energy $G(r)$, the potential energy density $V(r)$, electron density $\rho(r)$, Laplacian of electron density $\nabla^2\rho(r)$ and the Hamiltonian kinetic energy $H(r) = G(r) + V(r)$ [79]. The Laplacian $\nabla^2\rho(r)$ and electron density $\rho(r)$ govern the interaction type. The hydrogen bond can fall into three categories: (1) weak hydrogen bond, where $\nabla^2\rho(r) > 0$ and $H(r) > 0$; (2) moderate hydrogen bond, $\nabla^2\rho(r) > 0$ and $H(r) < 0$; and (3) strong hydrogen bond, $\nabla^2\rho(r) < 0$ and $H(r) < 0$. The critical points are depicted in Fig. 18. Here, three possible crucial points can be observed: the ring (RCP), the bond (BCP) and the reaction type (RCP). The positioning of the bond's critical point reveals the polarity of the bonds. BCPs are found near donor atoms in polar bonds and are in the centre of nonpolar bonds. This information yields insights into the possible reaction sites within a molecule and intramolecular stabilizing effects. The topological parameters for intramolecular hydrogen bonds observed in myricetin and quercetin are summarized in Table 8. Non bonded BCPs (34 and 41), and RCPs (38, 44, 51, 58 and 61) are observed for myricetin, while quercetin displayed BCPs (67, 72, and 74) and RCPs (45, 49, 58, 63, 71 and 73). Daphnetin shows resolved RCPs (29 and 31) while only bonded BPCs (σ s-sp, σ sp-sp and π p-p) are observed in MetforminH$^+$. It should be noted however, that the absence of nonbonding interaction in AIM does not rule out its existence.

To further visually investigate the strength of nonbonding interaction NCI is used. NCI is combined with reduced density gradient (RDG) analysis for visualization of molecular interactions. RDG relies on electron density and its derivatives to efficiently distinguish noncovalent interactions such as van der Waals, stearic repulsion and hydrogen bonds. The RDG values are computed according to:

$$\mathrm{RDG(r)} = frac12\left(3\pi^2\right)^{\frac{1}{3}}\frac{|\nabla\rho(\mathrm{r})|}{\rho(\mathrm{r})^{\frac{4}{3}}}$$

Low-density gradient analysis confirms weak interaction sites, while strong interactions are identified at high-density gradient. RDG plots employ low-gradient peak density as an indicator of interaction strength. This analysis distinguishes interaction types as the product of the second eigenvalues (λ_2) and electron density ρ. Bound ($\lambda_2 < 0$) and noncoupling ($\lambda_2 > 0$) interactions can be distinguished according to the parameter sign λ_2. In this analysis, high value densities ($\rho > 0$) with negative λ_2 signifies strong attractive interactions such as hydrogen bonds. Large positive λ_2 at high density ($\rho > 0$) mark the areas of strong repulsive forces such as stearic hinderance. Weak interaction such as the van der Waals are observed at near zero values ($\lambda_2 \approx 0$, $\rho \approx 0$). The NCI and RDG plots of the studied compounds are shown in Figs. 19 and 20.

3.3.7. ELF and LOL analysis

Electron density can be investigated through electron localizing function (ELF) [94], a tool for quantitative analysis of electron behavior. We employed electron localizing function to investigate the intramolecular bonding of the studied compounds. The ELF diagrams of the phytocompounds are shown in Figs. 21 and 22. In the ELF 2D mapping,

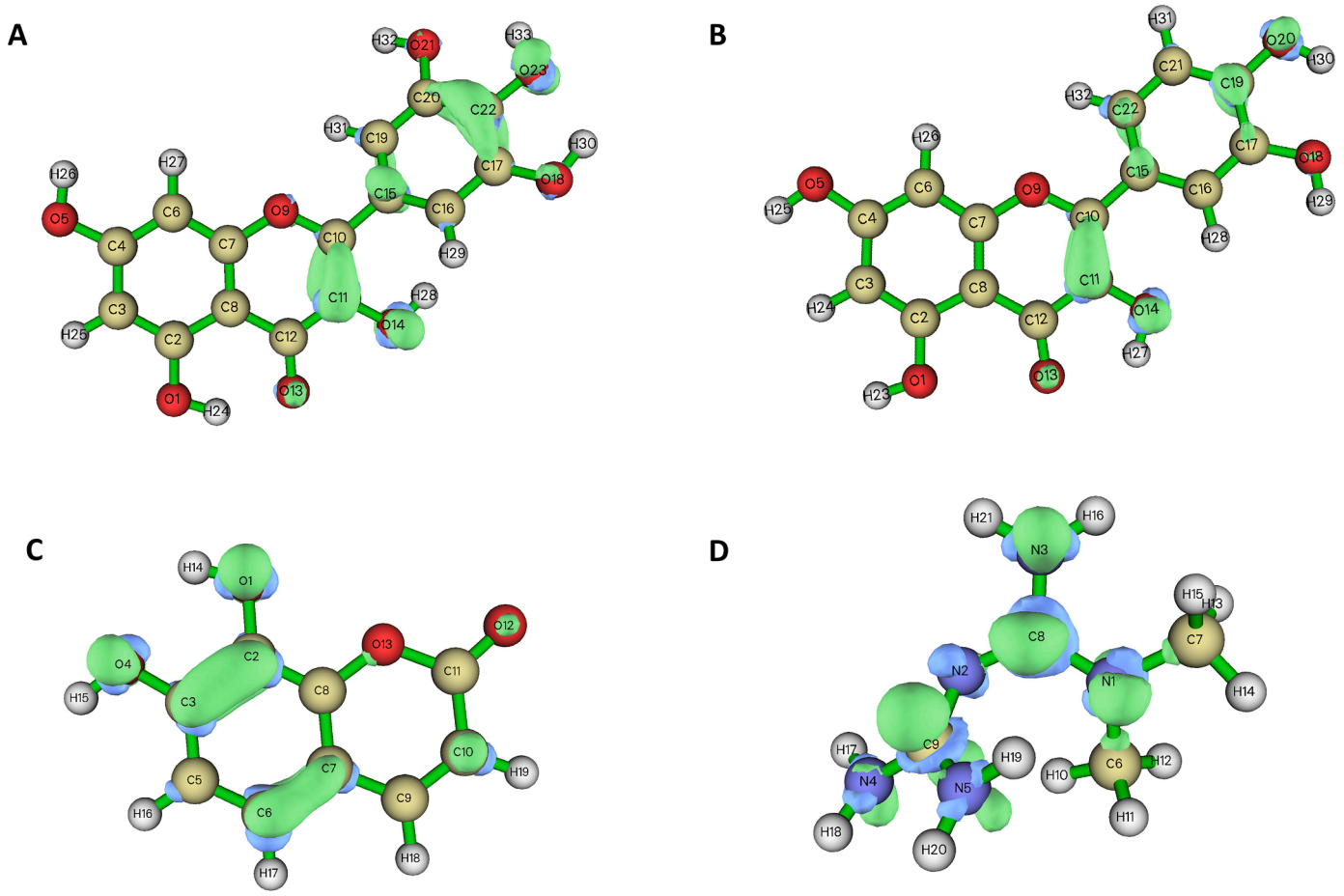


Fig. 16. Negative Fukui functions (f⁻) for (A) Myricetin (1, CID 5281672); (B) Quercetin (2, CID 5280343); (C) Daphnetin (3, CID 5280569) and (D) MetforminH$^+$ (6, CID 4091) at M06–2X/6–311++G(d,p) level of theory in PCM water solvent (ε = 78.355).

electrons are shown as hue relative to electron density. Low electron density ρ(r) ≈ 0 is shown as blue and high electron density ρ(r) = 1.0 as red. Electrons in core orbitals are shown as red circles within cyclic blue areas, this marks nuclei with filled core orbitals and delocalized valence electrons. The blue circles around the red nuclei denote the absence of valence electrons in atomic orbitals. The red hue in between the nuclei indicates the electrons in molecular orbitals. This information can also be read in the accompanying 3D ELF plot as a potential energy surface. In 3D ELF, resolved nuclei are pointy tips within deep wells, the height signifies the high electrostatic potential due to core electron. The well surrounding the pointy tips denote the absence of electrons in valence atomic orbitals hence low electrostatic potential energy. Molecular orbitals are depicted as hilltops denoting the high electrostatic potential.

To further investigate the electronic structure of the phytocompounds the localized orbital locator (LOL) method was employed. Localized orbital locator uses the same electron density mapping as ELF however in the former, electron density can be mapped on the electrostatic energy surface to yield insights on the atomic and molecular orbitals. The localized orbital locator maps are shown in Figs. 21 and 22. In LOL, electron density ranges from ρ(r) = 0 (blue) to ρ(r) = 0.8 (red), while upper ρ(r) > 0.8 and lower ρ(r) < 0 outliers of electron density are shown as white and black regions, respectively. Notably, the valence electrons are delocalized away from the nuclei (blue circles) and are localized in molecular orbitals (red shades). White areas within centralized molecular orbitals found between heavy atoms -CC-, -CO- and/ -CO (σ sp-sp and/ π p-p) denote high electron density (ρ(r) > 0.8) molecular orbitals. However, white spheres near hydrogen in -CH and -OH bonds (σ s-sp) denote the 1s orbital penetration. From this, it can be noted that in polar hydrogen orbitals -OH (σ s-sp) are less penetrated than the nonpolar -CH (σ s-sp), denoting the probable higher reactivity/ acidity of polar and activated hydrogens in the phytocompounds. The full atom numbering for LOL analysis is according to Fig. S12.

3.4. *Drug-likeness and ADMET prediction [81,107]*

Computational drug-likeness studies [81] are important in drug discovery as they eliminate leads with poor pharmacokinetics early in the process. Drug candidates must display optimum activity and least toxicity. We used metforminH$^+$ as a positive control to compare the drug-likeness potentials of *T. officinale* compounds. Absorption, distribution, metabolism, and excretion descriptors were measured in reference to metforminH$^+$ as the most prescribed anti-T2D worldwide [108]. Tables 9 and 10 show the summarized drug metabolism and pharmacokinetic data for the studied phytocompounds. The negatively charged conjugate quinate ion (from quinic acid, CID: 6508) showed the highest soluble hydrogen acceptance of 7.85. The least soluble hydrogen acceptance was observed for the positively charged metforminH$^+$ tautomer. This observation is attributed to these ions' formal charge and ability to attract or repel a proton in solution. Myricetin showed the highest number of hydrogen bonds a solute can accept in water, making it the most nucleophilic phytoconstituent. All the studied compounds showed soluble hydrogen donor-acceptor within the acceptable ranges.

The predicted octanol/water partition coefficient (QPlogPo/w) and polar surface area (PSA) are important limits for the preliminary estimation of biological activity. The QPlogPo/w was in the optimal range for all six compounds. The optimum values accepted for PSA are between 7 and 200. All the calculated PSA values were within this range, and myricetin showed the highest polarity and, hence, the least

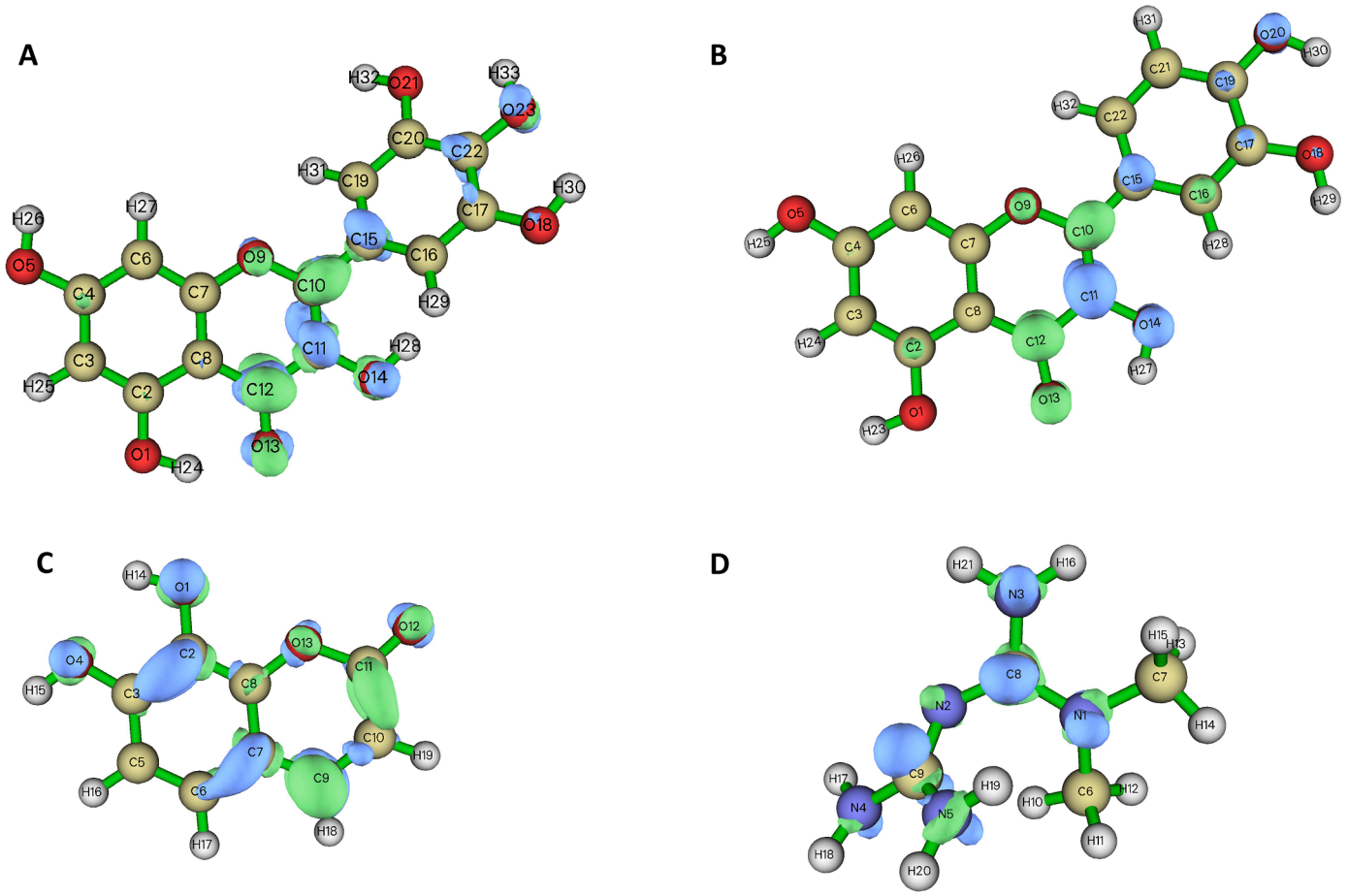


Fig. 17. Electron density dual descriptor functions ($f^{(2)}$) for (A) Myricetin (1, CID 5281672); (B) Quercetin (2, CID 5280343); (C) Daphnetin (3, CID 5280569) and (D) MetforminH$^+$ (6, CID 4091) at M06–2X/6–311++G(d,p) level of theory in PCM water solvent (ε = 78.355).

Table 6
Non-linear optical properties and solvation energies at M06–2X 6–311++*G*(d,p) in PCM.

CID	α (10^{-23} esu)	Δα (10^{-24} esu)	β (10^{-28} esu)	μ_D (Debye)	Solvation energy (kcal/mol)
5281672	4.32	30.3	5.27	12.43	-26.04
5280343	4.36	36.3	1.82	4.905	-25.24
5280569	2.42	21.2	3.06	10.57	-15.81
4091*	1.64	6.00	0.147	2.42	-77.42

* MetforminH$^+$

lipophilicity. Daphnetin displayed the highest percentage of human oral absorption, followed by the metforminH$^+$ tautomer, quercetin, quinic ion, malic ion and myricetin. The acceptable range of predicted binding to human serum albumin (QPlogKhsa) bounds from -1.5 to 1.5. In our system, the QPlogKhsa values were between -1.252 to -0.364. The drug-likeness was estimated according to Lipinski's rule of 5 (Ro5); except for myricetin, all the compounds did not violate the rule.

Myricetin violated one Ro5 as the number of hydroxyls is greater than five. Among all the six compounds, daphnetin and the metforminH$^+$ protomer showed the highest predicted central nervous system activity of -1. The computed IC_{50} for HERG ion channels was above -5 for all the compounds, with daphnetin showing the highest probability for ion channel blocking. The passive diffusion or active transport mechanisms of the apparent Caco-2 cell permeability and the Madin-Darby Canine Kidney (MDCK) cell line were studied. Daphnetin showed the best Caco-2 as well as the highest MDCK value. Caco-2 predicts human intestinal permeability, while MDCK models the blood-brain barrier passage. The skin permeability (log Kp) and aqueous solubility (log S) were within the acceptable ranges, rendering all the compounds permeable through the skin and soluble in water. Except for daphnetin, which had a calculated number of reactive functional groups (#rtvFG) of one, all the studied had zero #rtvFG. The value of rtvFG predicts the steps a molecule will take to reach the target site after entering the bloodstream. All the molecules were predicted to undergo metabolic reactions within the acceptable range (1 - 8).

3.5. MD

The stability and flexibility of the macromolecular scaffolds was studied through molecular dynamics (MD) simulations. The simulations of the four complex systems were studied in environments simulating physiological conditions (pH = 7.4, C_{NaCl} = 0.15 M).

3.5.1. RMSD

The root mean square displacement (RSMD) calculation of the backbone atoms was used to assess the structural and dynamic properties of the protein-ligand complexes. The dynamics were carried out for 100 ns simulation time. RMSD measures the mean distance between the backbone atoms of the complex according to:

$$RMSD_X = \sqrt{\frac{1}{N}\sum_{i=1}^{N}(\delta)^2}$$

where *N* is the sum of atoms calculated, and δ represents the distance of

Table 7
NBO analysis of phytocompounds at M06-2X/6–311++*G*(d,p).

$CID_{(phase)}$	Donor(i)	ED(i)	Acceptor(j)	ED(j)	E^2 (kcal/mol)	E_j-E_i (a.u.)	F(i,j) (a.u.)
$5281672_{(g)}$	η_2 (O_1)	1.8300	π* C_2-C_3	0.3422	51.68	0.44	0.134
	π C_4-C_6	1.6860	π* C_7-C_8	0.4581	44.07	0.35	0.110
	η_2 (O_5)	1.9755	π* C_4-C_6	0.4068	43.35	0.45	0.125
	π C_2-C_3	1.676	π* C_4-C_6	0.4068	43.30	0.34	0.109
$5281672_{(w)}$	η_2 (O_1)	1.8446	π* C_2-C_3	0.3374	48.12	0.44	0.130
	π C_4-C_6	1.6756	π* C_7-C_8	0.4636	44.71	0.34	0.110
	η_2 (O_5)	1.8673	π* C_4-C_6	0.3882	44.01	0.45	0.126
	η_2 (O_9)	1.7636	π* C_7-C_8	0.4636	41.79	0.45	0.123
$5280343_{(g)}$	η_2 (O_1)	1.8588	π* C_2-C_3	0.3626	47.03	0.44	0.129
	η_2 (O_9)	1.7749	π* C_7-C_8	0.4493	43.33	0.45	0.125
	π C_4-C_6	1.6790	π* C_7-C_8	0.4493	43.06	0.35	0.109
	η_2 (O_5)	1.8727	π* C_4-C_6	0.3725	41.75	0.46	0.124
$5280343_{(w)}$	η_2 (O_1)	1.8606	π* C_2-C_3	0.3469	45.47	0.45	0.128
	π C_4-C_6	1.6711	π* C_7-C_8	0.4605	44.48	0.34	0.110
	η_2 (O_9)	1.7728	π* C_7-C_8	0.4605	43.02	0.45	0.124
	η_2 (O_5)	1.8678	π* C_4-C_6	0.3761	42.77	0.45	0.124
$5280569_{(g)}$	η_2 (O_{12})	1.8428	σ* C_{11}-O_{13}	0.1141	46.37	0.72	0.163
	η_2 (O_{13})	1.7580	π* C_{11}-O_{12}	0.2453	44.50	0.47	0.129
	η_2 (O_{13})	1.7580	π* C_7-C_8	0.4550	39.69	0.44	0.118
	η_2 (O_1)	1.8795	π* C_2-C_3	0.4123	39.25	0.44	0.117
$5280569_{(w)}$	η_2 (O_{13})	1.7556	π* C_{11}-O_{12}	0.2892	50.63	0.45	0.092
	η_2 (O_{12})	1.8564	σ* C_{11}-O_{13}	0.1081	45.25	0.74	0.083
	η_2 (O_1)	1.8860	π* C_2-C_3	0.4172	37.32	0.44	0.098
	η_2 (O_{13})	1.7556	π* C_7-C_8	0.4684	37.07	0.45	0.084
$4091_{(g)}$	η_1 (N_3)	1.7249	π* N_1-C_8	0.5020	95.45	0.31	0.155
	η_1 (N_4)	1.7357	π* N_2-C_9	0.4782	92.09	0.34	0.158
	η_1 (N_5)	1.7648	π* N_2-C_9	0.4782	80.84	0.36	0.151
	σ N_2-C_9	1.8305	π* N_1-C_8	0.5020	46.25	0.36	0.115
$4091_{(w)}$	η_1 (N_3)	1.7184	π* N1-C_8	0.4976	97.98	0.31	0.156
	η_1 (N_4)	1.7400	π* N_2-C_9	0.4921	92.37	0.34	0.157
	η_1 (N_5)	1.7433	π* N_2-C_9	0.4921	91.05	0.34	0.157
	π N_2-C_9	1.8326	π* N_1-C_8	0.4976	45.41	0.36	0.114

pairs of common atoms. The four systems were stable and showed convergence around 40ns. Myricetin showed the lowest RMSD throughout the simulation, with pre-convergence average RMSD (0 – 40 ns) and equilibrium RMSD (>40 ns) of 2.356 and 2.321 Å. The protein RMSD fluctuations are shown in Fig. 23A. Generally, protein systems with larger ligands (JNK1_myricetin and JNK1_quercetin) displayed reduced complex RMSD of 2.34 and 2.87 Å, respectively. Correspondingly, smaller ligand-containing complexes recorded the highest values of protein RMSD of 3.02 and 2.88 Å for JNK1_daphnetin and JNK1_metforminH$^+$. This observation suggests that larger ligands bring the protein to a near-crystal state due to their extended reach within the binding pocket. The ligand RMSDs were computed and plotted in Fig. 23B to investigate this further. It was observed that smaller ligands exhibited the highest values of RMSD compared to sized ligands. Larger ligands (myricetin and quercetin) showed the lowest average RMSDs of 3.04 and 2.79 Å. Daphnetin and metforminH$^+$ recorded higher values of 3.54 and 8.11 Å. It was further noted that there were two defined equilibrium states for daphnetin RMSD (S1 and S2), while metforminH$^+$ showed the most volatile moving average. The average RMSD of the first equilibrium state of daphnetin (S1) was 2.66 Å and extended from 0 – 40, 77 – 88 and 94 – 100 ns. An RMSD of 4.93 Å was obtained for the second state (S2), which was measured between intervals of 44 – 76 and 89 – 93 ns, Fig. 23B. The size of the compounds was deduced to be the most determining factor of the ligand mobility within the protein. Smaller ligands (daphnetin and metforminH$^+$) recorded higher flexibilities than larger phytocompounds (quercetin and myricetin).

3.5.2. RMSF

Root mean square fluctuations (RMSF) equate the flexibility of the ligand-protein complexes as a function of each standard residue. RMSF is a useful feature for the characterization of the local dynamics within the protein according to:

$$RMSF_i = \sqrt{\frac{1}{T}\sum_{t=1}^{N}\left\langle \left(r_i'(t) - r_i\left(t_{ref}\right)\right)^2\right\rangle}$$

where the trajectory over time is given by *T,* and t_{ref} is the starting time. The positions of the residues and atoms in residue *i* after mapping on the reference are given by r_i and r_i', respectively. RMSF was used to estimate the thermodynamic stabilities of the different systems. Larger RMSF values indicate regions of higher flexibility, while lower values indicate stable or constrained regions. As shown in Fig. 23C, the apo-protein showed the highest fluctuation range at the flexible regions (0.447 – 9.867 Å) compared to all holo-proteins. Fig. 24 shows how the ligand contacts and structured protein regions relate to the RMSF. It was noted that the secondary structures (α helices and β strands) and regions of ligand contact remained rigid during simulation time relative to the unstructured fragments. The β turn residues Ala17, Met181, His186, Ser329, and Lys340 in all the systems showed the highest flexibilities. Moreover, the C-terminal residues from Thr369 also showed the highest RMSF. There was a good agreement between the experimental Debye-Waller temperature factors (B-factor) and RMSF. B-factors mapped on RMSF have been used to estimate the flexible regions of a protein [109]. Bornot *et al.* reported a Pearson correlation 0.29 for raw RMSF and B-factor [110]. The calculated RMSF and B-factor Pearson's correlations for apoprotein were 0.23, 0.29, 0.33, 0.48 and 0.56 for myricetin, quercetin, daphnetin and metforminH$^+$ bound JNK1 systems, respectively. B-factors are obtained from X-ray diffractions and assume isotropic harmonic probability distribution of motions while MD considers the anharmonicity and anisotropic nature of atoms [111]. This difference in considerations of atom motions, X-ray refinement and resolution accounts for the differences in B-factors and RMSF of the flexible regions [112].

3.5.3. Protein interactions

To further understand and refine the binding nature of ligand-protein

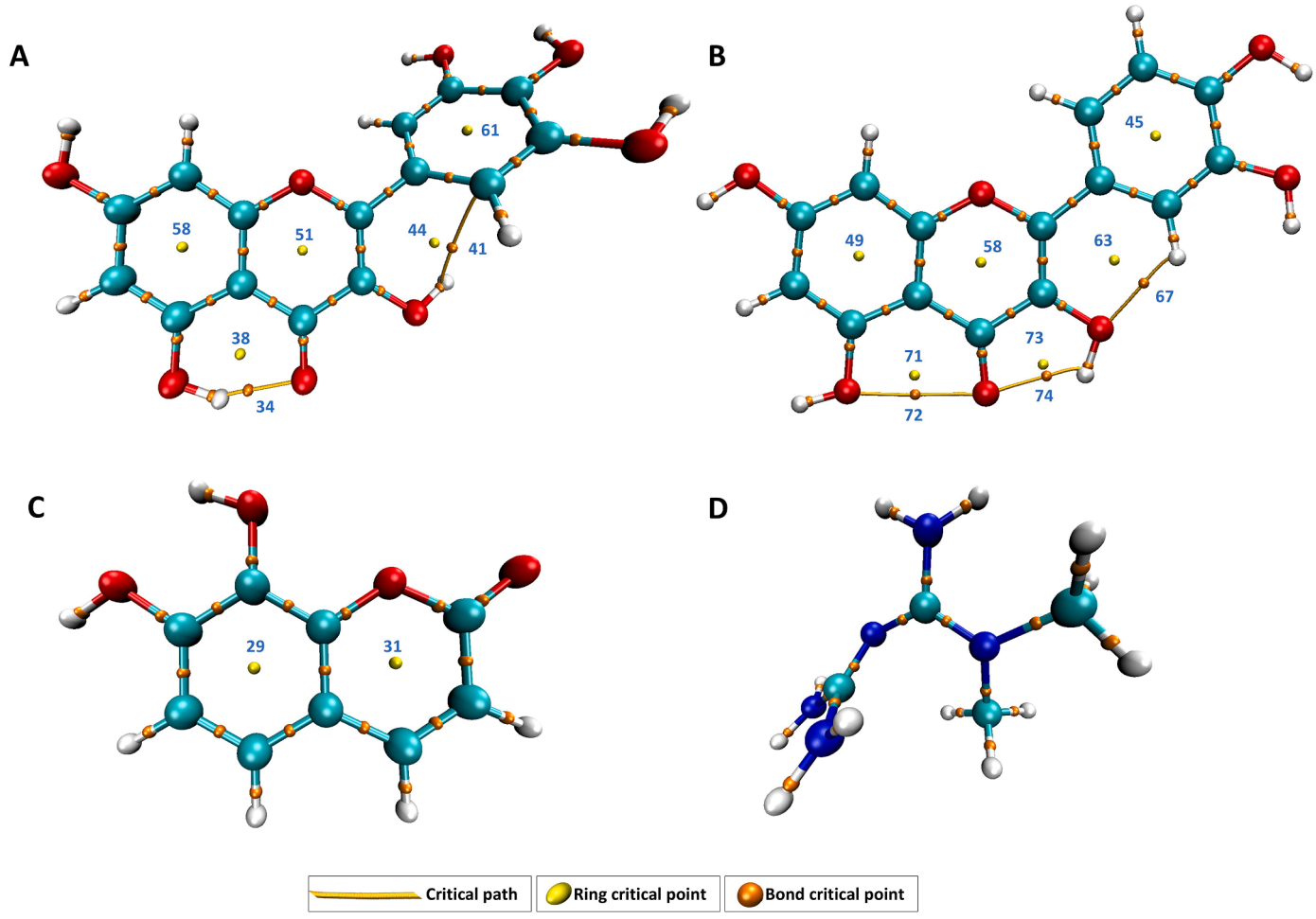


Fig. 18. Bond critical points in (A) Myricetin (1, CID 5281672); (B) Quercetin (2, CID 5280343); (C) Daphnetin (3, CID 5280569) and (D) MetforminH$^+$ (6, CID 4091) at M06–2X/6–311++G(d,p) level of theory in PCM water solvent (ε = 78.355).

Table 8
Hydrogen bond topological properties, Laplacian density ($\nabla^2\rho$ in a.u.) and charge density (ρ in a.u.).

CID	BCP #	BCP	*G(r)*	*V(r)*	*H(r)*	$\nabla^2\rho(r)$	$\rho(r)$	E_{HB}(kcal/mol)
5281672	34	O_1-H_{24}…O_{13}	0.0381	-0.0416	-0.00352	0.138	0.0429	-13.058
5280343	74	O_{14}-H_{27}…O_{13}	0.0261	-0.0237	0.00232	0.114	0.0272	-7.445

interactions we analyzed the trajectories for protein interactions through the simulation period Fig. 25. The myricetin JNK1 complex showed four types of interactions in the order of water bridges > hydrogen bonds > hydrophobic interactions and ionic bonding. Residues Ile32, Gln37 and Ser155 exhibited all four types of interactions with myricetin, while Ser155 revealed all but hydrophobic interactions. Residues Met111, Asn114, Asn156 and Asp169 displayed hydrogen bonding and water bridges with myricetin. Amino acids Lys55 and Glu109 showed only water bridges, and hydrophobic interactions occurred between myricetin and Val40, Ala53, Leu110, Val158 and Leu168.

Quercetin-JNK1 complex demonstrated four types of interactions in the order of water bridges > hydrogen bonds > hydrophobic interactions and ionic bonding. Residues Ile32 showed water bridges, hydrogen bonds and hydrophobic interactions. Amino acids Ser34, Met111 and Asn114 presented water bridges and hydrogen bonds, while Lys55 showed water bridges, hydrogen bonds and ionic bonding. Pure water bridges were observed for residues Glu73 and Glu109, while Val40, Leu110, Val158 and Asp169 demonstrated hydrophobic interactions.

Daphnetin did not show any ionic bonding; the bonding order was water bridges > hydrogen bonds > hydrophobic interactions. Residues Met111 and Asn114 showed a combination of hydrogen bonding and water bridges. Gly33 showed pure hydrogen bonding, while Ile32 showed a combination of water bridges and hydrophobic interactions. Hydrophobic interactions were observed with residues Val40, Ala53, Leu110, Val158 and Leu168. MetforminH$^+$ showed the most varied interactions as it showed the highest mobility through the protein. The order of MetforminH$^+$ binding was water bridges > hydrogen bonds > hydrophobic interactions and ionic bonding.

3.5.4. *Ligand interactions*

The ligand contact summary was analyzed to gain insights into the ligand atoms with the highest contact time during the simulation. Fig. 26 shows how the interactions lasted throughout the simulation. Myricetin showed the longest duration of hydrophilic interactions with residue Met111 for 82 % of the simulation time. This was followed by Asn114 for 40 % and Ile32, Asp169 with maximum contact above 30 %. Quercetin was bound to Met111 and Glu109 for 83 and 75 % of the simulation time, respectively. Residues Gly38, Lys55, Ile32 and Asn114 also

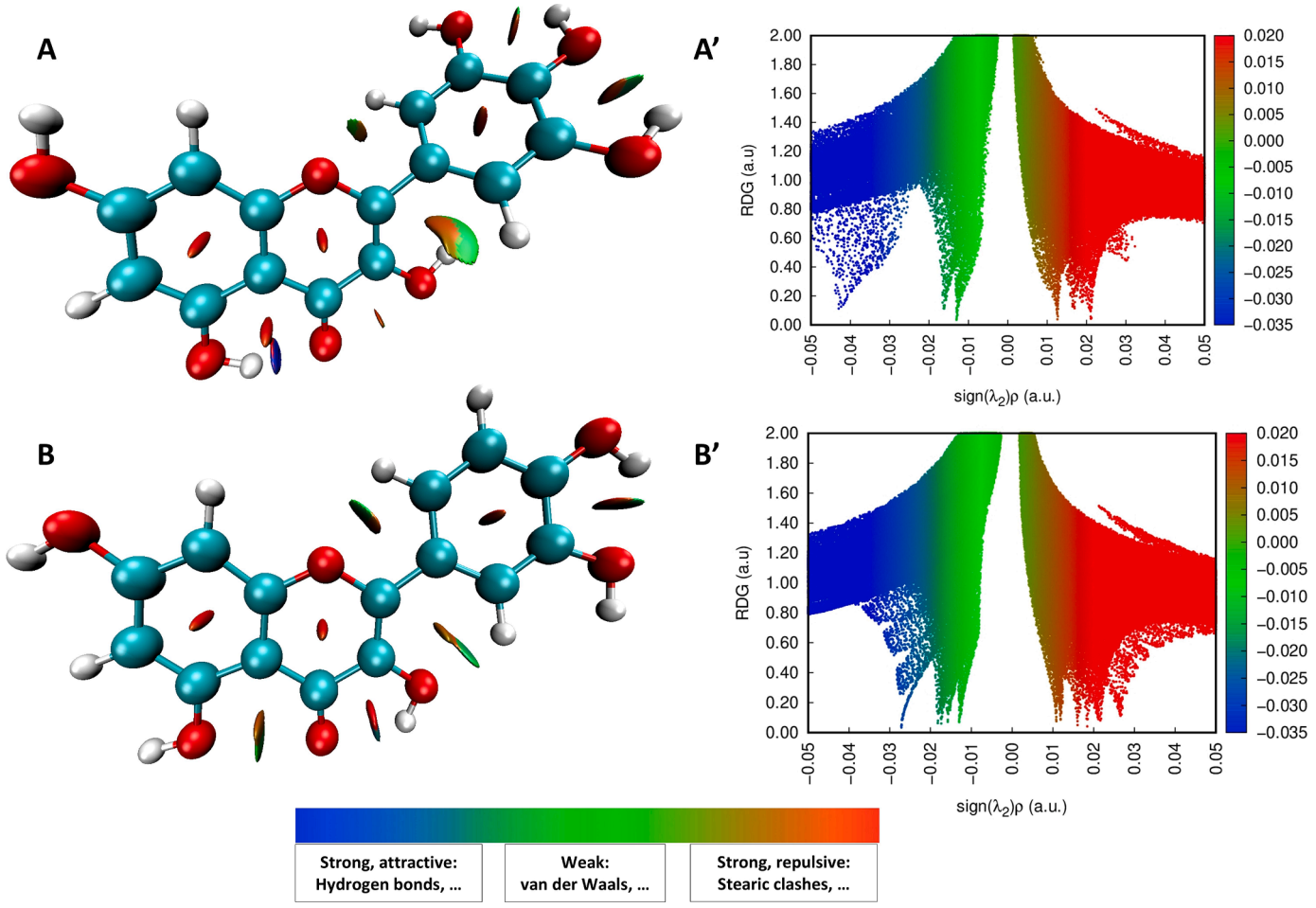


Fig. 19. NCI and RDG plots of (A) Myricetin (1, CID 5281672) and (B) Quercetin (2, CID 5280343) at M06–2X/6–311++*G*(d,p) in PCM water solvent (ε = 78.355).

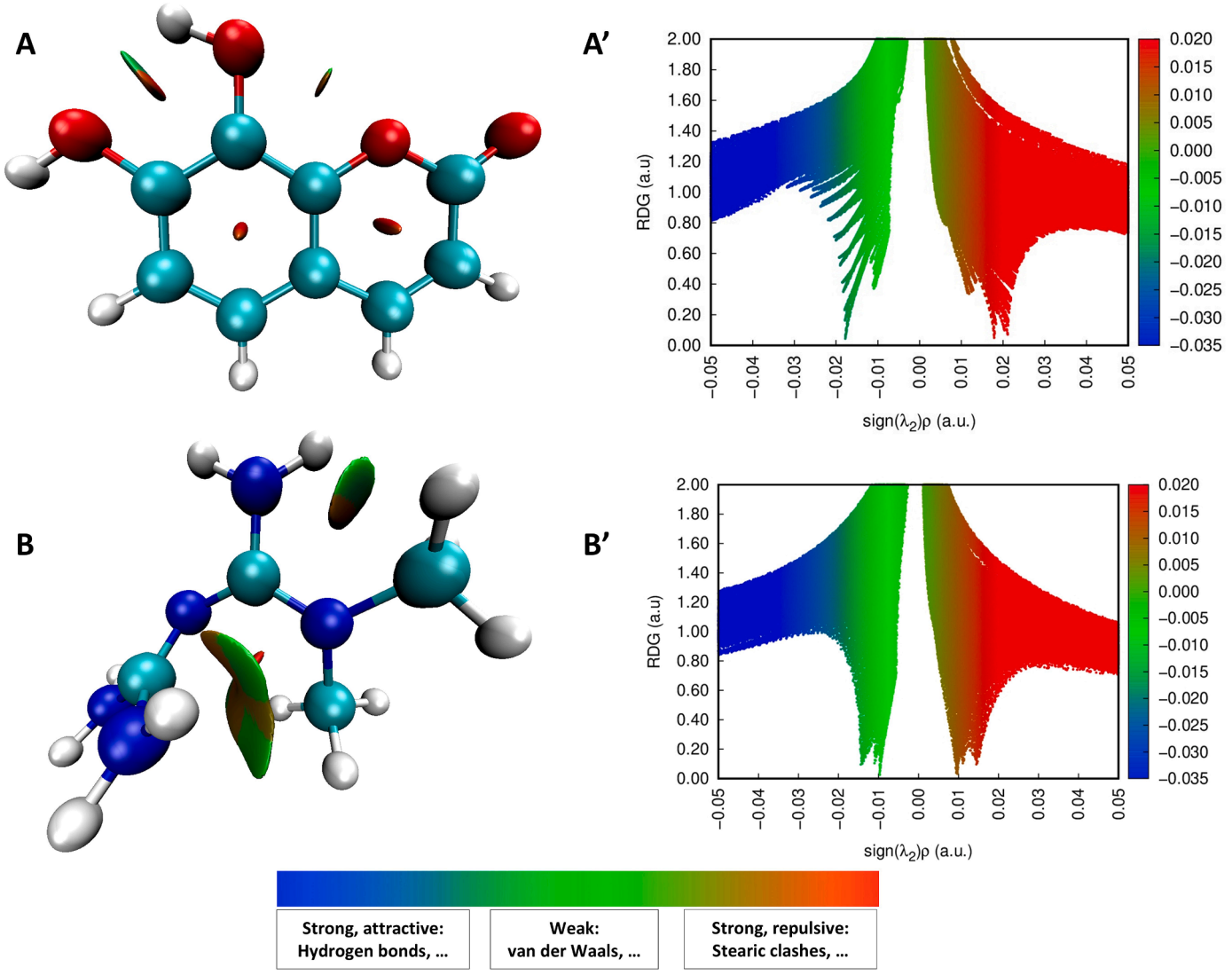


Fig. 20. NCI and RDG plots of (A) Daphnetin (3, CID 5280569) and (B) MetforminH^{+} (6, CID 4091) at M06–2X/6–311++*G*(d,p) in PCM water solvent (ε = 78.355).

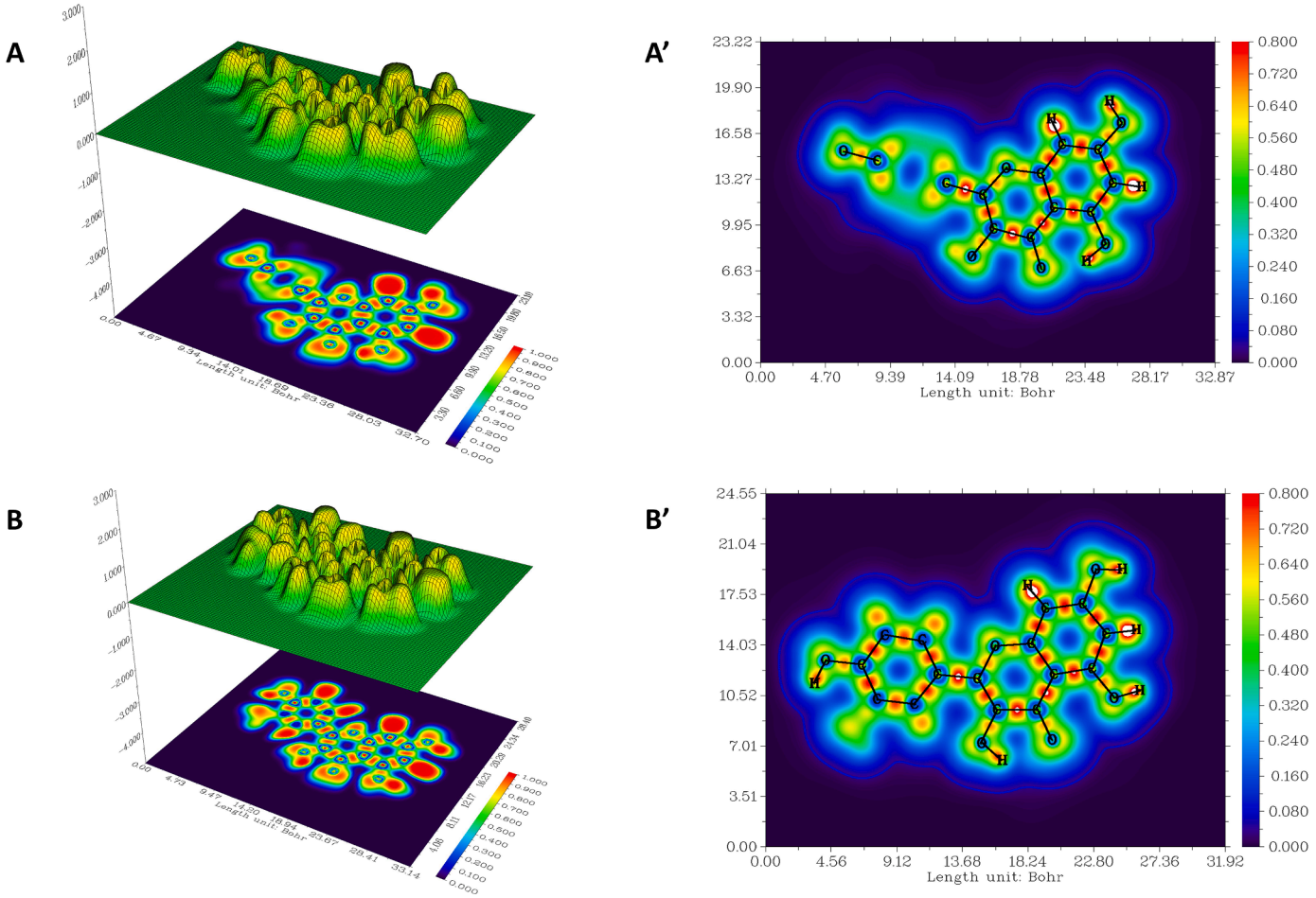


Fig. 21. ELF and LOL of (A) Myricetin (1, CID 5281672) and (B) Quercetin (2, CID 5280343) at M06–2X/6–311++*G*(d,p) in PCM water solvent (ε = 78.355).

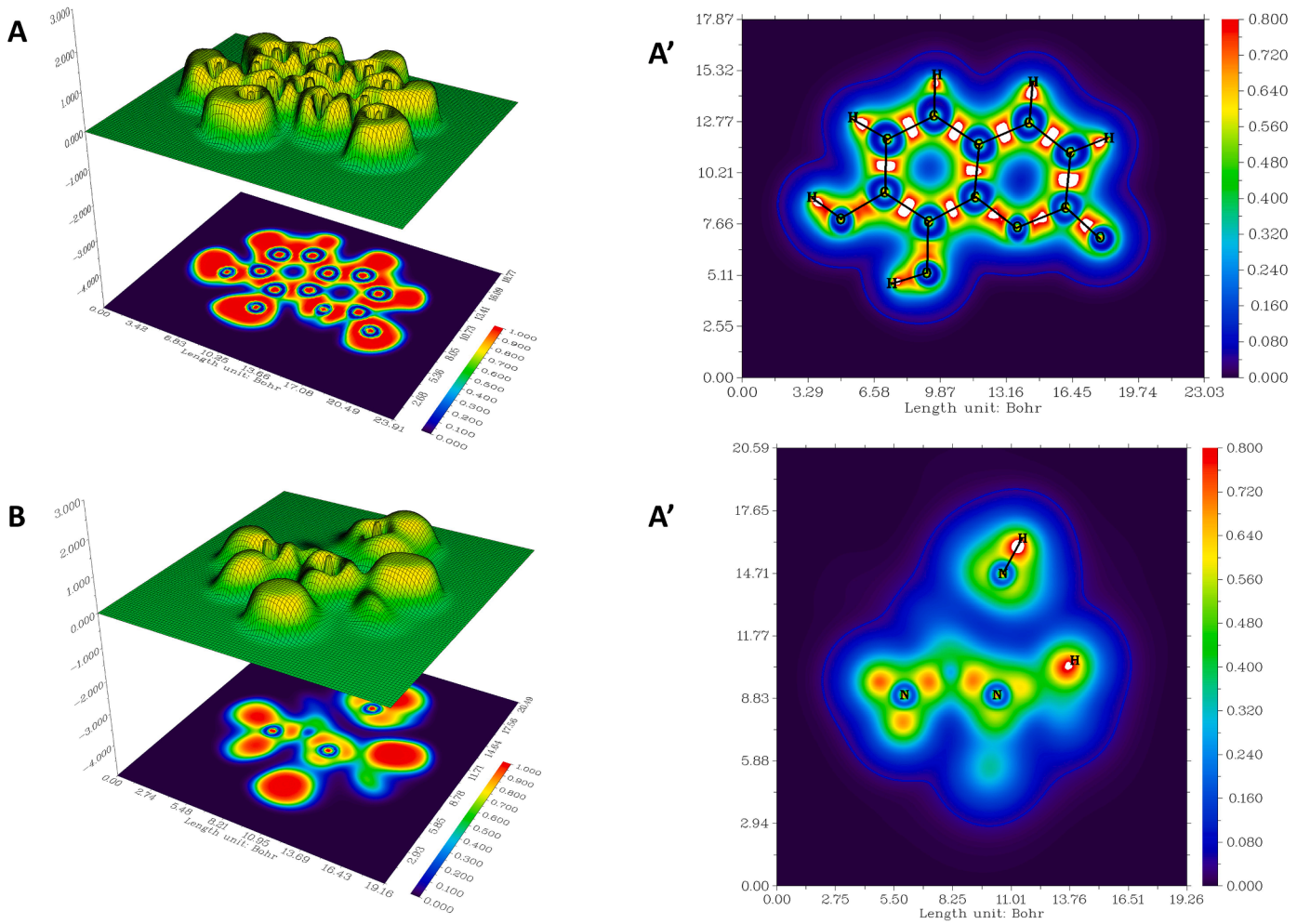


Fig. 22. ELF and LOL of (A) Daphnetin (3, CID 5280569) and (B) MetforminH$^+$ (6, CID 4091) at M06–2X/6–311++*G*(d,p) in PCM water solvent (ε = 78.355).

Table 9
ADMET properties of selected best binding ligands.

CID	Hydrogen Bond Donor[a]	Hydrogen Bond Acceptor[b]	QPlogPo/w[c]	PSA[d]	Percent Human Oral Absorption[e]	QPlogKhsa[f]	Rule of Five[g]
5281672	5	6	-0.279	163.527	27.575	-0.489	1
5280343	4	5.25	0.35	136.815	53.465	-0.364	0
5280569	2	4	0.145	83.801	70.366	-0.59	0
6508	5	7.85	-1.234	127.272	39.183	-0.986	0
525	2	4.7	-0.452	117.401	33.695	-1.252	0
4091*	5	3.5	-0.678	90.865	66.324	-0.917	0

* MetforminH$^+$
[a] Estimated hydrogen bonds solute can donate to water in solution, range [0.0 – 6.0]
[b] Estimated hydrogen bonds a solute can accept from water in a solution, accepted values [2.0 – 20.0]
[c] Predicted octanol/water partition coefficient. [-2.0 – 6.5]
[d] The van der Waals surface area of polar nitrogen and oxygen atoms, [7.0 – 200.0]
[e] Predicted human oral absorption, [0 to 100]
[f] Prediction of binding to human serum albumin, [-1.5 – 1.5]
[g] Number of violations of Lipinski's rule of five, [maximum of 4]

Table 10
Further ADMET properties of selected best binding ligands.

CID	CNS activity [a]	HERG blockage (log IC_{50})[b]	Apparent Caco-2 permeability (nm/s) [c]	Apparent MDCK permeability (nm/s) [d]	Skin permeability (log *Kp*) [e]	Aqueous solubility (log S) [f]	Number of reactive functional groups [g]	Number of likely metabolic reactions [h]
5281672	-2	-4.970	7.088	2.350	-6.365	-4.011	0	6
5280343	-2	-4.760	23.293	8.502	-5.362	-4.043	0	5
5280569	-1	-3.657	239.064	105.341	-3.817	-1.967	1	2
6508	-2	-0.705	12.227	5.388	-5.533	-0.695	0	4
525	-2	1.12	3.351	1.691	-5.563	-0.545	0	2
4091*	-1	-2.853	264.126	117.327	-6.221	-0.649	0	3

* $MetforminH^+$
[a] Calculated central nervous system activity, range [-2 (inactive) to +2 (active)]
[b] Computed IC_{50} value for HERG K^+ ion channels, concerning below -5
[c] Predicted apparent Caco-2 cell permeability [<25 poor, >500 great]
[d] Madin-Darby Canine Kidney (MDCK) cell line models the blood-brain barrier (<25 poor; >500 great)
[e] Calculated skin permeability, range [-8.0 to -1.0]
[f] Predicted aqueous solubility in mol dm^{-3} [-6.5 to 0.5]
[g] Number of reactive functional groups ranges from 0 to 2
[h] Number of likely metabolic reactions, varies between 1 and 8 for 95 % of known drugs

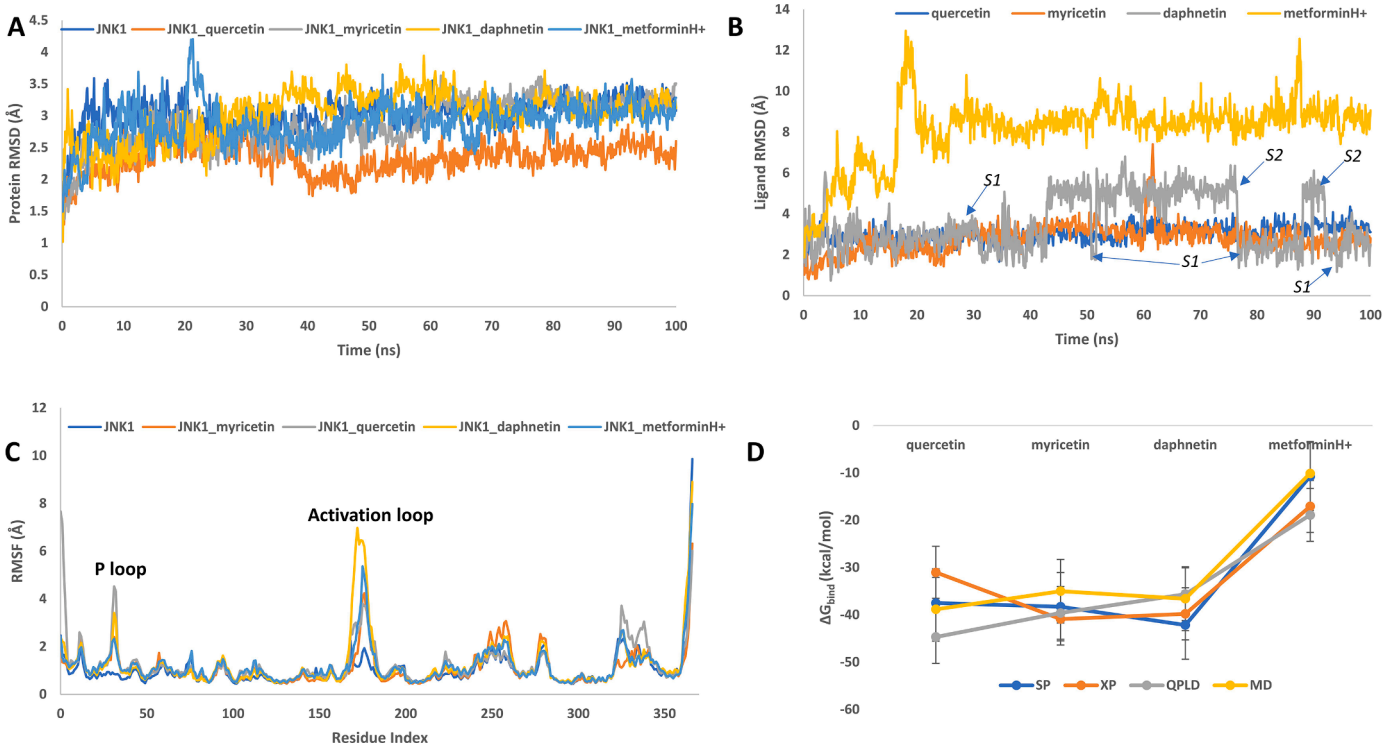


Fig. 23. (A)Protein RMSD, (B) Ligand RMSD, (C) Protein RMSF and (D) MMGBSA energies for selected complexes of T. officinale extracts against 4L7F.

showed stable interactions between 18 – 27 % for quercetin-bound JNK1. Daphnetin showed two binding patterns during the simulation with Met111. The donor hydrogen bond lasted 82 %, and the acceptor lasted 42 % of the simulation. The donor-only bonding results in higher RMSF and corresponds to S2 (Fig. 23B), while the coexistence of both bonds yields lower RMSF and agrees with S1. $MetforminH^+$ was not held in the JNK1 interface and was seen to percolate the entire protein (Fig. 27). This was due to the hydrophobicity of the pocket, the net charge of +1 (Fig. 2B and Fig. 2C), and the fact that $metforminH^+$ is delivered through ion channels.

3.6. MMGBSA

The stability of the complexes during the MD simulation was investigated through the computation of MMGBSA (ΔG_{bind}). [113,114] The "thermal_MMGBSA.py" decomposed ΔG_{bind} for MD is shown in Table 11. From the MD results it can be noted that quercetin showed the lowest binding energy (-38.8 kcal/mol), followed by daphnetin (-36.58 kcal/mol) and myricetin (-34.99 kcal/mol). The binding energy shows that the contributions due to van der Waals energy were higher for quercetin and daphnetin. The van der Waals energy is related to the dipole moment of the hydrophobic residues. This shows that the hydrophobic interactions may be crucial in the binding. Quercetin also showed the highest electrostatic and hydrogen bonding energy contributions which links these energies to stable binding within the binding site. These results agree well with the docking estimated energies for the different systems as shown in Fig. 23D.

The "breakdown_MMGBSA_by_residue.py" script was also employed to analyse free energy decomposition per residue. This analysis yields insights into the nature of protein-ligand contacts within the complex.

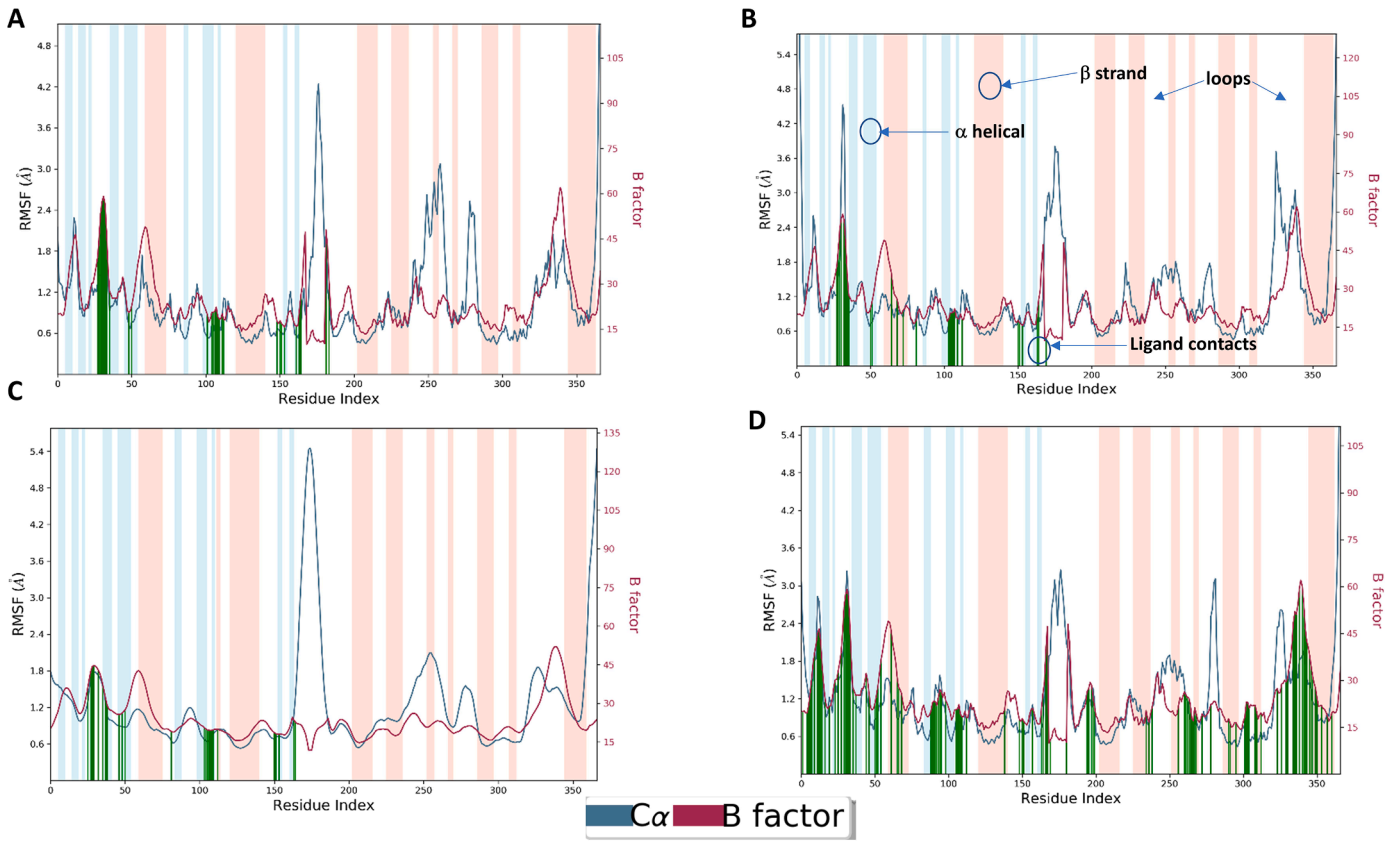


Fig. 24. RMSF and per atom data for (A) Myricetin (1, CID 5281672); (B) Quercetin (2, CID 5280343); (C) Daphnetin (3, CID 5280569) and (D) MetforminH$^+$ (6, CID 4091).

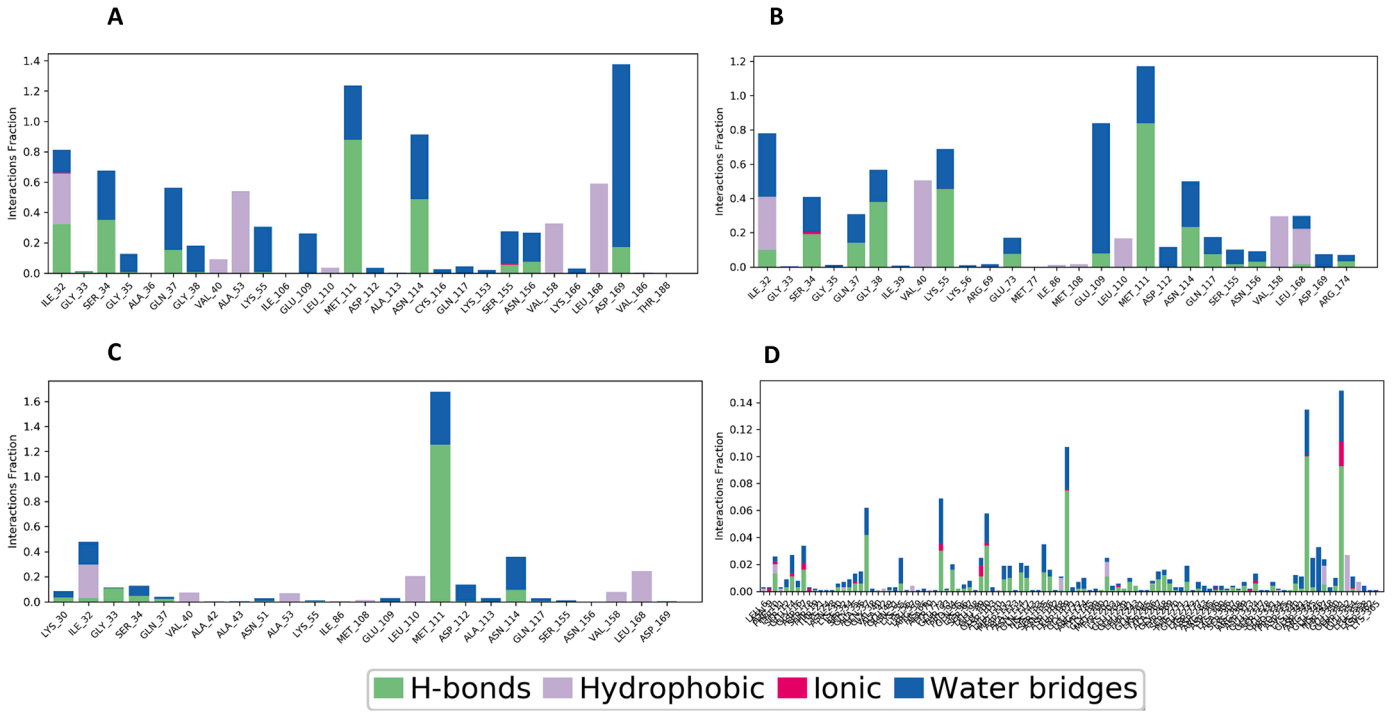


Fig. 25. Per residue interactions in (A) Myricetin (1, CID 5281672); (B) Quercetin (2, CID 5280343); (C) Daphnetin (3, CID 5280569) and (D) MetforminH$^+$ (6, CID 4091).

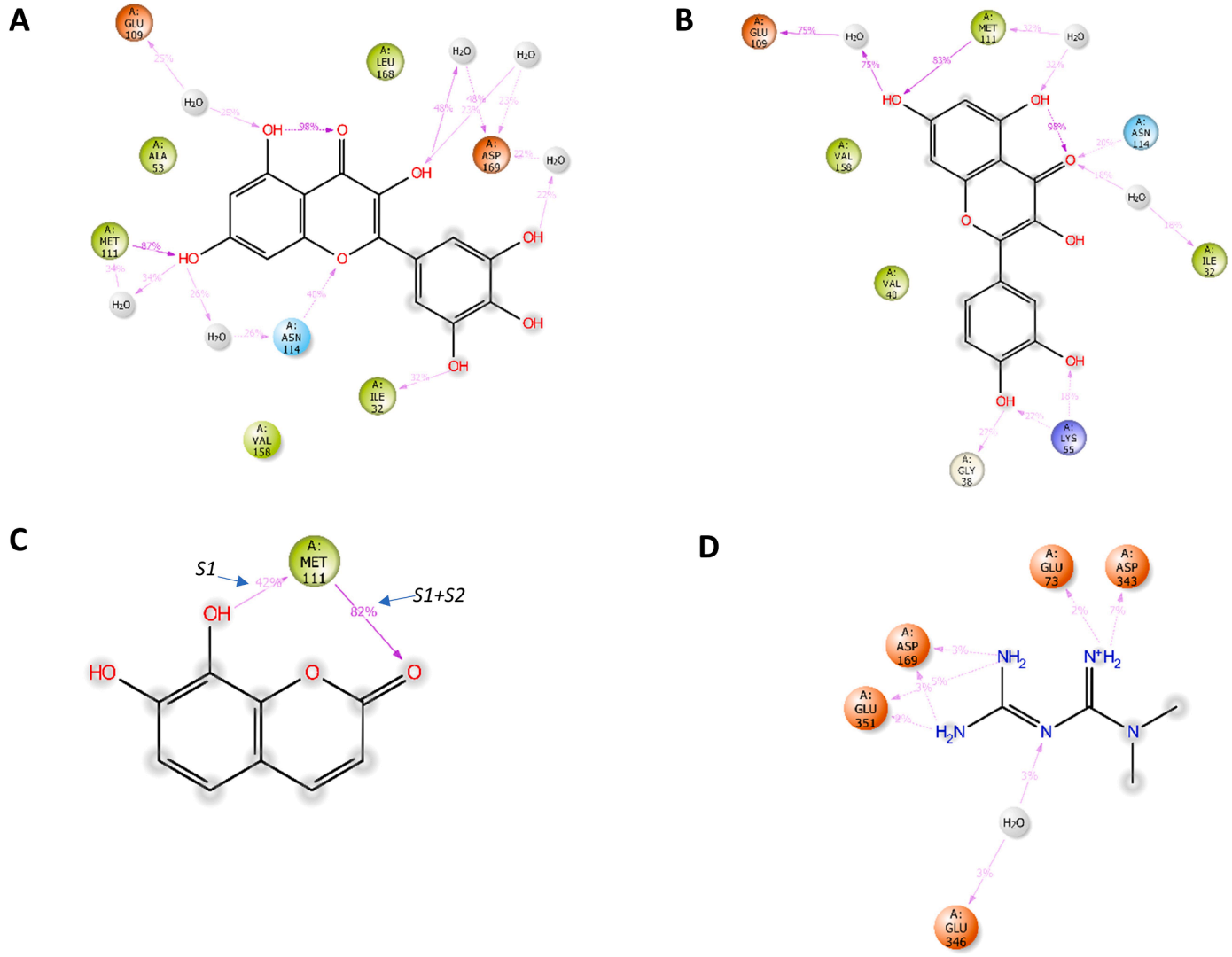


Fig. 26. Molecular interactions during MD for (A) Myricetin (1, CID 5281672); (B) Quercetin (2, CID 5280343); (C) Daphnetin (3, CID 5280569) and (D) MetforminH^{+} (6, CID 4091).

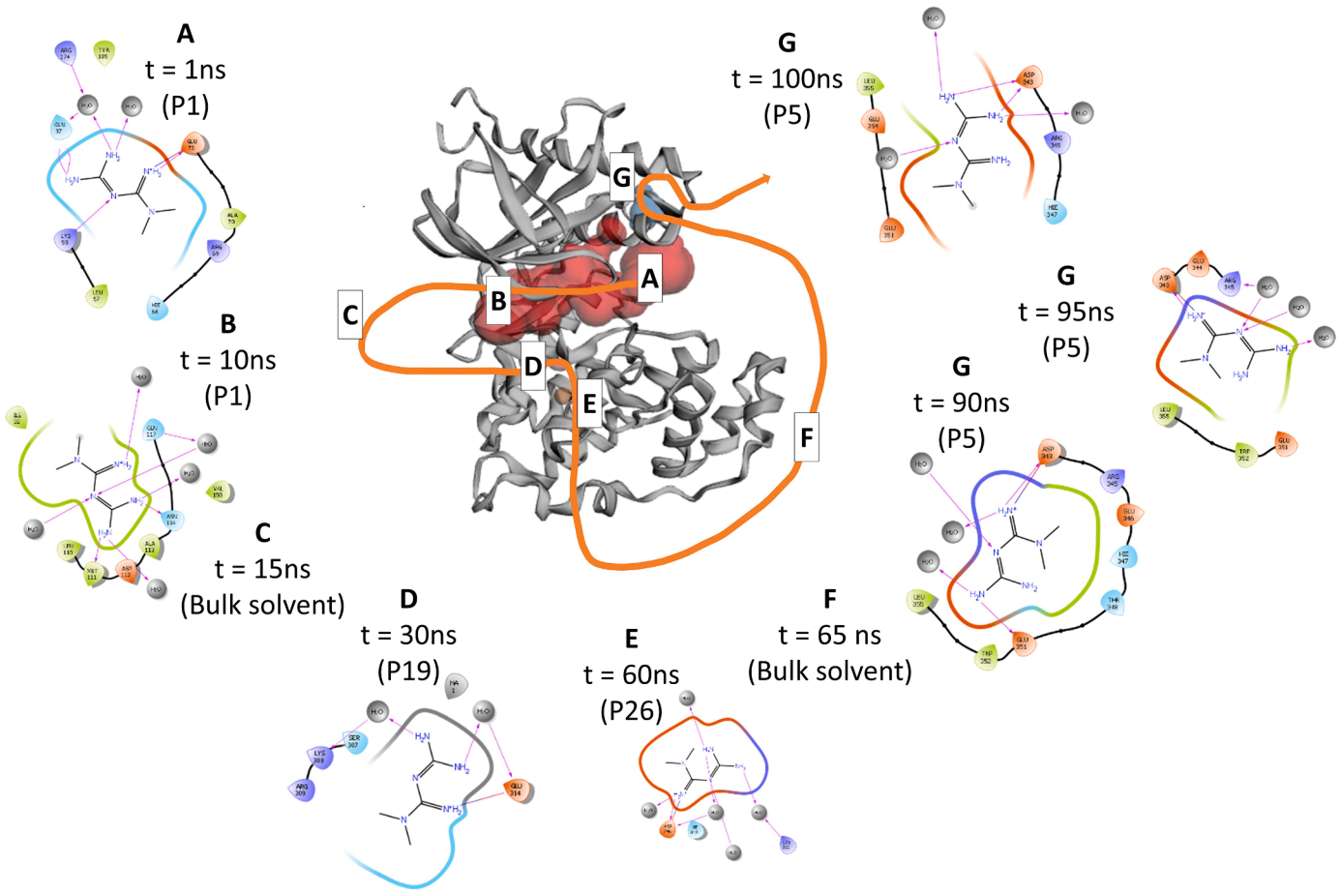


Fig. 27. MetforminH$^+$ migration during MD.

Table 11
Computed MMGBSA energies for the JNK1 system during MD.

CID	Binding free energy(kcal/mol) (MMGBSA)						
	ΔG_{Bind}	$\Delta G_{Coulomb}$	$\Delta G_{Covalent}$	ΔG_{Hbond}	ΔG_{Lipo}	ΔG_{SolvGB}	ΔG_{vdW}
5281672	-38.81	-18.44	1.672	-2.395	-6.636	24.47	-33.64
5280343	-34.99	-13.45	0.750	-1.512	-5.518	19.34	-32.97
5280569	-36.58	-13.04	0.4574	-1.185	-10.08	10.10	-23.24
4091*	-10.09	-24.12	0.463	-1.390	-1.207	18.90	-8.530

For phytocompounds, a snapshot was extracted every 50 ps from the last 40 ns of MD. For metforminH$^+$, a snapshot was taken for every 10 ps for the last 10 ns of MD. Amino acids with high unfavourable contacts are characterized by high positive energy [115]. In contrast, residues with significant contacts exhibit negative values. For the plant extracts, amino acids Ile32, Lys55, and Met111 are hotspot residues for ligand binding (Fig. S15). These functional residues agree with the docking as well as MD data.

3.7. Pharmacophore analysis

The pharmacophore model was generated in the Phase module employing poses of the top three active compounds. A total of 69 poses generated in the MMGBSA postprocessing of QPLD were used for the calculation. A total of 25 actives were detected. A five-point model was created to match at least 25 % of the actives. The hypothesis feature range was set between four and seven, with a preference for five. The phase hypo formula was employed as a scoring function. Fig. 28A shows the model consisting of three hydrogen-bond acceptors (A1, A3 and A5), a hydrogen bond donor (D9), and two aromatic rings (R13 and R14). Fig. 28B depicts the most compatible model, including the template ligand.

4. Conclusion

Computational techniques such as docking, DFT, MD, pharmacophore modelling and ADMET studies have been used to gain insights into the role of *T. officinale* in JNK1. The results point to quercetin, myricetin and daphnetin as potential JNK1 inhibitors. QPLD docking revealed that quercetin bound tightly to JNK1 (-10.432 kcal/mol). Pharmacophore modelling also suggested quercetin as the most active compound. Quercetin also showed the lowest band gap (5.919 eV) among the rest of the ligands. In ADMET, quercetin did not violate any of Lipinski's rules of five, and in general, all the lead phytocompounds showed toxicity values within the acceptable ranges. By binding with pertinent residues such as the gatekeeper residue Met108, the *T. officinale* compounds can interfere with JNK1 activity, thereby dysregulating its bioactivities. Furthermore, compounds myricetin (ΔG_{BIND}

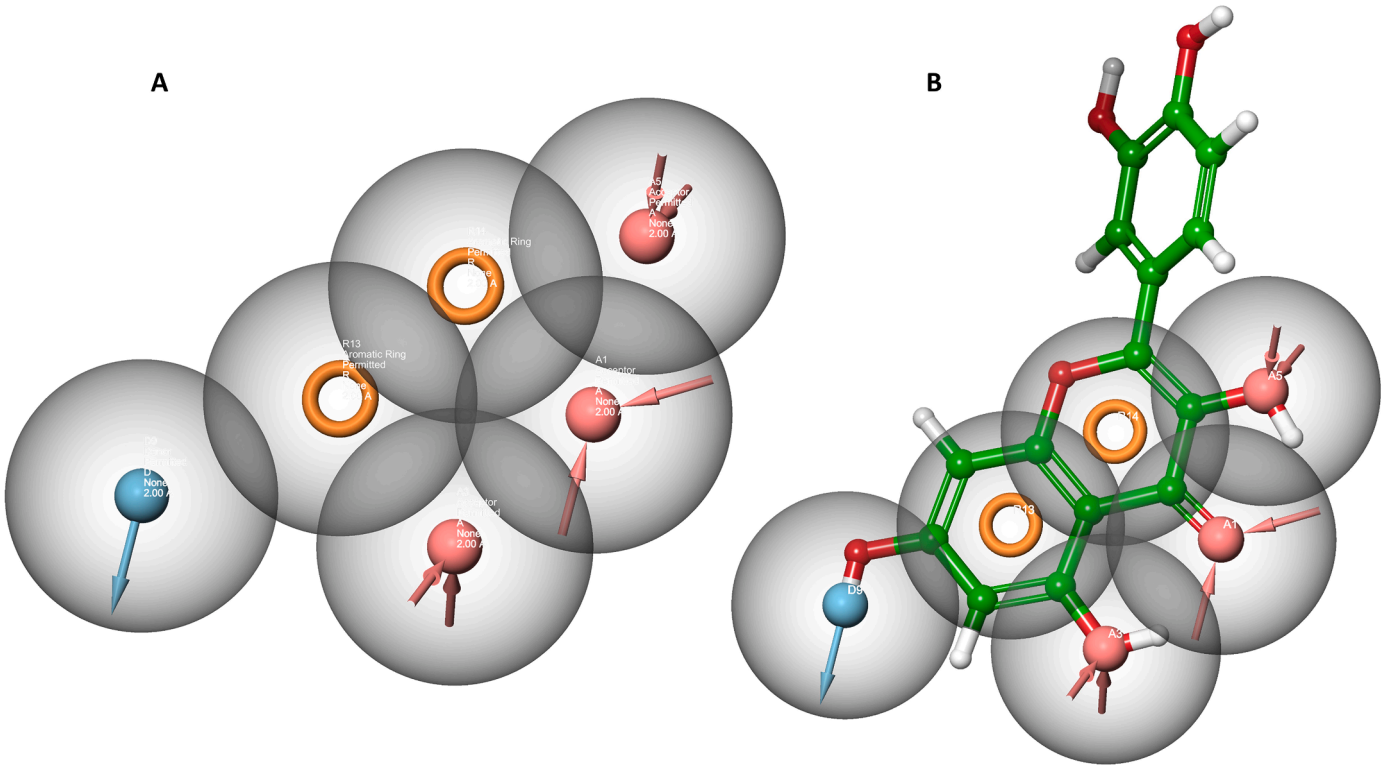


Fig. 28. (A)Representation of pharmacophore model AAADRR based on top three chemicals. (B) The most active compound (quercetin) within the pharmacophore model.

= -38.81), daphnetin (ΔG_{BIND} = -36.58), and quercetin (ΔG_{BIND} = -34.99 kcal/mol) formed stable complexes during MD simulation.

CRediT authorship contribution statement

Sphelele C. Sosibo: Writing – review & editing, Writing – original draft, Methodology, Investigation, Formal analysis, Data curation, Conceptualization. **Hendrik G. Kruger:** Writing – review & editing, Supervision, Methodology, Formal analysis. **Wonder P. Nxumalo:** Writing – review & editing, Visualization, Methodology, Formal analysis. **Zimbili Zondi:** Writing – review & editing, Visualization, Supervision, Resources, Formal analysis.

Declaration of competing interest

The authors declare that they have no known competing financial interests or personal relationships that could have appeared to influence the work reported in this paper.

Acknowledgements

The authors gratefully acknowledge the facilities the Department of Chemistry, North-West University, South Africa provided.

The Center for High-Performance Computing (CHPC) (https://www.chpc.ac.za/) is thanked for providing supercomputing resources and licenses for the various codes.

SCS would like to thank everyone who contributed to this work.

Supplementary materials

Supplementary material associated with this article can be found, in the online version, at doi:10.1016/j.chphi.2024.100757.

Data availability

Data will be made available on request.

References

[1] D. Iafusco, et al., From Metabolic Syndrome to Type 2 Diabetes in Youth, Children 10 (3) (2023) 516.
[2] C. Baumgartner, et al., Ectopic lipid metabolism in anterior pituitary dysfunction, Front. Endocrinol. (Lausanne) 14 (2023) 1075776.
[3] A. Artasensi, et al., Obesity and Type 2 Diabetes: Adiposopathy as a Triggering Factor and Therapeutic Options, Molecules. 28 (7) (2023) 3094.
[4] H. Sun, et al., IDF Diabetes Atlas: Global, regional and country-level diabetes prevalence estimates for 2021 and projections for 2045, Diabetes Res. Clin. Pract. 183 (2022) 109119.
[5] A.G. Tabák, et al., Prediabetes: a high-risk state for diabetes development, Lancet 379 (9833) (2012) 2279–2290.
[6] W.R. Lin, et al., Role of antidiabetic agents in type 2 diabetes patients with chronic kidney disease, World J. Diabetes. 14 (4) (2023) 352–363.
[7] A.J. Scheen, Clinical pharmacology of antidiabetic drugs: What can be expected of their use? La Presse Médicale 52 (1) (2023) 104158.
[8] J. Lan, et al., Meta-analysis of the effect and safety of berberine in the treatment of type 2 diabetes mellitus, hyperlipemia and hypertension, J. Ethnopharmacol. 161 (2015) 69–81.
[9] L. Tarasova, et al., Association of genetic variation in the organic cation transporters OCT1, OCT2 and multidrug and toxin extrusion 1 transporter protein genes with the gastrointestinal side effects and lower BMI in metformin-treated type 2 diabetes patients, Pharmacogenet. Genomics. 22 (9) (2012) 659–666.
[10] J.O. Unuofin, S.L. Lebelo, Antioxidant effects and mechanisms of medicinal plants and their bioactive compounds for the prevention and treatment of type 2 diabetes: an updated review, Oxid. Med. Cell Longev. 2020 (2020).
[11] M.W. Schwartz, et al., Brain Glucose Sensing and the Problem of Relative Hypoglycemia, Diabetes Care 46 (2) (2023) 237–244.
[12] A. Stasi, et al., Obesity-related chronic kidney disease: principal mechanisms and new approaches in nutritional management, Front. Nutr. 9 (2022) 925619.
[13] E.J. Barrett, et al., Diabetic microvascular disease: an endocrine society scientific statement, J. Clin. Endocrinol. Metab. 102 (12) (2017) 4343–4410.
[14] P.A. Kern, et al., Adipose tissue tumor necrosis factor and interleukin-6 expression in human obesity and insulin resistance, Am. J. Physiology-Endocrinol. Metabol. (2001).
[15] Y.-j. Xing, et al., LncRNA HEM2ATM improves obesity-associated adipose tissues meta-inflammation and insulin resistance by interacting with heterogeneous nuclear ribonucleoprotein U, Clin. Immunol. (2023) 109234.

[16] T.K. Lam, et al., Free fatty acid-induced hepatic insulin resistance: a potential role for protein kinase C-δ, Am. J. Physiol.-Endocrinol. Metab. 283 (4) (2002) E682–E691.
[17] J. Delarue, C. Magnan, Free fatty acids and insulin resistance, Curr. Opin. Clin. Nutr. Metabolic Care 10 (2) (2007) 142–148.
[18] X. Yan, et al., Up-regulation of Toll-like receptor 4/nuclear factor-κB signaling is associated with enhanced adipogenesis and insulin resistance in fetal skeletal muscle of obese sheep at late gestation, Endocrinology 151 (1) (2010) 380–387.
[19] E. Seki, D.A. Brenner, M. Karin, A liver full of JNK: signaling in regulation of cell function and disease pathogenesis, and clinical approaches, Gastroenterology 143 (2) (2012) 307–320.
[20] D. Szukiewicz, Molecular Mechanisms for the Vicious Cycle between Insulin Resistance and the Inflammatory Response in Obesity, Int. J. Mol. Sci. 24 (12) (2023) 9818.
[21] J.H.M. Yung, A. Giacca, Role of c-Jun N-terminal kinase (JNK) in obesity and type 2 diabetes, Cells 9 (3) (2020) 706.
[22] B. Dérijard, et al., JNK1: a protein kinase stimulated by UV light and Ha-Ras that binds and phosphorylates the c-Jun activation domain, Cell 76 (6) (1994) 1025–1037.
[23] J.M. Kyriakis, et al., The stress-activated protein kinase subfamily of c-Jun kinases, Nature 369 (6476) (1994) 156–160.
[24] S. Leppä, et al., Differential regulation of c-Jun by ERK and JNK during PC12 cell differentiation, EMBO J. 17 (15) (1998) 4404–4413.
[25] A. Minden, M. Karin, Regulation and function of the JNK subgroup of MAP kinases, Biochimica et Biophysica Acta (BBA)-Reviews on Cancer 1333 (2) (1997) F85–F104.
[26] K. Sabapathy, Role of the JNK pathway in human diseases, Prog. Mol. Biol. Transl. Sci. 106 (2012) 145–169.
[27] A. Kumar, et al., JNK pathway signaling: a novel and smarter therapeutic targets for various biological diseases, Future Med. Chem. 7 (15) (2015) 2065–2086.
[28] M.A. Bogoyevitch, The isoform-specific functions of the c-Jun N-terminal Kinases (JNKs): differences revealed by gene targeting, Bioessays 28 (9) (2006) 923–934.
[29] R. Nakano, T. Nakayama, H. Sugiya, Biological properties of JNK3 and its function in neurons, astrocytes, pancreatic β-cells and cardiovascular cells, Cells 9 (8) (2020) 1802.
[30] H. Tsuiki, et al., Constitutively active forms of c-Jun NH2-terminal kinase are expressed in primary glial tumors, Cancer Res. 63 (1) (2003) 250–255.
[31] M.A. Bogoyevitch, et al., Targeting the JNK MAPK cascade for inhibition: basic science and therapeutic potential, Biochimica et Biophysica Acta (BBA)-Proteins Proteomics 1697 (1-2) (2004) 89–101.
[32] A.M. Bode, Z. Dong, The functional contrariety of JNK, Mol. Carcinogenesis: Published in cooperation with University Texas MD Anderson Cancer Center 46 (8) (2007) 591–598.
[33] W. Lu, et al., Development of a Covalent Inhibitor of c-Jun N-Terminal Protein Kinase (JNK) 2/3 with Selectivity over JNK1, J. Med. Chem. 66 (5) (2023) 3356–3371.
[34] S. Pietkiewicz, et al., Oppositional Regulation of Noxa by JNK1 and JNK2 during Apoptosis Induced by Proteasomal Inhibitors, PLoS. One 8 (4) (2013) e61438.
[35] L. Du, et al., JNK2 is required for the tumorigenic properties of melanoma cells, ACS. Chem. Biol. 14 (7) (2019) 1426–1435.
[36] I. Nikolic, M. Leiva, G. Sabio, The role of stress kinases in metabolic disease, Nat. Rev. Endocrinol. 16 (12) (2020) 697–716.
[37] M. Khalid, et al., Insulin signal transduction perturbations in insulin resistance, Int. J. Mol. Sci. 22 (16) (2021) 8590.
[38] J. Hirosumi, et al., A central role for JNK in obesity and insulin resistance, Nature 420 (6913) (2002) 333–336.
[39] P.A. Carpino, D. Hepworth, Beyond PPARs and metformin: new insulin sensitizers for the treatment of type 2 diabetes, Annu Rep. Med. Chem. 47 (2012) 177–192.
[40] R. Naz, et al., Food Polyphenols and Type II Diabetes Mellitus: Pharmacology and Mechanisms, Molecules. 28 (10) (2023) 3996.
[41] S. Halazy, Designing heterocyclic selective kinase inhibitors: from concept to new drug candidates, ARKIVOC. 7 (2006) 496–508.
[42] M.A. Siddiqui, P.A. Reddy, Small molecule JNK (c-Jun N-terminal kinase) inhibitors, J. Med. Chem. 53 (8) (2010) 3005–3012.
[43] V.P. Krenitsky, et al., Discovery of CC-930, an orally active anti-fibrotic JNK inhibitor, Bioorg. Med. Chem. Lett. 22 (3) (2012) 1433–1438.
[44] P. Koch, M. Gehringer, S.A. Laufer, Inhibitors of c-Jun N-terminal kinases: an update, J. Med. Chem. 58 (1) (2015) 72–95.
[45] S.S. Pammi, B. Suresh, A. Giri, Antioxidant potential of medicinal plants, J. Crop. Sci. Biotechnol. 26 (1) (2023) 13–26.
[46] B. Lis, B. Olas, Pro-health activity of dandelion (Taraxacum officinale L.) and its food products–history and present, J. Funct. Foods. 59 (2019) 40–48.
[47] A.K. Watson, K.L. Bailey, *Taraxacum officinale FH Wigg, dandelion (Asteraceae)*, in *Biological control programmes in Canada 2001-2012*, CABI Wallingford UK, 2013, pp. 383–391.
[48] A. Di Napoli, P. Zucchetti, A comprehensive review of the benefits of Taraxacum officinale on human health, Bull. Natl. Res. Cent. 45 (1) (2021) 110.
[49] F.E. Wirngo, M.N. Lambert, P.B. Jeppesen, The physiological effects of dandelion (Taraxacum officinale) in type 2 diabetes, Review Diabetic Studies: RDS 13 (2-3) (2016) 113.
[50] H. Willems, S. De Cesco, F. Svensson, Computational Chemistry on a Budget: Supporting Drug Discovery with Limited Resources, J. Med. Chem. 63 (18) (2020) 10158–10169.
[51] B. Honarparvar, et al., Integrated Approach to Structure-Based Enzymatic Drug Design: Molecular Modeling, Spectroscopy, and Experimental Bioactivity, Chem. Rev. 114 (1) (2014) 493–537.
[52] V.T. Sabe, et al., Current trends in computer aided drug design and a highlight of drugs discovered via computational techniques: A review, Eur. J. Med. Chem. 224 (2021) 113705.
[53] R. Rolta, et al., In silico screening of hundred phytocompounds of ten medicinal plants as potential inhibitors of nucleocapsid phosphoprotein of COVID-19: An approach to prevent virus assembly, J. BioMol. Struct. Dyn. 39 (18) (2021) 7017–7034.
[54] D. Salaria, et al., In vitro and in silico antioxidant and anti-inflammatory potential of essential oil of Cymbopogon citratus (DC.) Stapf. of North-Western Himalaya, J. BioMol. Struct. Dyn. 40 (24) (2022) 14131–14145.
[55] S.K. Katari, et al., Inhibitor design against JNK1 through e-pharmacophore modeling docking and molecular dynamics simulations, J. Recept. Signal Transduction 36 (6) (2016) 558–571.
[56] Mitogen-activated protein kinase 8 (JNK1; MAPK8); mitogen-activated protein kinase 8 interacting protein 1 (JIP1; MAPK8IP1; IB1), Sci.-Bus. eXchange 1 (39) (2008) 948.
[57] J. Wang, et al., Identify of promising isoquinolone JNK1 inhibitors by combined application of 3D-QSAR, molecular docking and molecular dynamics simulation approaches, J. Mol. Struct. 1225 (2021) 129127.
[58] Frisch, A., *gaussian 09W Reference*. Wallingford, USA, 25p, 2009. 470.
[59] E.D. Glendening, C.R. Landis, F. Weinhold, Natural bond orbital theory: Discovering chemistry with NBO7, Complemen. Bonding Anal. (2021) 129–156.
[60] T. Lu, F. Chen, Multiwfn: A multifunctional wavefunction analyzer, J. Comput. Chem. 33 (5) (2012) 580–592.
[61] N.M. O'boyle, A.L. Tenderholt, K.M. Langner, Cclib: a library for package-independent computational chemistry algorithms, J. Comput. Chem. 29 (5) (2008) 839–845.
[62] J. Racine, gnuplot 4.0: a portable interactive plotting utility, Wiley Online Library, 2006.
[63] J. Sánchez-Márquez, et al., Introducing "UCA-FUKUI" software: reactivity-index calculations, J. Mol. Model. 20 (2014) 1–13.
[64] S. Kim, et al., PubChem in 2021: new data content and improved web interfaces, Nucleic. Acids. Res. 49 (D1) (2021) D1388–D1395.
[65] S. Jagannath, S.H. Mallanna, C. Nandini, Diet-inducing hypercholesterolemia show decreased O-GlcNAcylation of liver proteins through modulation of AMPK, J. Physiol. Biochem. 80 (1) (2024) 205–218.
[66] J. Biwi, et al., The Many Ways by Which O-GlcNAcylation May Orchestrate the Diversity of Complex Glycosylations, Molecules. 23 (11) (2018).
[67] C. Lu, et al., OPLS4: Improving force field accuracy on challenging regimes of chemical space, J. Chem. Theory. Comput. 17 (7) (2021) 4291–4300.
[68] J.C. Shelley, et al., Epik: a software program for pK a prediction and protonation state generation for drug-like molecules, J. Comput. Aided. Mol. Des. 21 (2007) 681–691.
[69] J.R. Greenwood, et al., Towards the comprehensive, rapid, and accurate prediction of the favorable tautomeric states of drug-like molecules in aqueous solution, J. Comput. Aided. Mol. Des. 24 (6-7) (2010) 591–604.
[70] M. Rostkowski, et al., Graphical analysis of pH-dependent properties of proteins predicted using PROPKA, BMC. Struct. Biol. 11 (1) (2011) 6.
[71] B. Li, et al., Hit-to-lead optimization and kinase selectivity of imidazo [1, 2-a] quinoxalin-4-amine derived JNK1 inhibitors, Bioorg. Med. Chem. Lett. 23 (18) (2013) 5217–5222.
[72] G. Madhavi Sastry, et al., Protein and ligand preparation: parameters, protocols, and influence on virtual screening enrichments, J. Comput. Aided. Mol. Des. 27 (2013) 221–234.
[73] R.A. Friesner, et al., Extra precision glide: Docking and scoring incorporating a model of hydrophobic enclosure for protein− ligand complexes, J. Med. Chem. 49 (21) (2006) 6177–6196.
[74] E. Harder, et al., OPLS3: a force field providing broad coverage of drug-like small molecules and proteins, J. Chem. Theory. Comput. 12 (1) (2016) 281–296.
[75] C.A. Lipinski, et al., Experimental and computational approaches to estimate solubility and permeability in drug discovery and development settings, Adv. Drug Deliv. Rev. 23 (1-3) (1997) 3–25.
[76] A.E. Cho, et al., Importance of accurate charges in molecular docking: quantum mechanical/molecular mechanical (QM/MM) approach, J. Comput. Chem. 26 (9) (2005) 915–931.
[77] S. Kalyaanamoorthy, Y.-P.P. Chen, Quantum polarized ligand docking investigation to understand the significance of protonation states in histone deacetylase inhibitors, J. Mol. Graph. Model. 44 (2013) 44–53.
[78] W. Pietruś, et al., Isomeric Activity Cliffs—A Case Study for Fluorine Substitution of Aminergic G Protein-Coupled Receptor Ligands, Molecules. 28 (2) (2023) 490.
[79] C. Ragi, K. Muraleedharan, Antioxidant activity of Hibiscetin and Hibiscitrin: insight from DFT, NCI, and QTAIM, Theor. Chem. Acc. 142 (3) (2023) 30.
[80] S.N. Mali, H.K. Chaudhari, Molecular modelling studies on adamantane-based Ebola virus GP-1 inhibitors using docking, pharmacophore and 3D-QSAR, SAR. QSAR. Environ. Res. 30 (3) (2019) 161–180.
[81] O.O. Elekofehinti, et al., Identification of lead compounds from large natural product library targeting 3C-like protease of SARS-CoV-2 using E-pharmacophore modelling, QSAR and molecular dynamics simulation, In. Silico Pharmacol. 9 (1) (2021) 49.
[82] K.J. Bowers, et al., Scalable algorithms for molecular dynamics simulations on commodity clusters, in: Proceedings of the 2006 ACM/IEEE Conference on Supercomputing, 2006.
[83] W. Jorgensen, J. Chandrasekhar, J. Madura, lmpey, RW; Klein,ML, J. Chem. Phys 79 (1983) 926.

[84] J.J. Blessy, D.J.S. Sharmila, Molecular simulation of N-acetylneuraminic acid analogs and molecular dynamics studies of cholera toxin-Neu5Gc complex, J. BioMol. Struct. Dyn. 33 (5) (2015) 1126–1139.
[85] D.J. Evans, B.L. Holian, The nose–hoover thermostat, J. Chem. Phys. 83 (8) (1985) 4069–4074.
[86] M.P. Jacobson, et al., A hierarchical approach to all-atom protein loop prediction, Proteins: Struct. Function Bioinf. 55 (2) (2004) 351–367.
[87] T. Hou, et al., Assessing the performance of the molecular mechanics/Poisson Boltzmann surface area and molecular mechanics/generalized Born surface area methods. II. The accuracy of ranking poses generated from docking, J. Comput. Chem. 32 (5) (2011) 866–877.
[88] S.L. Dixon, et al., PHASE: a new engine for pharmacophore perception, 3D QSAR model development, and 3D database screening: 1. Methodology and preliminary results, J. Comput. Aided. Mol. Des. 20 (2006) 647–671.
[89] D. Ramírez, J. Caballero, Is it reliable to take the molecular docking top scoring position as the best solution without considering available structural data? Molecules. 23 (5) (2018) 1038.
[90] G. Liu, et al., Aminopyridine carboxamides as c-Jun N-terminal kinase inhibitors: targeting the gatekeeper residue and beyond, Bioorg. Med. Chem. Lett. 16 (22) (2006) 5723–5730.
[91] C.K. Lombard, et al., Allosteric modulation of JNK docking site interactions with ATP-competitive inhibitors, BioChem. 57 (40) (2018) 5897–5909.
[92] J.Y. Chung, J.-M. Hah, A.E. Cho, Correlation between Performance of QM/MM Docking and Simple Classification of Binding Sites, J. Chem. Inf. Model. 49 (10) (2009) 2382–2387.
[93] L.R. Domingo, P. Pérez, The nucleophilicity N index in organic chemistry, Org. Biomol. Chem. 9 (20) (2011) 7168–7175.
[94] A.E. Owen, et al., Exploration of semi-carbazone derivatives as promising agents against cholera: Insights from spectroscopic analysis, reactivity studies (ELF, HOMO-LUMO, NBO), solvation effects, and molecular docking investigations, Chem. Phys. Impact 8 (2024) 100438.
[95] P. Muller, Glossary of terms used in physical organic chemistry (IUPAC Recommendations 1994), Pure Appl. Chem. 66 (5) (1994) 1077–1184.
[96] P. Politzer, J.S. Murray, Electronegativity—a perspective, J. Mol. Model. 24 (2018) 1–8.
[97] P. Pérez, R. Contreras, A. Aizman, Relationship between solvation energy, chemical potential and hardness variations, J. Mol. Struct.: THEOCHEM 390 (1-3) (1997) 169–175.
[98] R.P. Iczkowski, J.L. Margrave, Electronegativity, J. Am. Chem. Soc. 83 (17) (1961) 3547–3551.
[99] K.K. Hazarika, N.C. Baruah, R.C. Deka, Molecular structure and reactivity of antituberculosis drug molecules isoniazid, pyrazinamide, and 2-methylheptylisonicotinate: a density functional approach, Struct. Chem. 20 (2009) 1079–1085.
[100] R.G. Pearson, Ionization potentials and electron affinities in aqueous solution, J. Am. Chem. Soc. 108 (20) (1986) 6109–6114.
[101] O. Manual, Jaguar 6.6. (2006).
[102] F. Kajzar, J. Messier, Third order nonlinear optical effects in conjugated polymers. Conjugated Polymers: The Novel Science and Technology Highly Conducting and Nonlinear Optically Active Materials, 1991, pp. 509–554.
[103] I.M. Kenawi, A.H. Kamel, R.H. Hilal, BSSE effects on the static dipole polarizability and first dipole hyperpolarizability of diclofenac sodium, J. Mol. Struct. 851 (1) (2008) 46–53.
[104] R. Pottel, D. Adolph, U. Kaatze, Dielectric relaxation in aqueous solutions of some dipolar organic molecules, Berichte der Bunsengesellschaft für physikalische Chemie 79 (3) (1975) 278–285.
[105] C.T. Tedjeuguim, S.N. Tasheh, G.Julius Numbonui, Theoretical Investigation of the Nonlinear Optical and Charge Transport Properties of N-(4-Methoxybenzylidene) Isonicotinohydrazone and Some of Its Derivatives: A DFT and TD-DFT Study, Adv. Mater. Sci. Eng. 2023 (2023) 6588603.
[106] A. Otero-De-La-Roza, E.R. Johnson, J. Contreras-García, Revealing non-covalent interactions in solids: NCI plots revisited, Phys. Chem. Chem. Phys. 14 (35) (2012) 12165–12172.
[107] P.A. Onguéné, et al., The potential of anti-malarial compounds derived from African medicinal plants, part III: an in silico evaluation of drug metabolism and pharmacokinetics profiling, Org. Med. Chem. Lett. 4 (1) (2014) 6.
[108] L. Gong, et al., Metformin pathways: pharmacokinetics and pharmacodynamics, Pharmacogenet. Genomics. 22 (11) (2012) 820–827.
[109] Z. Sun, et al., Utility of B-Factors in Protein Science: Interpreting Rigidity, Flexibility, and Internal Motion and Engineering Thermostability, Chem. Rev. 119 (3) (2019) 1626–1665.
[110] A. Bornot, C. Etchebest, A.G. de Brevern, Predicting protein flexibility through the prediction of local structures, Proteins. 79 (3) (2011) 839–852.
[111] J. Kuriyan, et al., Effect of anisotropy and anharmonicity on protein crystallographic refinement: An evaluation by molecular dynamics, J. Mol. Biol. 190 (2) (1986) 227–254.
[112] A. Kuzmanic, N.S. Pannu, B. Zagrovic, X-ray refinement significantly underestimates the level of microscopic heterogeneity in biomolecular crystals, Nat. Commun. 5 (1) (2014) 3220.
[113] J. Chen, et al., Effect of mutations on binding of ligands to guanine riboswitch probed by free energy perturbation and molecular dynamics simulations, Nucleic. Acids. Res. 47 (13) (2019) 6618–6631.
[114] J. Chen, et al., Decoding the Identification Mechanism of an SAM-III Riboswitch on Ligands through Multiple Independent Gaussian-Accelerated Molecular Dynamics Simulations, J. Chem. Inf. Model. 62 (23) (2022) 6118–6132.
[115] J. Jose, et al., Probing the inhibition of MAO-B by chalcones: an integrated approach combining molecular docking, ADME analysis, MD simulation, and MM-PBSA calculations, J. Mol. Model. 30 (4) (2024) 103.